MODELING EPITHELIAL OVARIAN CANCER IN THE MOUSE

A Dissertation

Presented to the Faculty of the Graduate School

of Cornell University

In Partial Fulfillment of the Requirements for the Degree of

Doctor of Philosophy

by

Andrea Flesken-Nikitin

August 2011

MODELING EPITHELIAL OVARIAN CANCER IN THE MOUSE

Andrea Flesken-Nikitin, Ph. D.

Cornell University 2011

For over five decades epithelial ovarian cancer (EOC) is identified as the leading cause of death from gynecological malignancies in the USA. Unfortunately, due to latent progression of EOC and lack of accurate animal models studies of this disease's pathogenesis have been challenging. Not surprisingly, establishment of adequate screening tests for early disease stages, at which point the cancer would be curable, and advances in treatment approaches have been slow.

Deficiency of tumor suppressor genes *p53* and *RB* and overexpression of *c-MYC* oncogene occur frequently in the most common form of sporadic EOC, high grade serous adenocarcinoma. Thus, we have initiated development of several mouse models of EOC based on alterations of these genes in the presumed EOC tissue of origin, the ovarian surface epithelium (OSE). By using a new approach of *in situ* targeting of OSE we have demonstrated that disruption of *p53* and *Rb* leads to high grade serous adenocarcinoma. We have also established new models of EOC intraperitoneal spreading and have shown that *c-MYC* promotes tumorigenicity of *p53*-and *p53/Rb*-deficient OSE.

Next, we have shown that multiphoton microscopy and second harmonic generation (MPM/SHG) imaging are well suited for studies of cell motility *in vivo* and can complement pathological characterization EOC by

allowing optical biopsies of native human and mouse tissues at resolution comparable to that of routinely processed histological sections. We have also shown the feasibility of laparoscopic MPM/SHG. Moreover, we identified layered nanohybrids as suitable particles for combination of intravital biomedical imaging with controlled drug release.

As the first step to determine whether EOC arises from the stem cell compartment we have identified an OSE subpopulation which is positive for stem cell marker aldehyde dehydrogenase 1, efficiently forms clonogenic spheres and displays extended self-renewal properties in serial sphere generation assays. These putative OSE stem cells are slow cycling according to BrdU label retention assays and are mainly located in the hilum area of the mouse ovary. These findings will direct our future search for better approaches to target EOC cells with stem cell properties.

BIOGRAPHICAL SKETCH

Andrea Flesken-Nikitin was born on November 02, 1956, in Duisburg, Germany. Dedicated to a career in Chemistry and Biology, Andrea obtained her Bachelor's degree in Biochemistry from the Private Technical College Duisburg, as a State-Examined Technician. Working exclusively in the field of Cancer Research for many years, in Essen, Germany, San Antonio, Texas and Ithaca, New York, USA, and enjoying the challenge of novel research, Andrea decided on attaining an advanced degree. In the fall of 2005, Andrea started to pursue her Ph. D. degree at Cornell University, Ithaca, NY, where Dr. Andrew Yen agreed to supervise her study on modeling epithelial ovarian cancer in the mouse.

Diese Arbeit ist gewidmet an meine Großmutter, meinen Vater, meinen Ehemann und meinen Sohn.

ACKNOWLEDGMENTS

I gratefully acknowledge Dr. Andrew Yen, my committee chair, for his advice, encouragement and invaluable support during the time course of my Ph.D. project.

I also thank my Ph.D. committee members, Drs. Bendicht Pauli, Warren Zipfel and Stephen Bloom, for their suggestions, comments and constructive criticisms throughout my studies.

I would like to thank the Cornell Employee Degree Program which gave me the opportunity to complete my Ph.D. degree while working as a Support Specialist III in the Department of Biomedical Sciences.

Thank you to Dr. Alexander Nikitin for sharing his expertise and guidance in generating the mouse models, and performing pathological analyses. I thank my collaborators Drs. Rebecca Williams and Warren Zipfel, for their kind assistance with the multiphoton microscopy imaging; Dr. Lora Hedrick Ellenson for providing human ovarian biopsy samples; Jishnu Naskar and Dr. Emmanuel Giannelis for generating the nanoparticles., I would like to acknowledge my former and present colleagues David Corney, Chieh-Yang Cheng, Jinhyang Choi, Le Cheng, Chang-il Hwang, Samantha Palmaccio, Benjamin Ranard, Meredith Stone, Eric Yu, and Zongxiang Zhou. I appreciate their scientific support and kind help, when needed, which made working with them a pleasure. In addition, I would like to thank Lavanya Sayam, Cornell Biomedical Sciences Flow Cytometry Core Lab, for excellent technical assistance with flow cytometry. Thank you to Gabriel Balmus for taking the EGFP and DsRed sphere images.

Finally, I am thankful, to my husband for his patience, support and

understanding my wish to pursue an advanced degree. I thank you, my son Alexander, for his encouragement, dedication and practical advice during the scientific course work included in my studies.

TABLE OF CONTENTS

LIST OF FIGURES

LIST OF TABLES

LIST OF ABBREVIATIONS

AdCre	Adenovirus Cre recombinase
ALDH1	Aldehyde dehydrogenase 1
APL	Acute promeyelomytic leukemia
BLI	Bioluminescence imaging
BM	Basement membrane
Brca1	Breast cancer 1
Brca2	Breast cancer 2BrdU 5-Bromo-2'-deoxyuridine
CA 125	Cancer antigene 125
CDK	Cyclin dependent kinase
CL	Corpus luteum
CMV	Cytomegalovirus
Cre	Cre-recombinase
creERT_2	Cre fused to a $G_{400}V/M_{543}A$/L544A triple mutation of the human estrogen receptor ligand binding domain
DAPI	4',6-Diamidino-2-phenylinodole
DMBA	7,12-Dimethylbenz(a)anthracene
DNA	Deoxyribonucleic acid
EGF	Epidermal growth factor
EMT	Epithelial-mesenchymal transition
EOC	Epithelial ovarian cancer
F	Follicle
FACS	Fluorescence activated cell sorter
FAD	Flavin adenine dinucleotide

fs	Femtosecond
Gd/Mg	Gadolinium/Magnesium
GEM	Genetically engineered mouse
HDM2	Human double minute 2
H&E	Hematoxylin&Eosin
IHC	Immunohistochemistry
i.p.	Intraperitoneal
iPS	Induced pluripotent stem
IR	Infrared
IRES	Internal ribosome entry site
i.v.	Intravenous
KI	Knock in
KO	Knock out
LNH	Layered nanohybrid
LNH-Ly	LNH-Lucifer yellow
LPD	Lipid-polycation-DNA
LRC	Label retaining cell
LW	Long wavelength
MCP1	Monocyte chemotactic protein
mdm2	Murine double minute 2
MEM device	Microelectromechanical device
Mg/Al	Magnesium/Aluminum
MISIIR	Mullerian inhibitory substance type II receptor
MRI	Magnetic resonance imaging
mRNA	Messenger ribonucleic acid
miRNA	MicroRNA

MOI	Multiplicity of infection
MPM	Multiphoton microscopy
NA	Not applicable
NADH	Nicotinamide adenine dinucleotide
NAD(P)H	Nicotinamide adenine dinucleotide phosphate
nJ	Nano joule
NIR	Near infrared
OB	Ovarian bursa
OSE	Ovarian surface epithelium
OSE-CFC	OSE-Clone forming cell
OSE-CFU	OSE-Clone forming unit
OSE-SC	OSE-stem cell
OSE-SCM	OSE-stem cell medium
PBS	Phosphate buffered saline
PCR	Polymerase chain reaction
pfu	Particle forming units
RB1	Retinoblastoma gene1
RCAS	Replication-competent avian retrovirus
RNA	Ribonucleic acid
RU	Rudimentary unit
SA	Splice acceptor
Sca1	Stem cell antigen 1
SC	Stem cell
s.c.	Subcutaneous
SHG	Second harmonic generation
SSC	Somatic stem cell

SV40 Tag	Simian virus 40 T antigen
SW	Short wavelength
TA	Transit amplifying
TAg	SV40 T antigen
TM	Tamoxifen
TP53	Tumor protein 53
TVA	Tumor virus A
UTR	Untranslated region
UV	Ultraviolet
V	Vessel

CHAPTER 1

INTRODUCTION

1.1 Ovarian Cancer Biology and Etiology

Ovarian Cancer is the leading cause of death from gynecological malignancies in the USA with 13,850 deaths predicted in 2010 (Jemal et al., 2010). One out of seventy women will endure the disease in the year 2010. The high lethality rate is mainly related to late diagnosis. Ovarian cancer has been termed a 'silent killer', because only 20% of ovarian cancers are detected while they are at stage I, limited to the ovaries, a stage when available therapies can successfully cure 90% of patients (Bast et al., 2009). At an early stage of the disease patients show none or few symptoms. However, currently only limited early detection methods exist. Early diagnostic tools are trans-vaginal ultrasound and serum CA125 (cancer antigen 125) blood screenings in combination. Unfortunately, ongoing trials showed their shortcomings (Menon et al., 2009). For example, one trial reported detection of three ovarian cancers at advanced stages and none at early stages among 470 screenings. The malignancy progresses by spreading and metastasing to the pelvic organs (stage II), the abdomen (stage III) or beyond the peritoneal cavity (stage IV). At advanced stages cytoreductive surgery is carried out to remove the bulk of the tumor. After surgery 70% of ovarian cancers will respond to a combination regimen of platinum- and taxane-based chemotherapy and in approximately 50% of these patients, residual cancer is undetectable utilizing imaging studies and serum markers after 5 months of treatment. However,

limited numbers of drug-resistant cells remain dormant in the peritoneal cavity and, after several months, start to grow progressively, acquire resistance to drugs and cause the death of patients. Unlike neoplasms at many other sites, no anatomical barrier prevents widespread dissemination of ovarian cancer throughout the peritoneal cavity. Thus, due to the distinctive clinical biology and behavior of ovarian cancer, early detection is crucial to life-saving and our ability to cure this malignancy.

Ovarian cancer as a general term, groups together a diverse set of cancers originating from the ovary. Around 90% of all ovarian malignancies are epithelial cancers (EOCs)(Corney et al.; 2008; Nikitin et al., 2005), classified as serous, mucinous, endometrioid, clear cell, transitional cell, squamous cell, and mixed epithelial neoplasms (Scully et al., 1999). The most common variant of EOC is serous adenocarcinoma which occurs in 80% of all cases. It is believed that EOC arises from the ovarian surface epithelium (OSE) lining the ovary or the epithelial inclusion cysts (Auersperg et al., 2008). Malignant neoplasms which have a similar histology might also arise from the lining of the fallopian tube, deposits of endometriosis or the exterior of the peritoneal cavity (Lengyel et al., 2010).

Understanding of EOC etiology remains inadequate and although several risk factors have been identified, their direct involvement remains mainly undetermined. The hypothesis that persistent ovulation increases ovarian carcinogenesis occurrence has received the largest attention. In normal ovarian homeostasis, repeated rupture of the ovarian surface occurs during oogenesis and the subsequent repair by OSE proliferation may result in cancer inducing mutations. Numerous studies support this theory in demonstrating that a reduction in ovulatory events by pregnancy and/or oral

contraceptive decreases EOC risk (Corney et al., 2008). However, since the cellular and molecular levels of EOC are remarkably heterogeneous, other effects, such as reproductive hormones or acute inflammation, both of which may be mutagenic, also have to be considered as cancer initiating events (Fleming et al., 2006; Nikitin et al., 2005).

1.2 Genetics of Epithelial Ovarian Cancer

1.2.1 Tumor Suppressor Genes p53 and RB in EOC. Advanced EOCs show a wide range of genetic and epigenetic. abnormalities. Familial cancer represents only about 5% of all cases and frequently contains mutations in tumor suppressor genes *Brca1* and *2*. By far the most frequent alterations in sporadic EOC occur in the *p53* (a.k.a, *TP53 and Trp53)* and *Rb* (a.k.a., Retinoblastoma 1) pathways. Importantly, alterations in their function have been associated with poor prognosis for ovarian cancer patients (Horiuchi et al., 2003; Katsaros et al., 2004; Tachibana et al., 2003). Deficiencies in p53 and RB pathways are present in over eighty percent of human cancers (Hahn and Weinberg, 2002; Sherr and McCormick, 2002).

Mutations and loss of the *p53* gene are the most common genetic alteration in sporadic human EOC and are observed in 60-80% of both sporadic and familial cases. Functioning as a transcription factor, p53 directly connects to p53-binding sites in regulatory regions of target genes. Utilizing bioinformatics more than 4,000 putative target genes were identified (Wang et al., 2001). Activation of p53 occurs through UV irradiation-induced DNA damage, inappropriate proto-oncogene activation, mitogenic signaling and hypoxia. Cell type specific responses are cell cycle arrest, senescence,

differentiation or induction of the apoptotic cascade. Thus, impairment of wildtype p53 function, gain of oncogenic function or the ability to induce p53 inappropriately results in increased cellular proliferation and survival. Alterations in both p53 regulators and downstream targets have been also implicated in ovarian cancer. The p53 inhibitor, HDM2 (mdm2) is an E3 ubiquitin ligase that binds p53 and targets it for proteasomal degradation. Approximately one-third of ovarian cancers overexpress HDM2. In leukemia's with wild-type p53, distortion of the p53 - HDM2 binding with small molecular mass compounds such as nutlins increased p53 stability and induced apoptosis (Kojima et al., 2005). Thus, a similar therapy might be successful in EOCs with high levels of HDM2 and low levels of wild-type p53. Recently, a new class of p53 transcriptional targets, microRNA miR-34 family, has been discovered (Chang et al., 2007; Corney et al., 2010; Hermeking et al., 2010). All members of this family (miR-34a, miR-34b and miR3-4c) are down regulated in EOC and expression of miR34b/c is inversely correlated with disease stage (Corney et al., 2010). Strikingly, although *p53* mutations have been found in all histological types of EOC, *p53* mutations are strongly associated with high grade serous adenocarcinomas. On the contrary, they are rare in low grade or borderline serous carcinomas (Corney et al., 2008).

Frequent mutations in the RB pathway and *RB* loss or aberrant expression were demonstrated in over 60% of human ovarian carcinomas (Corney et al., 2008; Hashiguchi et al., 2001; Havrilesky et al., 2001; Nikitin et al., 2005).The *RB* family consists of *RB*, *p107* and *p130* tumor suppressor genes. They play an important part in the G1-S phase restriction point of the cell cycle by binding to the E2F family of transcription factors and governing DNA replication. RB is functionally inactivated by phosphorylation performed

by Cyclin/CDK complexes. These complexes are in turn regulated by CDK inhibitors INK4 (*p16 ^{Ink4a}*) and ARF (*p19*). Apart from important functions in cell cycle regulation the RB family genes play an important part in differentiation. Alterations in INK4 protein *p16^{Ink4a}*, *RB* or *cyclin D1/CDK4* are detected in nearly 50% of EOC clinical samples (Hashiguchi et al., 2001; Kusume et al., 1999).

Remarkably, over fifty percent of EOC patients have mutations in both the p53 and RB pathways, including forty percent of serous carcinomas (Hashiguchi et al., 2001). These pathways have widespread connections (Sherr and McCormick, 2002) which includes a link to the oncogene *C-MYC* by cross talk with E2Fs. HDM2 binds directly to p53 to inhibit transcription and catalyses p53 ubiquitination. In turn, p14 ARF binds to HDM2 to antagonize these functions. The ability of deregulated E2F to induce ARF transcription provides an additional connection between the RB pathway and p53.

The main challenge of studies based on clinical data, neoplastic specimens and cell lines is the difficulty of separating critically important genetic alterations from passenger charges. As discussed in the Section 1.4 and Chapter 2, introduction of specific genetic alterations in genetically modified mice should address this problem and allow direct genetic testing of the roles of p53 and RB in the pathogenesis of human EOC.

1.2.2 C-MYC Oncogene Association with EOC. *C-MYC* oncogene overexpression was detected in 41-66% of EOCs, while amplifications ranged at 20% of cases (Plisiecka-Halasa et al., 2003). Correlation studies between *C-MYC* gene copy number and clinico-pathological parameters of ovarian tumors revealed the highest frequency of amplification in mixed epithelial

40.9% and endometrioid 30.8%, followed by mucinous 26.9%, serous and non-classified 22.2% carcinomas. The amplification rate was strongly associated with the degree of malignancy of ovarian neoplasms, increasing statistically from low malignancy to high and was zero in benign adenoma. C-MYC is an oncogenic transcription factor, which uses distinct mechanisms for activating and repressing gene expression. The proto-oncogene was originally identified as the cellular homologue to *V-MYC*, the viral oncogene of the avian myelocytomatosis retrovirus (Vennstrom et al., 1982) in Burkitt's lymphoma patients. Three closely related MYC family proteins C-MYC, N-MYC and L-MYC exist, each with documented oncogenic potential and similar DNA binding properties. However, most data reports deregulated expression of C-MYC in a broad range of human cancers. Expression of C-MYC is often associated with poor prognosis, indicating a key role for this oncogene in carcinogenesis. For transcriptional activation, MYC and its binding partner MAX dimerize and bind to genomic DNA directly upstream or within the first introns of target genes. For transcriptional repression MYC does not interact with DNA directly, but rather is recruited through protein-protein interactions to target promoters and antagonizes the function of positive regulators of transcription (e.g. Sp1, Smad2, NF-Y).

One main biological function of *C-MYC* is the ability (Amati et al., 2001) to promote cell-cycle progression. C-MYC expression is virtually undetectable in quiescent tissue culture cells, however after serum stimulation, C-MYC mRNA and protein are rapidly induced and cells enter the G1 phase of the cell cycle. Subsequently, the mRNA and protein decline to low, but measurable, steady-state ranges in proliferating cells. If serum or growth factors are removed, C-MYC levels turn down to undetectable numbers and cells arrest.

Targeted gene deletion of both *c-Myc* alleles in embryonic stem cells leads to embryonic lethality at day 9.5-10.5, confirming the crucial role of C-MYC in normal growth control during mammalian development (Davis et al., 1993). Moreover, C-MYC significantly increases efficacy of somatic cell reprogramming into induced pluripotent stem (iPS) cells by transcription factors Oct4, Sox2, and Klf4. (Takahashi and Yamanaka, 2006) demonstrating the importance of this gene in mammalian biology.

Enigmatically, C-MYC, a potent inducer of cell proliferation, also possesses pro-apoptotic activity (Adhikary and Eilers, 2005). Ectopic expression of C-MYC in fibroblasts that were grown without extracellular and intracellular components that block apoptosis (survival factors), resulted in apoptosis, with the death of the entire cell population (Evan et al., 1992). Later experiments, with other promoters of cell proliferation (e.g. E2F) corroborated these studies (Wu and Levine, 1994). Thus, cells acquiring growth deregulating mutations may harbor 'built-in' tumor suppressive functions, which counteract the expansion of potentially malignant cells.

As discussed in Sections 1.4 and 1.5 and Chapter 4 and 7 the generation of syngeneic lines of OSE should facilitate investigation of effects by defined genetic alterations on EOC progression.

1.3 Adult Stem Cells of the OSE and Implications to EOC

Somatic (aka, adult, tissue specific) stem cells (SSC) are believed to regulate normal tissue morphogenesis, renewal and repair of injured tissues. In adult mammals, SSCs have been identified in many organs, including the hematopoietic system, brain, intestine, mammary gland, prostate and skin

(Weissman et al., 2001). Features of SSC include ability for long-term self-renewal and multipotency. Usually such cells are quiescent slow cycling, but when activated have increased potential for proliferation. SSC can divide either symmetrically, into two stem cells or two proliferating transit amplifying (TA) progeny, or asymmetrically, into one TA and one stem cell progeny. Anatomically, SSC and their progeny reside in a defined microenvironment, the SSC niche, protected from differentiation, apoptosis and diverse other processes that would deplete stem cell reserve (Fuchs et al., 2004; Moore and Lemischka, 2006).

The ovary is a reproductive organ and undergoes extensive tissue regeneration during folliculogenesis. Three primary functional somatic cell types of the ovary, the ovarian surface epithelium (OSE), theca cells and granulosa cells, could harbor a stem/progenitor cell population residing in a sheltering stem cell niche (Chang et al., 2009). Epithelia are continuous layers of tightly connected cells that constitute the surfaces e.g. corneal epithelium or epidermis and linings such as respiratory, uro-genital and ovarian surface epithelium of the ovary. They provide a protective envelope against the external environment and in addition regulate water and nutrient absorption as well as glandular secretions. While, epithelia can be multilayered (stratified; skin, prostate, breast) or single-layered (simple, OSE) and may originate from ectoderm, mesoderm (origin of the OSE), or endoderm, different epithelial mammalian tissues share several molecular and cellular characteristics (Blanpain et al., 2007). Epithelial development begins as a sheet of cells that attach to a basement membrane, loaded with extracellular matrix (ECM), nutritional, and growth factors that are formed and deposited at the interface of the epithelium and the underlying mesenchyme. Specifically, the OSE has

been shown to transition back and forth between epithelial and mesenchymal phenotypes (Ahmed et al., 2007; Auersperg et al., 1999), this epithelial-mesenchymal transition (EMT) is believed to be an intrinsic process of post-ovulatory wound repair after oocyte release and OSE rupture. Thus, normal OSE surrounding the ovary constantly mobilizes cell replacement of damaged and dead tissue at the ovulation place this process is defined as homeostasis. Classically, epithelial tissue homeostasis is driven by somatic stem cells. Therefore, OSE biology implies the existence of a stem cell source. Recently, putative thecal stem cells (Honda et al., 2007) and OSE stem/progenitor cells have been reported (Szotek et al., 2008) in the mouse. Unfortunately, no unique markers for OSE-SC have been identified and the location of these putative stem cells, as well as their ability for self-renewal, remains to be determent. As 90% of ovarian cancers are of epithelial origin (Auersperg et al., 2001; Cho and Shih Ie, 2009) and are believed to arise from the OSE, studies aiming to confirm the existence of OSE-SC and to provide their complete characterization are essential for determining whether distortion of OSE-SC dynamics leads to carcinogenesis. This issue is specifically addressed in Chapter 6.

1.4 Mouse Models in Cancer Research and Relevance to Human Cancer

1.4.1 Generating Accurate Mouse Models for Human Cancer. Animal models are extremely useful tools in directly testing the roles of environmental factors such as hormones, diet, UV radiation, and chemicals, in cancer development. Studies on the effects of oophorectomy and estrogen removal, which are impossible or unethical to do in women, led to the discovery that

tamoxifen inhibits mammary carcinogenesis and facilitated the drugs approval for the treatment of human breast cancer (Jordan et al., 1977). The causative roles of UV and sunburn in melanoma were recognized first in mouse studies (Noonan et al., 2001), and the effect of the promoting compound phenobarbital was characterized in mice developing liver cancer treated with the reagent.

Mice share 99% of their genes with humans. They show great similarities in development, physiology and biochemistry to humans, which make them a prime model for research into human disease. Better than any other model system, the mouse has revolutionized our capability to investigate gene function *in vivo* and understand the molecular mechanisms of malignant transformation.

Cancers are thought to arise from the accrual of mutations that transform cells, induce abnormal growth, proliferation, and metastasis. Discovery of these abnormalities and understanding how they contribute to the pathophysiology of neoplasms are necessary for improvements in diagnosis and therapy. Genetically modified mice have significantly contributed to our understanding of cancer formation. Furthermore, studies in mouse models tremendously contribute to the success in therapeutic treatments. In one recent human / mouse model trial, two mechanism-based therapies for treating human pancreatic neuroendocrine tumors led to the discovery of two drugs (sunitinib and everolimus) for fighting these cancers, the first new effective treatment after 25 years (Tuveson and Hanahan, 2011). Contemporary cancer research utilizes highly advanced genetically modified mouse models, tailored to address specific questions (Cheon and Orsulic, 2011). Numerous techniques for genetic manipulation are available to

researchers. Selecting the right techniques is an imperative first step in developing mouse models of cancers. The most common ways to create appropriate models are to activate oncogenes or inactivate tumor-suppressor genes (or both) through the use of transgenic and gene targeting approaches, such as gene knock out (KO) or knock (KI) in mice (Frese and Tuveson, 2007). For loss-of-function studies researcher normally utilize conventional or conditional KO alleles, whereas gain-of-function studies employ transgenic, conditional transgenic, and KI approaches. Conditional and inducible systems permit introduction of somatic alterations in a tissue-specific and time-controlled mode. Such systems allow avoiding embryonic lethality and other unwelcome phenotypes due to genetic alterations in a wide range of tissues. By far the most common conditional gene-expression strategy used is the Cre-*loxP* system. Cre recombinase recognizes specific 34-base pair *loxP* sites in the DNA and mediates recombination between them. The relative orientation of the two *loxP* sequences decide the recombination results, whether host DNA is excised, inverted or translocated (Hoess et al., 1986). Two same oriented *loxP* sites are inserted into the target gene locus with the KI strategy, to develop either KO mice or conditional transgenic mice. By crossing these mice to tissue specific *Cre* expressing mouse lines, the *Cre* recombinase will be only activated in the organ of interest. A different possibility is the administration of lentivirus or adenovirus expressing Cre. The benefit of the Cre-l*oxP* conditional set up is that gene function can be followed in a specific tissue or cell type at a specified time point, thus allowing accurate modeling of sporadic occurring mutational events in a sub-cellular level. Reporter mouse strains, such as *ROSA26-lacZ* reporter (*R26R*) strain (Soriano et al., 1999),

are used to confirm *Cre* expression is confined to the tissue and developmental stage of interest.

These approaches provide with a variety of tools facilitating modeling of ovarian cancer as described in Section 1.4.2 and Chapter 2.

1.4.2 Animal Models of Ovarian Cancer. Historically, use of rodent models to identify the carcinogenic potential of chemicals and other agents for induction of ovarian cancer reaches back more than 40 years. For example, as early as 1969; ovarian tumors were induced by direct application of 7,12-Dimethylbenz(a)anthracene DMBA (Krarup et al., 1969).

One of the first ovarian genetically engineered mouse model (GEM) made used an avian retroviral delivery system (Orsulic et al., 2002). TVA (tumor virus A) transgenic mice were generated with the TVA receptor expressed under the control of keratin 5 promoter and crossed with *p53* null mice to generate TVA/p53$^{-/-}$ animals. TVA expression resulted in susceptibility to infection of replication-competent avian retrovirus (RCAS) which carried different oncogenes of interest (*C-MYC*, *K-RAS*, *AKT*). However, the keratin 5 is widely expressed in the basal layer of stratified and simple epithelia in many organs (Marks et al., 2007). Hence, for targeting the OSE and ovary, dissected organs were infected in tissue culture experiments and then introduced into recipient mice either by injection or transplantation under the ovarian bursa. Keratin 5-TVA/p53$^{-/-}$ ovarian cells overexpressing any two oncogenes C-MYC, K-RAS or AKT induced carcinogenesis confirming the importance of genetic alterations in EOC development.

In a different mouse model system, expression of the transforming region of the SV40 large T antigen (SV40 Tag) was directed to the OSE by

using the Mullerian inhibitory substance type II recepter (MISIIR) promoter (Connolly et al., 2003). SV40 Tag binds and inactivates both p53 and RB proteins. The MISIIR-SV40-Tag transgenic mice developed at early age bilateral poorly differentiated carcinomas and frequently ascites in the abdominal cavity. However, the MISIIR promoter is not specific to the OSE leading to neoplastic lesions in other organs. In addition, MISIIR expression is also evident during early embryonic development resulting in cancer at early adult life, which is unlike ovarian carcinogenesis in women. Most importantly, through alternative splicing, SV40 early region encodes several viral proteins including small t and 17kT antigens in addition to large T. Binding reactions of these proteins result in inactivation of all RB family members including p107 and p130, both are rarely mutated in human malignancies (Weinberg et al., 1991). Moreover, small t antigen has been implicated in pathogenesis of human neoplasms (Hahn and Weinberg, 2002).

Our mouse model has several improvements over other generated systems to study EOC in the mouse (Chapter 2). For one, intrabursal injection of AdCre removes the requirement for an OSE-specific promoter, of which none are currently known and unlike earlier studies (Orsulic et al., 2002), no virus treatments in tissue culture and transplantation procedures are required. Immunocompetent mice can be used reflecting more closely natural host responses. Importantly, our model allows conditional and temporal control of the initiating events which is important for modeling early stages of EOC induction. Furthermore, the cancer is initiated in adult mice, similarly to the EOC in humans. Since our original publication, the approach of intrabursal injection has been successfully used for demonstration of the role of K-RAS and PTEN in the initiation of endometrioid ovarian cancer (Dinulescu et al.,

2005). Deletion of tumor suppressors PTEN and APC in the OSE induced endometrioid adenocarcinomas (Wu et al., 2007) and the role of BRCA1 in preneoplastic lesions (Clark-Knowles et al., 2007) was demonstrated.

1.4.3 Applications of Mouse Models to Development of Imaging and Therapeutic Approaches. In vivo imaging of mouse cancers similarly can facilitate development and testing of new diagnostic and therapeutic approaches in preclinical settings. Noninvasive live imaging of neoplastic lesions allows for sequential measurements of different factors, as well as the effects of prospective therapeutic drugs. Various instrumentation have been developed for imaging mouse malignancies, including micro-positron emission tomography, single-photon emission computed tomography, magnetic resonance imaging, microcomputed tomography, bioluminescence imaging (BLI), whole-body fluorescence imaging, intravital microscopy, and ultrasound (Lyons et al., 2005). Furthermore, "biosensor" reporter mice were generated (Hoffman et al., 2009) expressing luciferase or fluorescent protein which can be detected in BLI. Specifically, luciferase or fluorescent protein can be fused with tissue-specific promoters, transcription factors, or responsive elements and via gene-targeting introduced into the mouse genome. Such approaches result in mouse models serving as biosensors to detect the activity of oncogenes or tumor suppressor genes and concomitant visualize processes during malignant transformation (Stell et al., 2007).

In the area of drug development and discovery, mouse models can be useful in evaluating the efficacy of novel anticancer drugs and in addition predicting chemotherapeutic responses, positive or negative. Studies with transgenic mouse models of multistage pancreatic islet cell cancer (RIP1-Tag2

mice) and prostate neoplasms (TRAMP mice) facilitated efficiency tests of angiogenesis inhibitors (Bergers et al., 1999; Huss et al., 2003) and brought insight into antiangiogenic drug prescription. Angiogenesis inhibitors are most effective at specific disease stages.

Combination chemotherapy is often required in cancer treatment and for testing the synergistic effects of reagents in pre-clinical trials, mouse models are valuable tools. Here experiments in GEM developing acute promyelomytic leukemia (APL) (Rego et al., 2000) initiated a new combination therapy with retinoic acid and arsenic trioxide for a subset of APL patients which is currently in clinical trials. These patients have a different genetic make up, causing the common retinoic acid therapy to fail. On the contrary, in cell culture experiments no synergistic efficacy of combination therapy was observed, confirming the value of mouse models in drug testing (Lallemand-Breitenbach et al., 1999).

Utilizing MPM/SHG as biomedical imaging technique I describe a method for studying cell motility in a living mammalian system in Chapter 3. Furthermore, the feasibility of in vivo laparoscopic MPM/SHG is demonstrated by using a "stick" objective lens on unfixed, unsectioned, und unstained tissues at a resolution comparable to that of routinely processed histological sections (Chapter 4).

1.5 Conclusions and Project Overview

The overall cure rate of approximately thirty percent for ovarian cancer patients has not changed over the past three decades. Despite current strategies to generate an effective screening process, only twenty percent of

ovarian neoplasms are diagnosed at early stages, when curable (Das and Bast, 2008). My project has been focused on the development of accurate sporadic mouse models of EOCs advancing the understanding of this malignancy and improvement of effective diagnostic and therapeutic methods.

Deficiency of tumor suppressor's *p53* and *RB* and overexpression of *C-MYC* oncogene or alterations in their respective pathways occur in about 50%, 30-60% and 30-40% of sporadic EOCs, respectively. Therefore, we have initiated development of several mouse models of EOC based on alterations of these genes (Fig. 1.1, *A-C* and Chapter 3, 4 and 7). We achieved this goal by development of the novel approach of intrabursal AdCre which allowed tissue - specific, spatial and temporal control of gene deletion in a sporadic manner (Chapter 2). Using this approach we demonstrated that conditional inactivation of *p53* and *Rb* in the OSE results in neoplasms that are mainly (97%) serous adenocarcinomas remarkably similar to those of human EOC. Furthermore, by using syngeneic OSE cell lines we found cooperation between p53 and RB deficiencies and C-MYC overexpression in EOC.

Secondly, I set out to develop biomedical imaging techniques for early EOC detection and diagnostic evaluation, on a sub-cellular level, where normal ovarian tissue could be compared to cancerous lesion (Fig. 1.2, *A, B* Chapters 4 and 5). Multiphoton microscopy imaging of malignancies expressing endogenous components and fluorescent proteins enables cells to be observed in great detail and greater depths within tissues (Shaner et al., 2005; Zipfel et al., 2003). In addition MPM was tested for the analysis of individual cell migration and motility in a time-lapse manner (Chapter 3), which could be useful in identifying tumor response to chemotherapy.

Figure 1.1 Modeling epithelial ovarian cancer (EOC) in the mouse. Outline of studies conducted with our EOC mouse models. ***1***, Tumor & Cell Biology. (*A*) Mouse ovarian polycystic tumor (arrow) and normal ovary (arrowhead). (*B)* Serous ovarian adenocarcinoma of the mouse. (*C)* Malignant ovarian surface epithelium syngeneic line OSN3, deficient for p53 and Rb and overexpressing C-MYC. ***2***, High-Resolution In Vivo Imaging. (*A)* Multiphoton Microscopy (MPM) imaging system set up. (*B)* Standard histology (left images , H&E staining) and MPM/Second Harmonic Generation (SHG) (right images) of human ovarian surface epithelium and poorly differentiated adenocarcinoma. Morphologically normal ovarian epithelium in the invaginations (top images, arrow) and simple cysts (top images, arrowhead). Atypical neoplastic cells forming glandular structure (bottom images, arrow) within desmoplastic stroma (bottom images, arrowhead). ***3***, Therapeutics Toxicity Test: (*A)* Layered nanohybrid (positively charged layers of magnesium-aluminum hydroxide, grey, incorporated molecules, red, and yellow). (*B)* Magnetic Resonance Imaging scanner. (*C)* MPM image of LNH incorporated into OSE 4 days after administration (green, arrow). ***4***, Stem Cell Location. (*A)* Immunohistochemical detection of stem cell marker ALDH1 on paraffin sections of the ovary (*A*, OV, ovary; U, uterus). (*B)* Insert from image (*A)*, ALDH1 is highly expressed in the hilum region of the ovary (arrow). (*C)* BrdU label retaining cells in the hilum region after 2 months chase (green fluorescent, arrow). (*D)* OSE sub-population of the hilum region develops conspicuous large OSE-Clones demonstrating greater *ex vivo* self-renewal potential compared to OSE of the anterior ovary region.

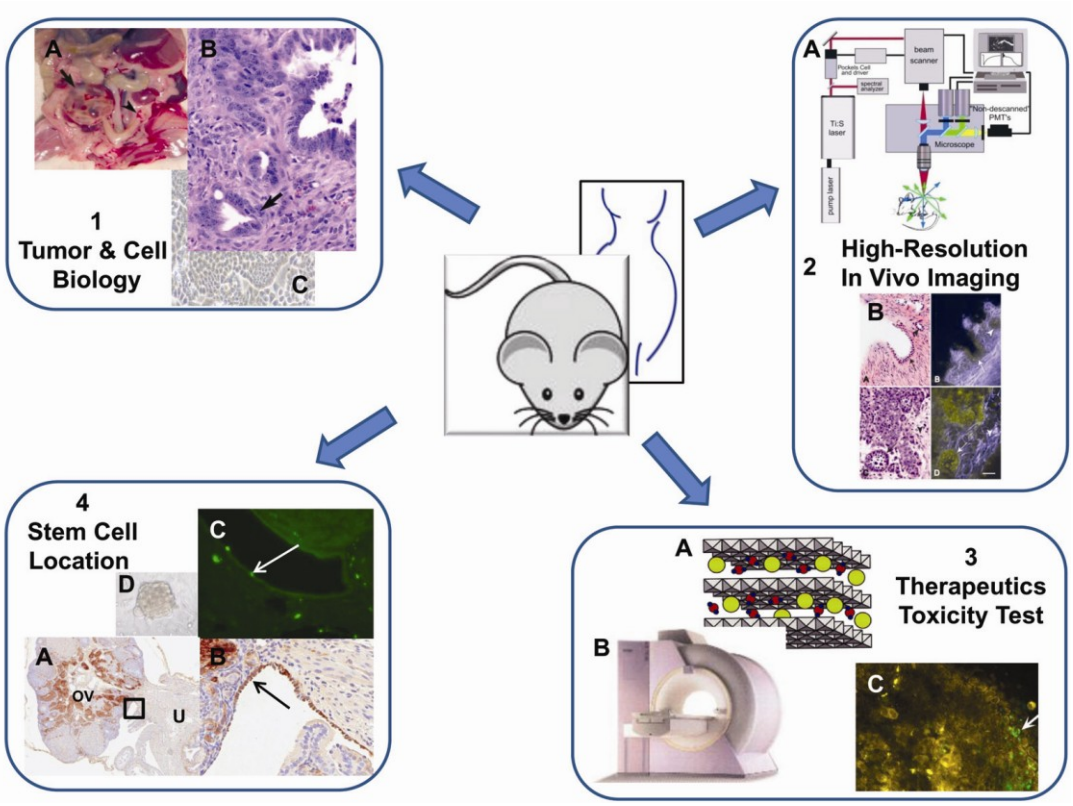
A
B
C
1
Tumor & Cell
Biology
A
beam
scanner
Ti:S
laser
Non-descanned
PMT's
Microscope
pump laser
2
High-Resolution
In Vivo Imaging
B
4
Stem Cell
Location
C
D
A
OV
U
B
A
3
Therapeutics
Toxicity Test
B
C

Improvement of treatment options has been the third objective of my studies. Layered nanohybrids are promising vehicles in controlled drug delivery. Although tested on glioma, choriocarcinoma cell lines and cardiac myocytes where they demonstrated little or no toxicity; these particles were not tested in the whole mammalian system. Therefore, we initiated research to evaluate the biological toxicity of LNH *in vivo* and potential applications of LNH for targeting OSE (Fig. 1.3, *A*-*C* and Chapter 5).

My final study is centered on the identification and functional characterization of adult ovarian surface epithelial stem cells. Accumulating evidence supports the notion that neoplastic cells in epithelial ovarian cancer may acquire molecular and cellular mechanisms typical for stem and progenitor cells (Alvero et al., 2009; Deng et al., 2010; Wei et al., 2010). Somatic stem cells reside in a specific niche, defined as the microenvironment. The niche hosts, shelters, and maintains stem cells (Moore and Lemischka, 2006). Characterizing the OSE stem cell niche and analyzing possible mechanisms which might distort the balance between stem cells and niche lays the essential basis for understanding EOC pathogenesis. (Fig. 1.4, *A*-*D* and Chapter 6).

REFERENCES

Adhikary, S., and Eilers, M. (2005). Transcriptional regulation and transformation by Myc proteins. Nat Rev Mol Cell Biol *6*, 635-645.

Ahmed, N., Thompson, E.W., and Quinn, M.A. (2007). Epithelial-mesenchymal interconversions in normal ovarian surface epithelium and ovarian carcinomas: an exception to the norm. J Cell Physiol *213*, 581-588.

Alvero, A.B., Chen, R., Fu, H.H., Montagna, M., Schwartz, P.E., Rutherford, T., Silasi, D.A., Steffensen, K.D., Waldstrom, M., Visintin, I.*, et al.* (2009). Molecular phenotyping of human ovarian cancer stem cells unravels the mechanisms for repair and chemoresistance. Cell Cycle *8*, 158-166.

Amati, B. (2001). Integrating Myc and TGF-beta signalling in cell-cycle control. Nat Cell Biol *3*, E112-113.

Auersperg, N., Pan, J., Grove, B.D., Peterson, T., Fisher, J., Maines-Bandiera, S., Somasiri, A., and Roskelley, C.D. (1999). E-cadherin induces mesenchymal-to-epithelial transition in human ovarian surface epithelium. Proc Natl Acad Sci U S A *96*, 6249-6254.

Auersperg, N., Wong, A.S., Choi, K.C., Kang, S.K., and Leung, P.C. (2001). Ovarian surface epithelium: biology, endocrinology, and pathology. Endocr Rev *22*, 255-288.

Auersperg, N., Woo, M.M., and Gilks, C.B. (2008). The origin of ovarian carcinomas: a developmental view. Gynecol Oncol *110*, 452-454.

Bast, R.C., Jr., Hennessy, B., and Mills, G.B. (2009). The biology of ovarian cancer: new opportunities for translation. Nat Rev Cancer *9*, 415-428.

Bergers, G., Javaherian, K., Lo, K.M., Folkman, J., and Hanahan, D. (1999). Effects of angiogenesis inhibitors on multistage carcinogenesis in mice. Science *284*, 808-812.

Blanpain, C., Horsley, V., and Fuchs, E. (2007). Epithelial stem cells: turning over new leaves. Cell *128*, 445-458.

Chang, H.L., MacLaughlin, D.T., and Donahoe, P.K. (2009). Somatic stem cells of the ovary and their relationship to human ovarian cancers. In StemBook, ed (The Stem Cell Research Community), pp. 1-16.

Chang, T.C., Wentzel, E.A., Kent, O.A., Ramachandran, K., Mullendore, M., Lee, K.H., Feldmann, G., Yamakuchi, M., Ferlito, M., Lowenstein, C.J., *et al.* (2007). Transactivation of miR-34a by p53 broadly influences gene expression and promotes apoptosis. Mol Cell *26*, 745-752.

Cheon, D.J., and Orsulic, S. (2011). Mouse models of cancer. Annu Rev Pathol *6*, 95-119.

Cho, K.R., and Shih Ie, M. (2009). Ovarian cancer. Annu Rev Pathol *4*, 287-313.

Clark-Knowles, K.V., Garson, K., Jonkers, J., and Vanderhyden, B.C. (2007). Conditional inactivation of Brca1 in the mouse ovarian surface epithelium results in an increase in preneoplastic changes. Exp Cell Res *313*, 133-145.

Connolly, D.C., Bao, R., Nikitin, A.Y., Stephens, K.C., Poole, T.W., Hua, X., Harris, S.S., Vanderhyden, B.C., and Hamilton, T.C. (2003). Female mice chimeric for expression of the simian virus 40 TAg under control of the MISIIR promoter develop epithelial ovarian cancer. Cancer Res *63*, 1389-1397.

Corney, D.C., Flesken-Nikitin, A., Choi, J., and Nikitin, A.Y. (2008). Role of p53 and Rb in ovarian cancer. Adv Exp Med Biol *622*, 99-117.

Corney, D.C., Hwang, C.I., Matoso, A., Vogt, M., Flesken-Nikitin, A., Godwin, A.K., Kamat, A.A., Sood, A.K., Ellenson, L.H., Hermeking, H., *et al.* (2010). Frequent downregulation of miR-34 family in human ovarian cancers. Clin Cancer Res *16*, 1119-1128.

Das, P., and Bast, R.C., Jr. (2008). Early detection of ovarian cancer. Biomarkers Med *2*, 291-303.

Davis, A.C., Wims, M., Spotts, G.D., Hann, S.R., and Bradley, A. (1993). A null c-myc mutation causes lethality before 10.5 days of gestation in homozygotes and reduced fertility in heterozygous female mice. Genes Dev *7*, 671-682.

Deng, S., Yang, X., Lassus, H., Liang, S., Kaur, S., Ye, Q., Li, C., Wang, L.P., Roby, K.F., Orsulic, S., *et al.* (2010). Distinct expression levels and patterns of stem cell marker, aldehyde dehydrogenase isoform 1 (ALDH1), in human epithelial cancers. PLoS One *5*, e10277.

Dinulescu, D.M., Ince, T.A., Quade, B.J., Shafer, S.A., Crowley, D., and Jacks, T. (2005). Role of K-ras and Pten in the development of mouse models of endometriosis and endometrioid ovarian cancer. Nat Med *11*, 63-70.

Evan, G.I., Wyllie, A.H., Gilbert, C.S., Littlewood, T.D., Land, H., Brooks, M., Waters, C.M., Penn, L.Z., and Hancock, D.C. (1992). Induction of apoptosis in fibroblasts by c-myc protein. Cell *69*, 119-128.

Fleming, J.S., Beaugie, C.R., Haviv, I., Chenevix-Trench, G., and Tan, O.L. (2006). Incessant ovulation, inflammation and epithelial ovarian carcinogenesis: revisiting old hypotheses. Mol Cell Endocrinol *247*, 4-21.

Frese, K.K., and Tuveson, D.A. (2007). Maximizing mouse cancer models. Nat Rev Cancer *7*, 645-658.

Fuchs, E., Tumbar, T., and Guasch, G. (2004). Socializing with the neighbors: stem cells and their niche. Cell *116*, 769-778.

Hahn, W.C., and Weinberg, R.A. (2002). Modelling the molecular circuitry of cancer. Nat Rev Cancer *2*, 331-341.

Hashiguchi, Y., Tsuda, H., Yamamoto, K., Inoue, T., Ishiko, O., and Ogita, S. (2001). Combined analysis of p53 and RB pathways in epithelial ovarian cancer. Hum Pathol *32*, 988-996.

Havrilesky, L.J., Alvarez, A.A., Whitaker, R.S., Marks, J.R., and Berchuck, A. (2001). Loss of expression of the p16 tumor suppressor gene is more frequent in advanced ovarian cancers lacking p53 mutations. Gynecol Oncol *83*, 491-500.

Hermeking, H. (2010). The miR-34 family in cancer and apoptosis. Cell Death Differ *17*, 193-199.

Hoess, R.H., Wierzbicki, A., and Abremski, K. (1986). The role of the loxP spacer region in P1 site-specific recombination. Nucleic Acids Res *14*, 2287-2300.

Hoffman, R.M. (2009). Imaging cancer dynamics in vivo at the tumor and cellular level with fluorescent proteins. Clin Exp Metastasis *26*, 345-355.

Honda, A., Hirose, M., Hara, K., Matoba, S., Inoue, K., Miki, H., Hiura, H., Kanatsu-Shinohara, M., Kanai, Y., Kono, T.*, et al.* (2007). Isolation, characterization, and in vitro and in vivo differentiation of putative thecal stem cells. Proc Natl Acad Sci U S A *104*, 12389-12394.

Horiuchi, A., Itoh, K., Shimizu, M., Nakai, I., Yamazaki, T., Kimura, K., Suzuki, A., Shiozawa, I., Ueda, N., and Konishi, I. (2003). Toward understanding the natural history of ovarian carcinoma development: a clinicopathological approach. Gynecol Oncol *88*, 309-317.

Huss, W.J., Barrios, R.J., and Greenberg, N.M. (2003). SU5416 selectively impairs angiogenesis to induce prostate cancer-specific apoptosis. Mol Cancer Ther *2*, 611-616.

Jemal, A., Siegel, R., Xu, J., and Ward, E. (2010). Cancer statistics, 2010. CA Cancer J Clin *60*, 277-300.

Jordan, V.C. (1977). Effects of tamoxifen in relation to breast cancer. Br Med J *1*, 1534-1535.

Katsaros, D., Cho, W., Singal, R., Fracchioli, S., Rigault De La Longrais, I.A., Arisio, R., Massobrio, M., Smith, M., Zheng, W., Glass, J.*, et al.* (2004). Methylation of tumor suppressor gene p16 and prognosis of epithelial ovarian cancer. Gynecol Oncol *94*, 685-692.

Kojima, K., Konopleva, M., Samudio, I.J., Shikami, M., Cabreira-Hansen, M., McQueen, T., Ruvolo, V., Tsao, T., Zeng, Z., Vassilev, L.T.*, et al.* (2005). MDM2 antagonists induce p53-dependent apoptosis in AML: implications for leukemia therapy. Blood *106*, 3150-3159.

Krarup, T. (1969). Oocyte destruction and ovarian tumorigenesis after direct application of a chemical carcinogen (9:0-dimethyl-1:2-benzanthrene) to the mouse ovary. Int J Cancer *4*, 61-75.

Kusume, T., Tsuda, H., Kawabata, M., Inoue, T., Umesaki, N., Suzuki, T., and Yamamoto, K. (1999). The p16-cyclin D1/CDK4-pRb pathway and clinical outcome in epithelial ovarian cancer. Clin Cancer Res *5*, 4152-4157.

Lallemand-Breitenbach, V., Guillemin, M.C., Janin, A., Daniel, M.T., Degos, L., Kogan, S.C., Bishop, J.M., and de The, H. (1999). Retinoic acid and arsenic synergize to eradicate leukemic cells in a mouse model of acute promyelocytic leukemia. J Exp Med *189*, 1043-1052.

Lengyel, E. (2010). Ovarian Cancer Development and Metastasis. The American Journal of Pathology *177*, 1053-1064.

Lyons, S.K. (2005). Advances in imaging mouse tumour models in vivo. J Pathol *205*, 194-205.

Marks, F., Furstenberger, G., and Muller-Decker, K. (2007). Tumor promotion as a target of cancer prevention. Recent Results Cancer Res *174*, 37-47.

Menon, U., Gentry-Maharaj, A., Hallett, R., Ryan, A., Burnell, M., Sharma, A., Lewis, S., Davies, S., Philpott, S., Lopes, A.*, et al.* (2009). Sensitivity and specificity of multimodal and ultrasound screening for ovarian cancer, and stage distribution of detected cancers: results of the prevalence screen of the UK Collaborative Trial of Ovarian Cancer Screening (UKCTOCS). Lancet Oncol *10*, 327-340.

Moore, K.A., and Lemischka, I.R. (2006). Stem cells and their niches. Science *311*, 1880-1885.

Nikitin, A.Y., and Hamilton, T. C. (2005). Modeling ovarian cancer in the mouse. RE Adv in Cancer, 2005 *5*, 49-59.

Noonan, F.P., Recio, J.A., Takayama, H., Duray, P., Anver, M.R., Rush, W.L., De Fabo, E.C., and Merlino, G. (2001). Neonatal sunburn and melanoma in mice. Nature *413*, 271-272.

Orsulic, S., Li, Y., Soslow, R.A., Vitale-Cross, L.A., Gutkind, J.S., and Varmus, H.E. (2002). Induction of ovarian cancer by defined multiple genetic changes in a mouse model system. Cancer Cell *1*, 53-62.

Plisiecka-Halasa, J., Karpinska, G., Szymanska, T., Ziolkowska, I., Madry, R., Timorek, A., Debniak, J., Ulanska, M., Jedryka, M., Chudecka-Glaz, A.*, et al.* (2003). P21WAF1, P27KIP1, TP53 and C-MYC analysis in 204 ovarian carcinomas treated with platinum-based regimens. Ann Oncol *14*, 1078-1085.

Rego, E.M., He, L.Z., Warrell, R.P., Jr., Wang, Z.G., and Pandolfi, P.P. (2000). Retinoic acid (RA) and As2O3 treatment in transgenic models of acute promyelocytic leukemia (APL) unravel the distinct nature of the leukemogenic process induced by the PML-RARalpha and PLZF-RARalpha oncoproteins. Proc Natl Acad Sci U S A *97*, 10173-10178.

Scully, R.E. (1999). Histological typing of ovarian tumours, Vol 9 (New York, Springer Berlin).

Shaner, N.C., Steinbach, P.A., and Tsien, R.Y. (2005). A guide to choosing fluorescent proteins. Nat Methods *2*, 905-909.

Sherr, C.J., and McCormick, F. (2002). The RB and p53 pathways in cancer. Cancer Cell *2*, 103-112.

Soriano, P. (1999). Generalized lacZ expression with the ROSA26 Cre reporter strain. Nat Genet *21*, 70-71.

Stell, A., Biserni, A., Della Torre, S., Rando, G., Ramachandran, B., Ottobrini, L., Lucignani, G., Maggi, A., and Ciana, P. (2007). Cancer modeling: modern imaging applications in the generation of novel animal model systems to study cancer progression and therapy. Int J Biochem Cell Biol *39*, 1288-1296.

Szotek, P.P., Chang, H.L., Brennand, K., Fujino, A., Pieretti-Vanmarcke, R., Lo Celso, C., Dombkowski, D., Preffer, F., Cohen, K.S., Teixeira, J.*, et al.* (2008). Normal ovarian surface epithelial label-retaining cells exhibit stem/progenitor cell characteristics. Proc Natl Acad Sci U S A *105*, 12469-12473.

Tachibana, M., Watanabe, J., Matsushima, Y., Nishida, K., Kobayashi, Y., Fujimura, M., and Shiromizu, K. (2003). Independence of the prognostic value

of tumor suppressor protein expression in ovarian adenocarcinomas: A multivariate analysis of expression of p53, retinoblastoma, and related proteins. Int J Gynecol Cancer *13*, 598-606.

Takahashi, K., and Yamanaka, S. (2006). Induction of pluripotent stem cells from mouse embryonic and adult fibroblast cultures by defined factors. Cell *126*, 663-676.

Tuveson, D., and Hanahan, D. (2011). Translational medicine: Cancer lessons from mice to humans. Nature *471*, 316-317.

Vennstrom, B., Sheiness, D., Zabielski, J., and Bishop, J.M. (1982). Isolation and characterization of c-myc, a cellular homolog of the oncogene (v-myc) of avian myelocytomatosis virus strain 29. J Virol *42*, 773-779.

Wang, L., Wu, Q., Qiu, P., Mirza, A., McGuirk, M., Kirschmeier, P., Greene, J.R., Wang, Y., Pickett, C.B., and Liu, S. (2001). Analyses of p53 target genes in the human genome by bioinformatic and microarray approaches. J Biol Chem *276*, 43604-43610.

Wei, X., Dombkowski, D., Meirelles, K., Pieretti-Vanmarcke, R., Szotek, P.P., Chang, H.L., Preffer, F.I., Mueller, P.R., Teixeira, J., MacLaughlin, D.T.*, et al.* (2010). Mullerian inhibiting substance preferentially inhibits stem/progenitors in human ovarian cancer cell lines compared with chemotherapeutics. Proc Natl Acad Sci U S A *107*, 18874-18879.

Weinberg, R.A. (1991). Tumor suppressor genes. Science *254*, 1138-1146.

Weissman, I.L., Anderson, D.J., and Gage, F. (2001). Stem and progenitor cells: origins, phenotypes, lineage commitments, and transdifferentiations. Annu Rev Cell Dev Biol *17*, 387-403.

Wu, R., Hendrix-Lucas, N., Kuick, R., Zhai, Y., Schwartz, D.R., Akyol, A., Hanash, S., Misek, D.E., Katabuchi, H., Williams, B.O.*, et al.* (2007). Mouse model of human ovarian endometrioid adenocarcinoma based on somatic defects in the Wnt/beta-catenin and PI3K/Pten signaling pathways. Cancer Cell *11*, 321-333.

Wu, X., and Levine, A.J. (1994). p53 and E2F-1 cooperate to mediate apoptosis. Proc Natl Acad Sci U S A *91*, 3602-3606.

Zipfel, W.R., Williams, R.M., Christie, R., Nikitin, A.Y., Hyman, B.T., and Webb, W.W. (2003). Live tissue intrinsic emission microscopy using multiphoton-excited native fluorescence and second harmonic generation. Proc Natl Acad Sci U S A *100*, 7075-7080.

CHAPTER 2

INDUCTION OF CARCINOGENESIS BY CONCURRENT INACTIVATION OF P53 AND RB1 IN THE MOUSE OVARIAN SURFACE EPITHELIUM*

2.1 Abstract

Alterations in p53 and Rb pathways are frequently observed in epithelial ovarian cancer (EOC). However, their roles in EOC initiation remain uncertain. Using a single intrabursal administration of recombinant adenovirus expressing Cre, we demonstrate that concurrent inactivation of *p53* and *Rb1* is sufficient for reproducible induction of ovarian epithelial carcinogenesis in mice homozygous for conditional gene alleles. Similarly to progression of disease in women, ovarian neoplasms spread intraperitoneally, forming ascites, and metastasize to the contralateral ovary, the lung, and the liver. These results establish critical interactions between p53 and Rb1 pathways in EOC pathogenesis, and provide a genetically defined immunocompetent mouse model of sporadic EOC.

2.2 Introduction

Ovarian cancer is the fifth leading female cancer among both new cancer cases and deaths in the United States (Jemal et al., 2003). Almost 90% of cases are believed to be derived from the ovarian surface epithelium (OSE), with serous adenocarcinomas comprising about 80% of EOC (Scully et al., 1996). By the time of diagnosis approximately 70% of tumors have spread beyond the ovary, and such cases are rarely curable by existing treatment schemes. Accordingly, over the past three decades the incidence and survival

*Previously published as Flesken-Nikitin et al., (2003). Cancer Research. 63: 3459-3463.

of ovarian cancer have remained relatively constant (Jemal et al., 2003). Unfortunately, development of accurate genetic mammalian models of EOC has been significantly delayed, in large part due to absence of promoters with expression limited to the OSE. Recently, two approaches have been reported. The first is based on the avian retroviral receptor TVA-replication-competent avian leukosis virus-derived vector (TVA-RCAS) gene delivery technique for introduction of defined alterations in explanted OSE with subsequent induction of tumor formation after injection of infected cells at subcutaneous, intraperitoneal, or ovarian sites of immunodeficient mice (Orsulic et al., 2002). The second uses the MISIIR receptor regulatory element for expression of the SV40 T antigen (TAg). Although insightful, these approaches either require *ex vivo* manipulations or result in transgene expression during embryonic development, dissimilar to the expected natural history of EOC in women. Mutations of *p53* gene are reported to be the most frequent alterations in sporadic EOC (Aunoble et al., 2000; Feeley and Wells, 2001), but initiate few, if any, carcinomas alone (Orsulic et al., 2002). p53 signaling is frequently interconnected with *Rb*-mediated pathways (Hahn and Weinberg, 2002; Sherr and McCormick, 2002). Aberrations in the Rb pathway in EOC have been suggested by a number of recent studies (Connolly et al., 2003; Gras et al., 2001; Hashiguchi et al., 2001; Havrilesky and Berchuck, 2001), however, direct genetic evidence for their contribution to EOC formation has been missing. To circumvent promoter-related limitations we have established a procedure for intrabursal administration of the recombinant adenovirus, taking advantage of the enclosed anatomical location of the mouse ovary within the bursa, which allows for selective exposure of the OSE to inducing agents. Using this approach in conjunction with Cre-*loxP*- mediated gene inactivation

we have directly evaluated role of *p53* and *Rb1* inactivation in the initiation of ovarian epithelial carcinogenesis.

2.3. Material and Methods

Experimental Animals. Mice with floxed copies of *p53* and *Rb1* genes were described elsewhere (Jonkers et al., 2001; Marino et al., 2000). *Rosa26STOPfloxLacZ* reporter mice (B6;129-Gt(ROSA)26SorT^{M1sor}) (Chai et al., 2000; Jiang et al., 2000; Soriano et al., 1999) were purchased from the Jackson Laboratory. In these mice, expression of bacterial β-galactosidase is possible only after deletion of a stop codon flanked by *loxP* sites. All mice were maintained identically, following recommendations of the Institutional Laboratory Animal Use and Care Committee.

Genotyping. All mice with floxed alleles were maintained in homozygous status. If necessary, PCR genotyping was performed essentially as described (Nikitin and Lee, 1996). *p53^{floxP}* mice were identified with primers 10FM5' (5' AAG CTG AAG ACA GAA AAG GGG AGG G 3') and 10RM3' (5' AAG CTA AGG GGT ATG AGG GAC AAG G 3') or 10RM23' (5' ACA GAA AAG GGG AGG GAT GAA GTG A3'). PCR amplification of wild-type and floxed *p53* gene sequences results in 163-bp and 316-bp DNA fragments, respectively, using 10FM5' and 10RM3' or in 432-bp and 585-bp, respectively, using 10FM5' and 10RM23'. Cre-mediated excision was detected as either 198-bp or 467-bp DNA fragment upon amplification with primers 1FM5' (5'GTG CCC TCC GTC CTT TTT CGC AAT C 3') and 10RM3' or 10RM23', respectively. *Rb1^{floxP}* mice were identified with primers Rb18M3' (5'- GGA ATT CCG GCG TGT GCC ATC AAT G 3') and Rb19EM5' (5' AGC TCT CAA GAG CTC AGA CTC ATG

G 3'). PCR amplification of wild-type and floxed *Rb1* gene sequences results in 247-bp and 295-bp DNA fragments, respectively. Cre-mediated excision was detected as a 269-bp DNA fragment upon amplification with primers Rb212M5' (5' CGA AAG GAA AGT CAG GGA CAT TGG G 3') and Rb18M3'.

Primary Culture of OSE. Individual ovaries were dissected and placed in DMEM/F12 (Ham's) medium containing Collagenase-Dispase at 5% CO_2 for 1 hr. OSE were placed in six-well plates covered with 0.1% gelatin, maintained in Ham's medium supplemented with 5% fetal bovine serum, 2 mM L-glutamine, 1 mM sodium pyruvate, 10 ng/ml EGF, 500 ng/ml hydrocortisone, 5 *μg*/ml insulin, 5 *μg*/ml transferrin, and 5 ng/ml sodium selenite, and passaged upon confluence. For estimation of proliferation index cells were incubated with 100 μM BrdU for 2 hr in cell culture incubator (37°C), washed with PBS three times 1 min each on ice, fixed with 4% paraformaldehyde for 30 min on ice, washed with PBS, 2 X 3 min, and processed for BrdU staining starting with ddH_2O rinse followed by 4N HCl as described in the Pathological Analyses.

Adenoviruses. Recombinant adenoviruses Ad*CMVLacZ*, Ad*CMVEGFP*, and Ad*CMVCre* are modifications of the adenovirus-5 genome, from which the e1a and e1b regions required for viral replication had been deleted and replaced with *Escherichia coli LacZ* or enhanced green fluorescent protein (EGFP) or Cre driven by the CMV immediate early regulatory sequence (Ad*CMVLacZ*, Ad*CMVEGFP*, and Ad*CMVCre*, respectively). Viruses purified as described (Anderson et al., 2000) were titered at 10^{11}–10^{12} infectious particles/ml, and frozen in small aliquots.

Adenovirus Administration. Pilot titration experiments demonstrated that infection at MOI 100 and 400-1000 resulted in lower infectivity or excessive cell damage, respectively (data not shown). Thus, for all subsequent cell culture ~ 2 x 10^5 OSE cells were incubated in 1 ml of serum-free medium with 4 x 10^7 Ad*CMVCre*, Ad*CMVEGFP* or Ad*CMVLacZ* pfu (MOI 200). After 2 hours at 37ºC, cells were washed twice with PBS and covered with complete medium containing 5% fetal bovine serum. Adenoviral delivery into the ovarian bursa was performed by injection with a Hamilton syringe and a 30-gauge beveled needle under the control of a dissection microscope after deep anesthesia with intraperitoneal (i.p.) Avertin (2.5% v/v in 0.85% NaCl, 0.020 ml/g body weight). Ovaries were accessed via dorsal incision, the needle was inserted into the oviduct near the infundibulum towards the bursa, and adenovirus (5 x 10^7 pfu/µl in PBS) was injected. According to our preliminary titration experiments using trypan blue and Ad*CMVEGFP* for injection to the bursa of 60-day old FVB/N females, a 10 µl volume is sufficient to fill the bursa entirely, yet without any significant leakage to the peritoneal cavity from the place of injection in > 95% of cases. This volume was used in all subsequent experiments.

Ovulation and Carcinogenesis Studies. To synchronize ovulation, 60-day-old females were mated with vasectomized males and the first day after ovulation was considered complete at midnight of the day after mating. Postnatal day 1 was considered completed 24 h after birth. Ad*CMVCre* and Ad*CMVLacZ* were injected into the bursa of the right and left ovary, respectively, of $p53^{floxP/floxP}$, $Rb1^{floxP/floxP}$, $p53^{floxP/floxP}Rb^{floxP/floxP}$ and wild type mice 1.5 days after ovulation.

To exclude possible inadvertent effects of mixed genetic background, all mice were kept on FVB/N background.

Microdissection PCR. Frozen and paraffin sections were placed on foil attached to glass slides, stained with H&E, and evaluated under microscope. Identified lesions as well as single cells were dissected either manually or with UV laser (Laser Microdissection System; Leica) and collected into caps of Eppendorf tubes filled with lysis buffer. DNA was isolated and processed essentially as described earlier (Nikitin and Lee, 1996).

Pathological Analyses. Moribund mice in long term-experiments, as well as those to be sacrificed according to schedule, were anesthetized with avertin, and, after cardiac perfusion at 90 mmHg with PBS followed by phosphate-buffered 4% paraformaldehyde, were subjected to gross pathology evaluation. Ovaries and other affected organs were removed, processed for preparing paraffin sections and characterized by microscopic evaluation. Serial sections were prepared for confirmation of neoplastic invasion. Pathology studies were performed by one of us (A.Y.N.) according to existing human and mouse EOC classifications (Davis et al., 2001; Nikitin et al., 2003; Scully et al., 1996). Immunohistochemical analysis of paraffin sections of paraformaldehyde-fixed tissue was performed by a modified ABC technique (Nikitin and Lee, 1996). The antibodies to EGFP (Living colors A.v. rabbit peptide antibody; 1:100 dilution, Clontech), cytokeratin 8 (CK8 TROMA-1 antibody, 1:50, Developmental Studies Hybridoma Bank, University of Iowa, Iowa City, IA) or BrdU, (Pharmingen; 1:100), were incubated with deparaffinized sections for 1 hour at room temperature. Ten-min boiling in 10 mM citric buffer was used for

antigen retrieval for detection of CK8. Rates of cell proliferation were evaluated by BrdU uptake according to earlier established protocols (Nikitin et al., 2002). At least 150 cells per field in 10 fields were scored for each tissue section. Detection of bacterial β-galactosidase was performed according to published protocols (Bonnerot and Nicolas, 1993; Fire et al., 1992; MacGregor et al., 1991).

Statistical Analyses. InStat 3.03 and Prism 3.02 (GraphPad, Inc. San Diego, CA) software was used in this study. Survival fractions were calculated using the Kaplan-Meier method. Survival curves were compared by log rank Mantel-Haenszel tests. Means were compared by estimation of the two-tailed *P* value with Mann-Whitney test.

2.4. Results and Discussion

To test the efficacy of recombinant adenovirus infection, primary cultures of OSE (Fig. 2.1*A*) were prepared, and cells were infected with adenovirus containing the EGFP encoding gene under control of the CMV promoter (Ad*CMVEGFP*) at a MOI of 200 infectious particles per cell. More than 80% of OSE cells expressed EGFP 24 h after infection (Fig. 2.1*B*). Similar results were also observed in cultured OSE of *Rosa26STOP^{floxP}LacZ* [B6;129-Gt(ROSA)26Sor^{TM1sor}] reporter mice (Chai et al., 2000; Jiang et al., 2000; Soriano et al., 1999) after infection with Ad*CMVCre* (data not shown). Accordingly, administration of Ad*CMVCre* to OSE cells carrying *p53$^{floxP/floxP}$* and/or *Rb1$^{floxP/floxP}$* resulted in inactivation of the respective gene(s) (Fig. 2.1, *C* and *D*). According to 5'-bromodeoxyuridine (BrdU) incorporation assay OSE

Figure 2.1 Targeting ovarian surface epithelium (OSE) by recombinant adenovirus in the primary culture. (*A)* Cytokeratin 8 expression in OSE after three passages. TROMA-1 antibody, ABC Elite method. (*B)* EGFP expression (green fluorescence) in the majority of OSE three days after infection. Counterstaining with DAPI (blue nuclear fluorescence). Calibration bar, *A*, 50 *μ*m, *B*, 100 *μ*m. *C* and *D*, PCR analysis of *p53* (*C*) and *Rb1* (*D*) gene structure in OSE containing either wild-type (*Lane 1*) or *floxP*/*floxP* (*Lanes 2 - 4*) gene 3 days after either Ad*CMVCre* (Cre +) or mock (Cre-) infection. (*C)* PCR with primers 10FM5' and 10RM3' results in 163 bp and 316 bp fragments for wild-type and floxed *p53* alleles, respectively. PCR with primers 1FM5' and 10RM3' detects 198 bp fragment diagnostic for Cre-mediated gene excision. (*D)* PCR with primers Rb19EM5' and Rb18M3' result in 247 bp and 295 bp fragments for wild-type and floxed *Rb1* alleles, respectively. PCR with primers Rb212M5' and Rb18M3' detects 269 bp fragment diagnostic for Cre-mediated gene excision. The bands about 850 bp (*Lane 1*) and 900 bp (*Lanes 2* and *4*) are the result of specific amplification of exon 19 and surrounding intron sequences without and with inserted loxP sites, respectively. (*C*, *D) Lane 5*, mock control. *Lane 6*, DNA marker. Three percent NuSieve agarose gels stained with ethidium bromide. (*E)* proliferation of OSE cells containing either $p53^{floxP/floxP}$ ($p53^{floxP}$), or $Rb1^{floxP/floxP}$ ($Rb1^{floxP}$) or $p53^{floxP/floxP}$, $Rb1^{floxP/floxP}$ ($p53^{floxP}$, $Rb1^{floxP}$), three (P3) and six (P6) passages after 2 hr exposure to 200 MOI of either Ad*CMVCre* (*Cre*) or Ad*CMVLacZ* (*LacZ*). According to semiquantitative PCR analyses > 90% of cells lost both functional copies of floxed genes 6 days after infection with Ad*CMVCre*. Cells were treated with BrdU for 2 h and BrdU indices (%, BrdUI, mean ± SD) was determined. Mann-Whitney test yielded two-tailed *P* values of <0.0001 for $p53^{floxP}$Cre versus

p53^{floxP}*LacZ* (18.25 ± 0.82, n = 12 versus 11.84 ± 0.62, n = 12) and *p53*$^{floxP/floxP}$, *Rb1*$^{floxP/floxP}$*Cre* versus *p53*$^{floxP/floxP}$*Cre* (54.94 ± 17.12, n = 11 versus 18.25 ± 0.82, n = 12) at passage 3, and 0.0206 and 0.0028 for *p53*^{floxP}*Cre* versus *p53*^{floxP}*LacZ* (21.00 ± 4.66, n = 11 versus 5.38 ± 3.20, n = 11) and for *Rb1*^{floxP}*Cre* versus *Rb1*^{floxP}*LacZ* (18.40 ± 3.50, n = 11, vs. 8.00 ± 1.6, n = 11), respectively, at passage 6. No significant differences was found among *p53*$^{floxP/floxP}$, *Rb1*$^{floxP/floxP}$, and *p53*$^{floxP/floxP}$, *Rb1*$^{floxP/floxP}$ OSE, exposed to Ad*CMVLacZ*, as well as wild-type OSE exposed to either Ad*CMVCre* or Ad*CMVLacZ* (data not shown).

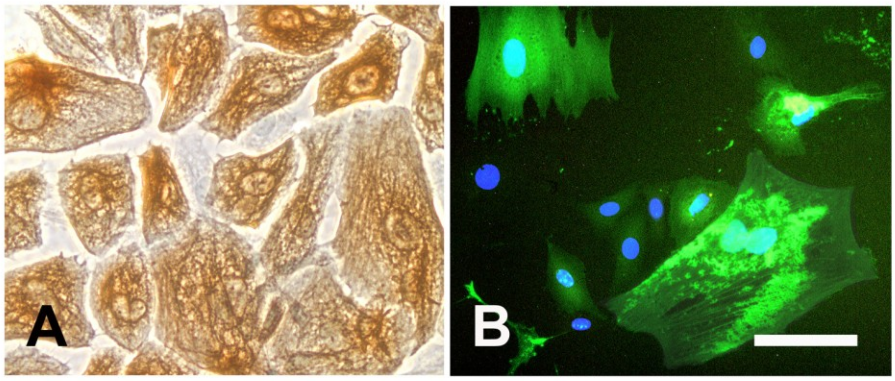
A
B

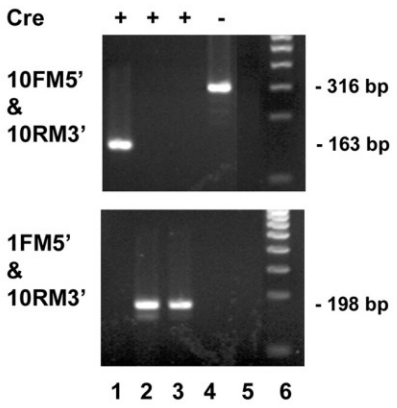
Cre
+ + + -
10FM5'
&
10RM3'
- 316 bp
- 163 bp
1FM5'
&
10RM3'
- 198 bp
1 2 3 4 5 6
C

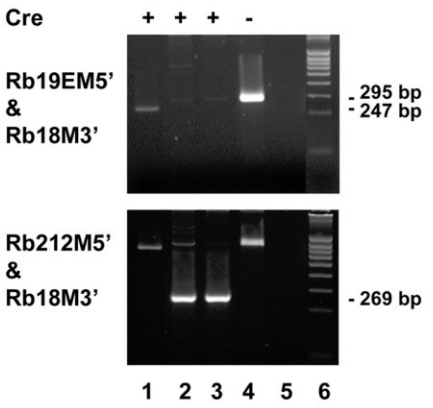
Cre
+ + + -
Rb19EM5'
&
Rb18M3'
- 295 bp
- 247 bp
Rb212M5'
&
Rb18M3'
- 269 bp
1 2 3 4 5 6
D

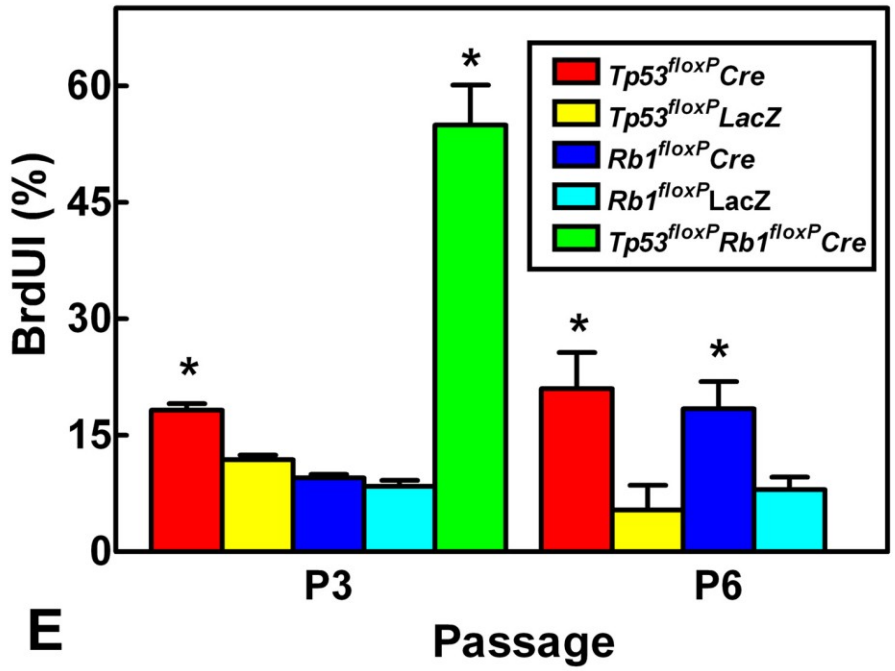
BrdUI (%)
60
45
30
15
0
*
*
*
*
Tp53floxPCre
Tp53floxPLacZ
Rb1floxPCre
Rb1floxPLacZ
Tp53floxPRb1floxPCre
P3
P6
Passage
E

proliferation was pronounced after the first passage following inactivation of both *p53* and *Rb1* (Fig. 2.1*E*; data and not shown). Modest but statistically significant increase in proliferation of OSE was evident three and six passages after individual inactivation of *p53* and *Rb1*, respectively (Fig. 2.1*E*). Taken together, these results indicate that recombinant adenovirus efficiently infects OSE, the CMV promoter is adequate for Cre expression in these cells, Cre-mediated inactivation of floxed *p53* and *Rb1* occurs after a single administration of AdCMVCre, and simultaneous inactivation of both genes results in dramatic increase of OSE proliferation.

To evaluate the feasibility of direct targeting of OSE by recombinant adenoviruses in the mouse, we have administered Ad*CMVEGFP* to the ovarian bursa. As determined by both fluorescence (Fig. 2.2, *A* and *B*) and immunostaining (Fig. 2.2, *C* and *D*), > 90% of OSE cells expressed EGFP 1 day after injection with Ad*CMVEGFP*. Notably no underlying stromal cells were infected. Expression ceased to be detected by the 21st day after administration, in agreement with the transient character of adenovirus infection. Similar results were obtained with the Ad*CMVLacZ* reporter (data not shown). To evaluate Cre-loxP-mediated gene deletion, Ad*CMVCre* was administered to OSE of *Rosa26STOP*^{floxP}*LacZ* mice (Chai et al., 2000; Jiang et al., 2000; Soriano et al., 1999). Consistent with Ad reporter experiments, *E.coli* β-galactosidase expression was detected only in OSE but to a somewhat lesser extent (about 60-80% of cells, Fig. 2.2, *E* and *F*). At the concentrations used no reactive hyperplasia or other pathological alterations were observed in OSE after infection with any of the applied recombinant adenoviruses. These results indicate that adenovirus can be used as an

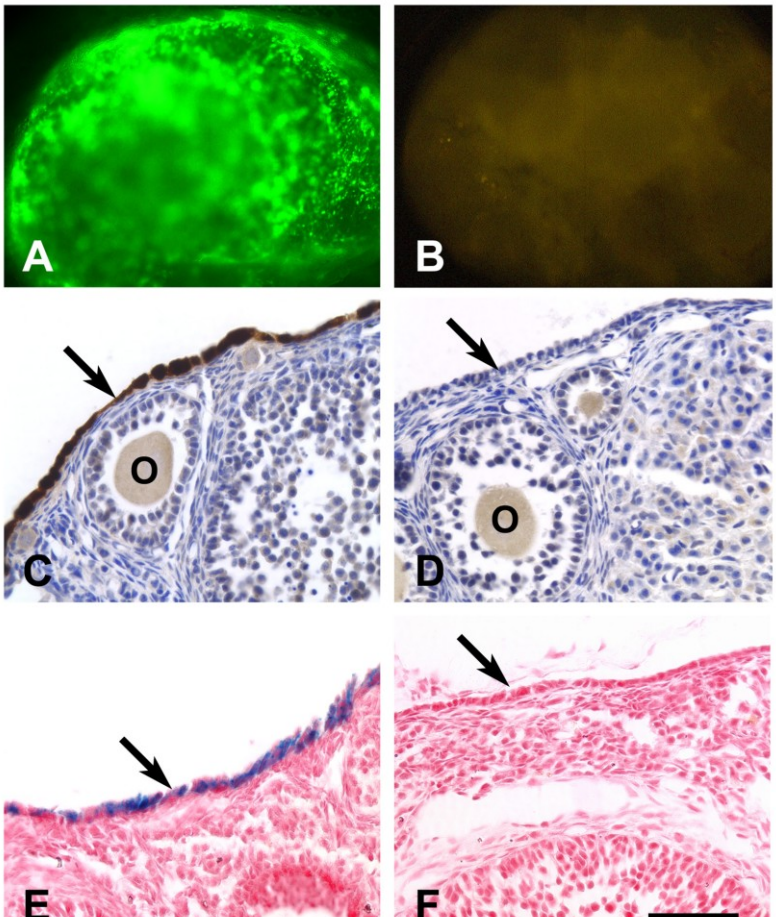

Figure 2.2 Targeting OSE by intrabursal administration of the recombinant adenovirus in the mouse. Wild type (*A-D*) and *R26STOPfloxLacZ* (*E* and *F*) mice were subjected to a single ovarian intrabursal injection with 5 x 10^7 pfu/μl of either Ad*CMVEGFP* (*A*, *C*, and *F*), Ad*CMVLacZ* (*B* and *D*) or Ad*CMVCre* (*E*). Ovaries were collected 3 days after injection and processed immediately for fluorescence (*A* and *B*), ABC immunostaining with rabbit anti-EGFP antibody (*C* and *D*) or histochemical detection of β-galactosidase (*E* and *F*). Arrow, OSE; *O*, oocyte. Counterstaining with Hematoxylin (*C* and *D*), and Nuclear Fast Red (*E* and *F*). Calibration bar, (*A* and *B*) 500 μm, (*C* and *D*) 50 μm.

efficient vector for selective induction of temporal localized gene expression in OSE. Thus, in conjunction with the Cre-LoxP system, this approach should be useful for OSE-targeted inactivation of floxed tumor suppressor genes, as well as for induction of oncogene expression in STOP^{floxP} designs such as *K-ras* (Jackson et al., 2001) and *neu/ErbB2* (Andrechek et al., 2000).

Both adenovirus infection efficacy and success in fixation of acquired genetic mutations increase in actively proliferating cells. Since in the adult mouse OSE proliferation is induced after ovulation, the peak of proliferation was determined in synchronized females (see "Materials and Methods"). Using BrdU incorporation assay, we identified the peak of proliferation at 1.5 days after ovulation (mean ± SD, 2.5 ± 0.3%; n = 3 *versus* 1.5 ± 0.3; n = 3 on day 1.5 and 3.5 after ovulation; P = 0.0034). Thus, in all subsequent experiments adenoviral administration was performed at 1.5 days after ovulation.

Thirty three out of 34 mice (97%) with inactivation of both genes succumbed to ovarian tumors at a median of 227 days (Fig. 2.3*A*, Table 1). In agreement with our pilot experiments indicating possible leakage of Ad*CMVCre* upon injection in ~5% of cases (see "Materials and Methods"), one tumor was not associated with ovary and had features of undifferentiated neoplasm (Table 2.1). At the same time, 4 out of 31 (13%) and 1 out of 29 (3%) mice developed tumors after Ad5Cre-mediated inactivation of floxed *p53* or *Rb1*, respectively. Among those tumors only 2 tumors in *p53*$^{floxP/floxP}$ mice arose from the ovary by 400 days after injection (Table 2.1). No tumors were observed after administration of Ad*CMVLacZ* And Ad*CMVCre* into the bursa of floxed (*p53*$^{floxP/floxP}$, *Rb1*$^{floxP/floxP}$, and *p53*$^{floxP/floxP}$*Rb1*$^{floxP/floxP}$) and wild-type

Figure 2.3 Survival and pathology of mice with conditional inactivation of *p53* and *Rb1* in OSE. *A*, survival of $p53^{floxP/floxP}$ (n = 31), $Rb1^{floxP/floxP}$ (n = 29), $p53^{floxP/floxP}Rb1^{floxP/floxP}$ (n = 34) and wild-type (n = 32) female mice after a single ovarian intrabursal injection of Ad*CMVCre*. Median survival for $p53^{floxP/floxP}Rb1^{floxP/floxP}$ mice was 227 days. (*B)* Abdominal distension (arrow) of the mouse with ovarian tumor. (*C)* Ovarian polycystic tumor (arrow) and normal ovary (arrowhead) of $p53^{floxP/floxP}Rb1^{floxP/floxP}$ mouse 255 days after a single intrabursal administration of Ad*CMVCre* and Ad*CMVLacZ*, respectively, into the right and left ovary. Low (*D*) and high (*E*) magnification of ovarian serous cystic adenocarcinoma with invasive growth (arrow). (*F)* Neoplastic OSE cells form papillary structures (arrow). (*G)* CK 8 is consistently detected in ovarian carcinoma cells arranged in invasive glandular structures and isolated groups (arrow) laying in dense fibrous tissue. *D-F*, H&E, *G*, immunohistochemical detection of CK 8 with TROMA-1 antibody, ABC elite method. Calibration bar, *B*, 21 mm; *C*, 68 mm; *D*; 180 *μ*m; *E-G*, 55 *μ*m.

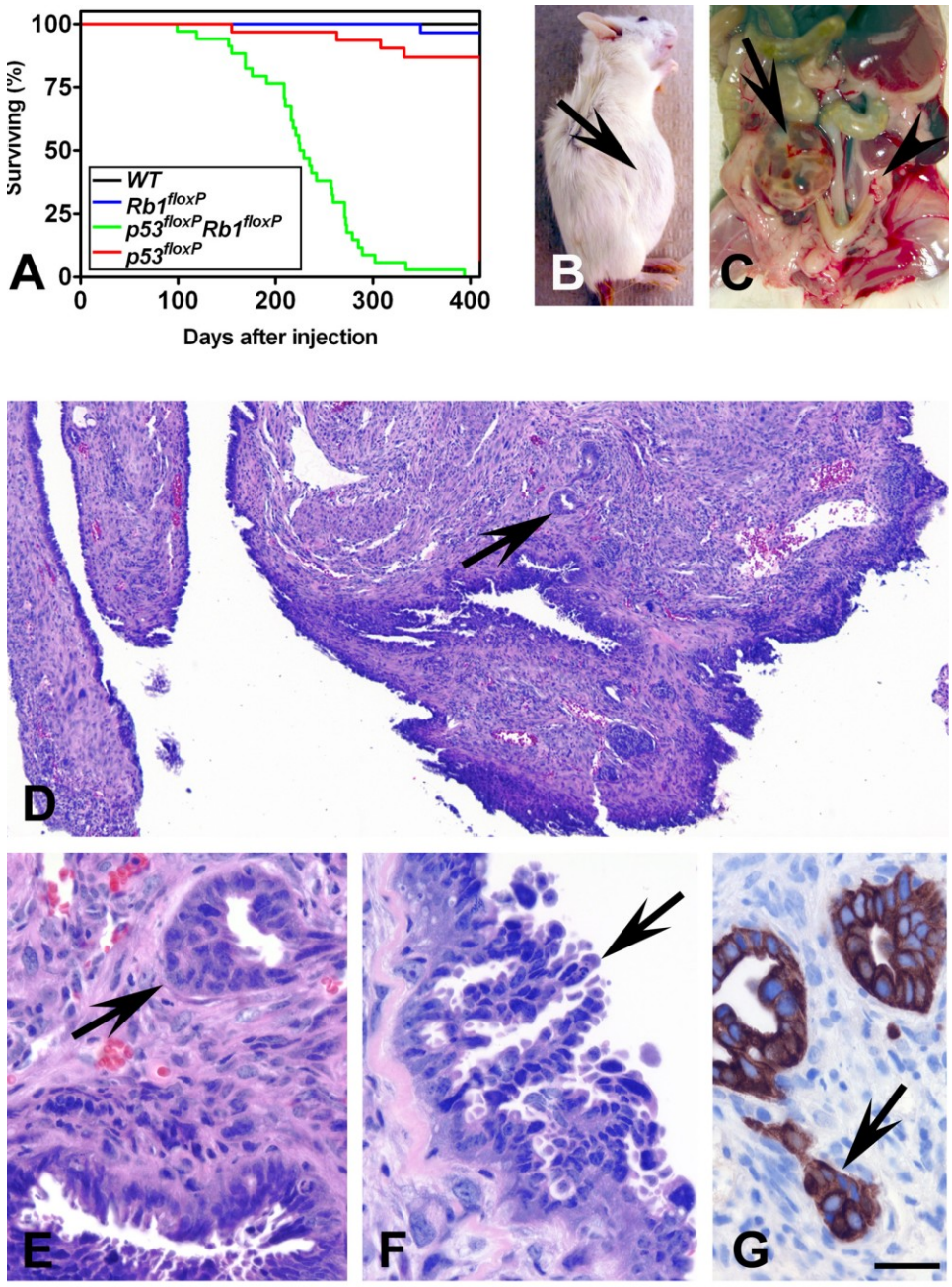
100
75
50
25
0
Surviving (%)
WT
Rb1floxP
p53floxPRb1floxP
p53floxP
A
0
100
200
300
400
Days after injection
B
C
D
E
F
G

Table 2.1 Ovarian neoplasms induced by a single intrabursal administration of Ad*CMVCre* to mice carrying conditional *p53* and/or *Rb1* alleles

Genotype	$p53^{floxP/floxP}$	$p53^{floxP/floxP}$ $Rb1^{floxP/floxP}$	$Rb1^{floxP/flox}$	Wild type
Mice with neoplasms, total, %[+]	13 (4/31)*	100 (34/34)	3 (1/29)	0 (0/32)
Mice with ovarian neoplasms, total %	6 (2/31)	97 (33/34)	0 (0/29)	0 (0/32)
Well differentiated serous epithelial neoplasms of the ovary, %	0 (0/2)	39 (13/33)	0 (0/0)	0 (0/32)
Poorly differentiated CK8-positive neoplasms of the ovary, %	100 (2/2)	45 (15/33)	0 (0/0)	0 (0/0)
Undifferentiated neoplasms of the ovary, %[#]	0 (0/2)	15 (5/33)	0 (0/0)	0 (0/0)
Peritoneal spreading, %	0 (0/2)	27 (9/33)	0 (0/0)	0 (0/0)
Ascites, %	0 (0/2)	24 (8/33)	0 (0/0)	0 (0/0)
Metastases in the contralateral ovary, %	0 (0/2)	15 (5/33)	0 (0/0)	0 (0/0)
Lung metastases, %	50 (1/2)	18 (6/33)	0 (0/0)	0 (0/0)
Liver metastases, %	0 (0/2)	3 (1/33)	0 (0/0)	0 (0/0)

[+]Non ovarian neoplasms were not physically associated with the ovary and included low differentiated spindle and polymorphic cell neoplasms without any morphological or immunohistochemical features of specific differentiation, such as expression of epithelial (CK8, Pan-cytokeratin), lymphoid (CD45R and CD3), smooth (smooth muscle actin) and striated (α-sarcomeric actin) muscle, histiocytic (F4/80) and schwannian (S100) markers. All neoplasms had no functional floxed gene(s) according to microdissection-PCR genotyping and were likely a result of rare inadvertent leakage of the AdCre during intrabursal administration.

*Numbers in parentheses indicate number of mice with neoplasm out of total number of mice.

[#]Neoplasms originating from the ovary but without any specific morphological or immunohistochemical features of differentiation (see comment to [+]). All neoplasms had loss of both floxed genes according to PCR genotyping.

Figure 2.4 Characterization of ovarian tumors induced by inactivation of *p53* and *Rb1*. (*A*, *B)* Poorly differentiated carcinoma consisting of epithelioid cells in loose trabecular formation (arrow) containing CK8 (*B*). (*C)* Intraperitoneal spreading of CK8 positive (arrow) neoplastic cells. (*D)* Liver metastasis (arrow) of poorly differentiated ovarian carcinoma. (*E)* Early dysplastic OSE lesions consisting of disorganized, ciliated (arrow) and vacuolated (arrowhead) atypical cells. (*F)* Flat OSE (arrow) 180 days after exposure to a single administration of Ad*CMVLacZ*. *A*, *D-F*, H&E. *B*, *C*, immunohistochemical detection of CK 8 with TROMA-1 antibody, ABC elite method. Calibration bar, *A-F*, 50 *μ*m. *G* and *H*, PCR analysis of *p53* (*G*) and *Rb1* (*H*) gene structure in the same sets of tissues (*Lanes 1*, *4*, and *7-11*) and primary cell cultures (*Lanes 2, 3, 5, 6*, *F* and *C*) samples collected from mice heterozygous (*Lane 1, H*), wild-type (*Lane 2, W*) and homozygous (*Lanes 3-11*) for both floxed gene without (*Lanes 3* and *4*, *F*) or with previous exposure to Ad*CMVCre* (*Lanes 5-11*, *C, N* and *E*). *N* and *E*, cells from ovarian neoplasms and early neoplastic lesions, respectively, collected by microdissection. *M* (*Lane 12*), mock control. PCR primers are as described in legend to the Fig. 1, with exception that all three primers were used simultaneously and 10RM23'primer was used instead 10RM3', resulting in 585-, 467-, and 433-bp fragments diagnostic for floxed, excised, and wild-type alleles of *p53* gene, respectively.

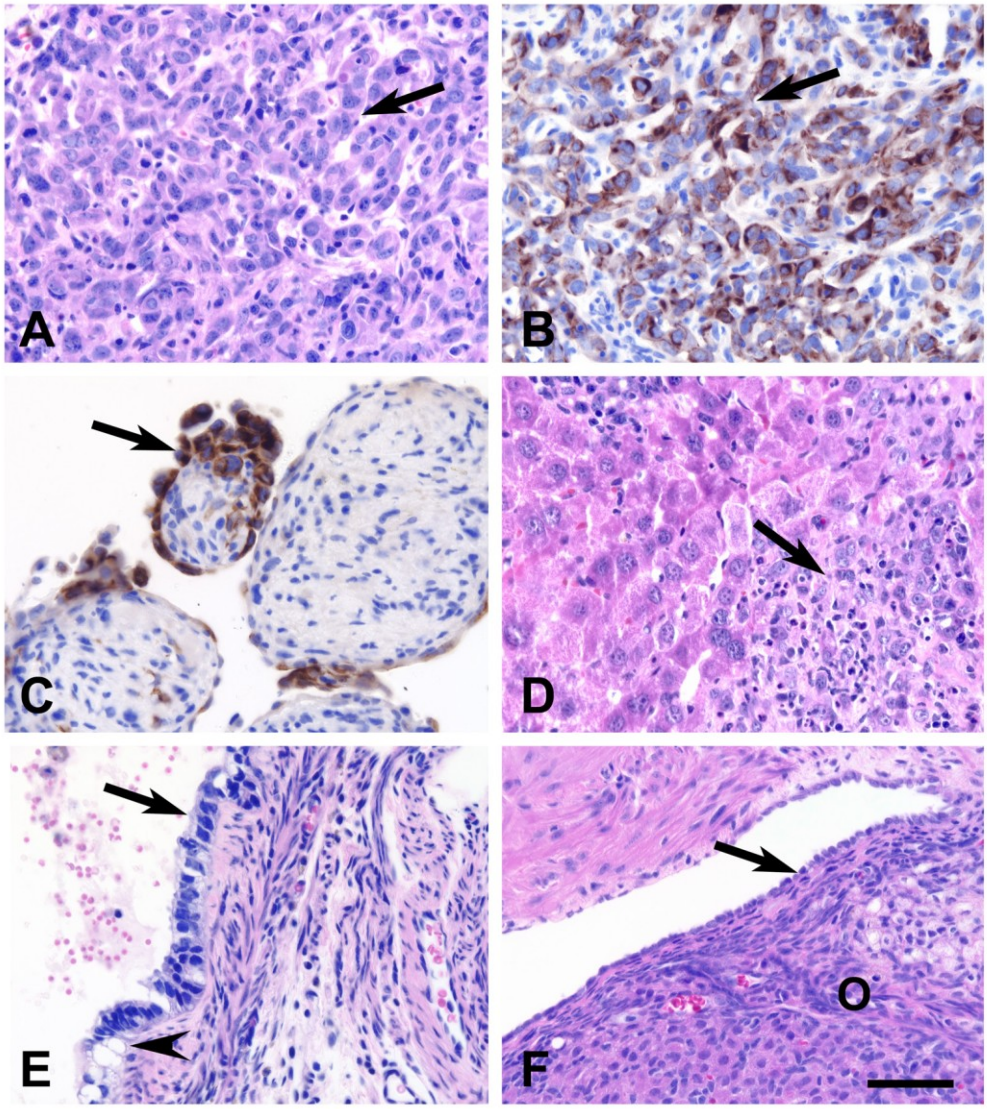
A
B
C
D
E
F
O

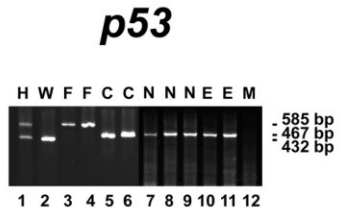
p53
H W F F C C N N N E E M
585 bp
467 bp
432 bp
1 2 3 4 5 6 7 8 9 10 11 12

G

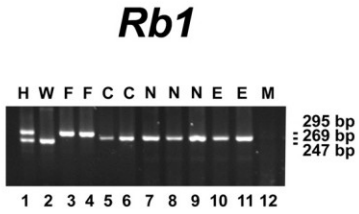
Rb1
H W F F C C N N N E E M
295 bp
269 bp
247 bp
1 2 3 4 5 6 7 8 9 10 11 12

H

mice, respectively. Grossly, the mice had abdominal distension (Fig. 2.3*B*). On necropsy polycystic tumor masses substituted the ovary and invaded surrounding tissues (Fig. 2.3*C*). Hemorrhagic or serous ascites were observed in 24% of the mice with ovarian tumors (Table 2.1).

Thirteen of 33 neoplasms that developed in the ovaries of $p53^{floxP/floxP}Rb1^{floxP/floxP}$ mice (39%) were composed of multiple serous cysts (Fig. 2.3*D*). These cysts were lined by crowded neoplastic epithelial cells with large hyperchromatic nuclei and small round to polygonal cytoplasm (Fig. 2.3, *E* and *F*). Neoplastic cells formed papillary structures (Fig. 2.3*F*), invaded underlying tissues (Fig. 2.3, *D*-*G*) and contained simple epithelium-specific cytokeratin 8 (CK8; Fig. 2.3*G*). Fifteen neoplasms (45%) were poorly differentiated and consisted of CK 8-positive epithelioid cells, which sometimes formed trabecular structures (Fig. 2.4, *A* and *B*). Tumors expanded i.p. (27%, Fig. 2.4*C*), formed ascites containing groups of neoplastic cells (24% of cases), and metastasized to the opposite ovary (15%), the lung (18%) and the liver (6%, Fig. 2.4*D*). Taken together, both pathology and biological behavior of induced neoplasms were remarkably similar to those of human EOC, particularly to its most common type, serous adenocarcinoma. Furthermore, in close concordance with human EOC, these neoplasms are induced in adult mice.

Microdissection-PCR confirmed loss of both copies of both *Rb1* and *p53* in the neoplastic cells of all 19 cases tested (Fig. 2.4, *G* and *H*; data not shown). Notably, loss of both genes was detected in early dysplastic lesions (Fig. 2.4, *E*, *G*, and *H*). No similar alterations were observed in the other ovary exposed to Ad*CMVLacZ* (Fig. 2.4*F*). Simultaneous Cre-LoxP-mediated recombination may result in rearrangements between chromosomes 11 (*p53*)

and 14 (*Rb1*) with potential influence on carcinogenesis. No such alterations were detected after PCR with four combinations of primers flanking *Rb1* (Rb212 and Rb18M3') and *p53* (1FM5' and 10RM3') loxP sites (not shown). Thus, inter-chromosomal rearrangements are unlikely to have a selective advantage in this model.

Formation of a small number of epithelial tumors in $p53^{floxP/floxP}$ mice alone indicates that p53 may be sufficient for initiation of OSE carcinogenesis. However, the complete effect of its inactivation is evident only in cooperation with alterations in the Rb pathway. These results support earlier studies which indicated that oncogenic transformation of OSE is easily achieved by cooperation of p53 inactivation with activation of c-myc, K-ras and Akt (Orsulic et al., 2002) or by inactivation of p53, Rb and PP2A pathways by SV40 T antigen (Connolly et al., 2003). Notably, both Akt and K-ras are involved in RB network signaling by regulating cyclin D1 activity (Sherr and McCormick, 2002). It is of note, that some genetic alterations preferentially occur in specific EOC subtypes such as serous (Aunoble et al., 2000; Morita et al., 2000), mucinous (Cuatrecasas et al., 1997; Morita et al., 2000) and endometrioid (Aunoble et al., 2000; Feeley and Wells, 2001; Havrilesky and Berchuck, 2001). Interestingly, carcinomas of the serous subtype more frequently have RB1 loss of heterozygosity and aberrant immunostaining (Gras et al., 2001), in close agreement with the observation of serous neoplasms in our model. Additional studies shall allow understanding of particular involvement of other genetic pathways, including c-MYC, AKT-2, PIK3CA, HER2/NEU, and EEF1A2. A small subset of hereditary cases are associated with alterations in tumor susceptibility genes BRCA1 and BRCA2 (Boyd et al., 2000). Mutations in BRCA1 and BRCA2 are rare in sporadic cases. However, recent studies

indicate that Rb1 interacts with BRCA1 (Deng and Brodie, 2000). Taken together, our experiments have established a genetically defined and phenotypically accurate model of EOC and have provided direct genetic evidence that defects in p53 and Rb1-mediated pathways may cooperate in ovarian carcinogenesis. These results furnish both rationale and suitable modeling means for development and testing of diagnostic, therapeutic and preventive approaches aimed at p53 and Rb1 signaling circuits in EOC.

REFERENCES

Anderson, R.D., Haskell, R.E., Xia, H., Roessler, B.J., and Davidson, B.L. (2000). A simple method for the rapid generation of recombinant adenovirus vectors. Gene Ther *7*, 1034-1038.

Andrechek, E.R., Hardy, W.R., Siegel, P.M., Rudnicki, M.A., Cardiff, R.D., and Muller, W.J. (2000). Amplification of the neu/erbB-2 oncogene in a mouse model of mammary tumorigenesis. Proc Natl Acad Sci U S A *97*, 3444-3449.

Aunoble, B., Sanches, R., Didier, E., and Bignon, Y.J. (2000). Major oncogenes and tumor suppressor genes involved in epithelial ovarian cancer (review). Int J Oncol *16*, 567-576.

Bonnerot, C., and Nicolas, J.F. (1993). Application of LacZ gene fusions to postimplantation development. Methods Enzymol *225*, 451-469.

Boyd, J., Hamilton, T.C., and Berchuck, A. (2000). Oncogenes and tumor-suppressor genes. In Principles and Practice of Gynecologic Oncology, W. Hoskins, C. Perez, and R. Young, eds. (Philadelphia, Lippincott, Williams & Wilkins).

Chai, Y., Jiang, X., Ito, Y., Bringas, P., Han, J., Rowitch, D.H., Soriano, P., McMahon, A.P., and Sucov, H.M. (2000). Fate of the mammalian cranial neural crest during tooth and mandibular morphogenesis. Development *127*, 1671-1679.

Connolly, D.C., Bao, R., Nikitin, A.Y., Stephens, K.C., Poole, T.W., Hua, X., Harris, S.S., Vanderhyden, B.C., and Hamilton, T.C. (2003). Female mice chimeric for expression of the SV40 TAg under control of the MISIIR promoter develop epithelial ovarian cancer. Cancer Res *63*, 1389-1397.

Cuatrecasas, M., Villanueva, A., Matias-Guiu, X., and Prat, J. (1997). K-ras mutations in mucinous ovarian tumors: a clinicopathologic and molecular study of 95 cases. Cancer *79*, 1581-1586.

Davis, B., Harleman, J.H., Heinrichs, M., Maekawa, A., McConnell, R.F., Reznik, G., and Tucker, M. (2001). Female Genital System. In International Classification of Rodent Tumors The Mouse, U. Mohr, ed. (Berlin, Springer), pp. 211-268.

Deng, C.X., and Brodie, S.G. (2000). Roles of BRCA1 and its interacting proteins. Bioessays *22*, 728-737.

Feeley, K.M., and Wells, M. (2001). Precursor lesions of ovarian epithelial malignancy. Histopathology *38*, 87-95.

Fire, A. (1992). Histochemical techniques for locating Escherichia coli beta-galactosidase activity in transgenic organisms. Gata *9*, 151-158.

Gras, E., Pons, C., Machin, P., Matias-Guiu, X., and Prat, J. (2001). Loss of heterozygosity at the RB-1 locus and pRB immunostaining in epithelial ovarian tumors: a molecular, immunohistochemical, and clinicopathologic study. Int J Gynecol Pathol *20*, 335-340.

Hahn, W.C., and Weinberg, R.A. (2002). Modelling the molecular circuitry of cancer. Nat Rev Cancer *2*, 331-341.

Hashiguchi, Y., Tsuda, H., Yamamoto, K., Inoue, T., Ishiko, O., and Ogita, S. (2001). Combined analysis of p53 and RB pathways in epithelial ovarian cancer. Hum Pathol *32*, 988-996.

Havrilesky, L.J., and Berchuck, A. (2001). Molecular alterations in sporadic ovarian cancer. In Ovarian Cancer, S.C. Rubin, and G.P. Sutton, eds. (Philadelphia, Lippincott, Williams & Wilkins), pp. 23-42.

Jackson, E.L., Willis, N., Mercer, K., Bronson, R.T., Crowley, D., Montoya, R., Jacks, T., and Tuveson, D.A. (2001). Analysis of lung tumor initiation and progression using conditional expression of oncogenic K-ras. Genes Dev *15*, 3243-3248.

Jemal, A., Murray, T., Samuels, A., Ghafoor, A., Ward, E., and Thun, M.J. (2003). Cancer statistics, 2003. CA Cancer J Clin *53*, 5-26.

Jiang, X., Rowitch, D.H., Soriano, P., McMahon, A.P., and Sucov, H.M. (2000). Fate of the mammalian cardiac neural crest. Development *127*, 1607-1616.

Jonkers, J., Meuwissen, R., van der Gulden, H., Peterse, H., van der Valk, M., and Berns, A. (2001). Synergistic tumor suppressor activity of BRCA2 and p53 in a conditional mouse model for breast cancer. Nat Genet *29*, 418-425.

MacGregor, G.R., and et al. (1991). Use of *E. Coli* lacZ (β-galactosidase) as a reporter gene. Gene Transfer and Expression Protocols *10*, 217-235.

Marino, S., Vooijs, M., van Der Gulden, H., Jonkers, J., and Berns, A. (2000). Induction of medulloblastomas in p53-null mutant mice by somatic inactivation of Rb in the external granular layer cells of the cerebellum. Genes Dev *14*, 994-1004.

Morita, K., Ono, Y., Fukui, H., Tomita, S., Ueda, Y., Terano, A., and Fujimori, T. (2000). Incidence of P53 and K-ras alterations in ovarian mucinous and serous tumors. Pathol Int *50*, 219-223.

Nikitin, A.Y., Connoly, D.C., and Hamilton, T.C. (2003). Pathology of ovarian neoplasms in genetically modified mice. Comparative Medicine, In press.

Nikitin, A.Y., and Lee, W.H. (1996). Early loss of the retinoblastoma gene is associated with impaired growth inhibitory innervation during melanotroph carcinogenesis in $Rb^{+/-}$ mice. Genes & Development *10*, 1870-1879.

Nikitin, A.Y., Liu, C.Y., Flesken-Nikitin, A., Chen, C.F., Chen, P.L., and Lee, W.H. (2002). Cell lineage-specific effects associated with multiple deficiencies of tumor susceptibility genes in Msh2(-/-)Rb(+/-) mice. Cancer Res *62*, 5134-5138.

Orsulic, S., Li, Y., Soslow, R.A., Vitale-Cross, L.A., Gutkind, J.S., and Varmus, H.E. (2002). Induction of ovarian cancer by defined multiple genetic changes in a mouse model system. Cancer Cell *1*, 53-62.

Scully, R.E., Young, R.H., and Clement, P.B. (1996). Tumors of the ovary, maldeveloped gonads, fallopian tube, and broad ligament (Washington, Armed Forces Institute of Pathology).

Sherr, C.J., and McCormick, F. (2002). The RB and p53 pathways in cancer. Cancer Cell *2*, 103-112.

Soriano, P. (1999). Generalized lacZ expression with the ROSA26 Cre reporter strain. Nat Genet *21*, 70-71.

CHAPTER 3

USE OF MULTIPHOTON IMAGING FOR STUDYING CELL MIGRATION IN THE MOUSE*

3.1 Abstract

We describe a method for studying cell motility in the living mouse using multiphoton microscopy. The procedure consists of mouse anesthesia, labeling of target cells with enhanced green fluorescent protein by infection with recombinant adenovirus, implantation of beads carrying chemoattractant, preparation of the mouse for imaging, and imaging of individual cell motions via multiphoton microscopy. Two-photon fluorescence excitation of enhanced green fluorescent protein allows visualization of cells within the dermis, whereas second harmonic generation (a non-linear scattering process) allows a simultaneous detailed definition of the dermis structure.

3.2 Introduction

The recent deciphering of human and mouse genomes, together with technical advances in mouse genetic engineering, have resulted in continuously increasing use of mice for modeling of human diseases, including cancer, neurological, cardiovascular and immune disorders. Since individual cell tracing provides important clues for understanding pathogenesis, the ability to detect single cells and monitor their behavior in the living mouse is particularly important. Multiphoton microscopy (MPM) (Denk et al., 1990; Williams et al.,

*Previously published as Flesken-Nikitin et al., (2005). Methods in Molecular Biology. 294: 335-345.

2001), a type of laser scanning microscopy, has become a preferred fluorescence imaging technique for *in vivo* studies due to its ability to image deeply into living tissue and its absence of out-of-focal plane excitation (Brown et al., 2001; Charpak et al., 2001; Christie et al., 2001; Lendvai et al., 2000; Svoboda et al., 1997; Wang et al., 2002). A type of MPM, two photon microscopy uses the simultaneous absorption of two infrared photons to excite an electronic transition equivalent to the absorption of a single higher energy (bluer) photon. In the absence of endogenously added (or transfected) fluorophores, MPM can also be used to image morphology via detection of intrinsic tissue emissions of such compounds as NADH and retinoids (Zipfel et al., 2003). However, genetically encoded green fluorescent proteins are significantly brighter (Xu et al., 1996), and, if incorporated into the system of interest, they enable imaging with lower power and less biologically damaging wavelengths (Zipfel et al., 2003). Using the same apparatus, second harmonic generation (SHG), a nonlinear scattering emission, can be collected from fibrillar collagen to obtain simultaneous images of structural features within many types of tissue. Here we describe how to use MPM for non-invasive imaging of the derma and its motile cells at subcellular resolution. The procedure consists of mouse anesthesia, labeling of target cells with enhanced green fluorescent protein (EGFP) by infection with recombinant adenovirus, implantation of beads carrying chemoattractant, preparation of the mouse for imaging, and imaging of individual cells with multiphoton microscopy.

3.3 Materials

3.3.1 Mouse Anesthesia

1. Medical oxygen tank with pressure sensor (Airgas, Radnor, PA).
2. Oxygen flow regulator (Airgas).
3. Isoflurane vaporizer (Harvard Apparatus, Holliston, MA).
4. Isoflurane (Halocarbon Laboratories, Rever Edge, NJ).
5. Tubing manifold for directing the gas to either the induction chamber or the imaging platform (Harvard Apparatus).
6. Port to building exhaust.
7. Tygon tubing (5/16-in. inner diameter).
8. Anesthesia induction chamber (Harvard Apparatus).
9. Small animal heating pad (Fine Science Tools, Foster City, CA)

3.3.2 Labeling Target Cells with EGFP

1. FVB/N mice (Taconic, Germantown, NY).
2. Recombinant adenovirus Ad5*CMVEGFP*, purified and tittered at 10^{11} – 10^{12} infectious particles/ml as described (Anderson et al., 2000); Gene Transfer Vector Core; University Iowa College of Medicine; Iowa City, IA). Albeit this virus is replication deficient, all NIH Recombinant DNA Guidelines must be closely followed.
3. Microscope Nikon SMZ 645 (Nikon, Melville, NY).
4. Fiber optic illuminator ACE (Schott-Fostec LLC, Auburn, NY).
5. Pet trimmer shaver (Wahl Clipper Corporation, Sterling, IL).
6. Isotonic saline (0.85% NaCl) sterile.
7. 70% ethanol.

8. Tissue marking dye (Triangle Biomedical Sciences, Durham, NC).

9. Hypodermic needles 21 and 30 gauge.

10. Sterile disposable syringes; 1 ml.

11. Micro dissecting forceps serrated 3.5-in. long, 0.6 mm tip (Roboz, Rockville, MD).

12. Pipetman for 1-20 µl, 10-200 µl and 100-1000 µl.

13. Sterile filter tips 1-20 µl and 10-200 µl.

3.3.3 Implanting Beads with Chemoattractant

1. Monocyte chemotactic protein 1 (MCP1), recombinant, mouse (derived from *Escherichia coli*), rmJE/MCP-1 (R&D Systems, Minneapolis, MN).

2. Heparin-acrylic beads (Sigma, St. Louis, MO).

3. PBS, Ca 2+ /Mg 2+ -free phosphate-buffered saline, sterile (Cellgro, Herndon, VA).

3.3.4. Preparation of Mouse for Imaging

1. Pet trimmer shaver (Wahl Clipper Corporation, Sterling, IL).

2. Nair lotion hair remover (Carter products, New York, NY).

3. Skin immobilizer (custom built, Fig. 3.1).

3.3.5 Multiphoton Microscopy

1. Ti:Sapphire laser (Spectra Physics, Mountain View, CA). The

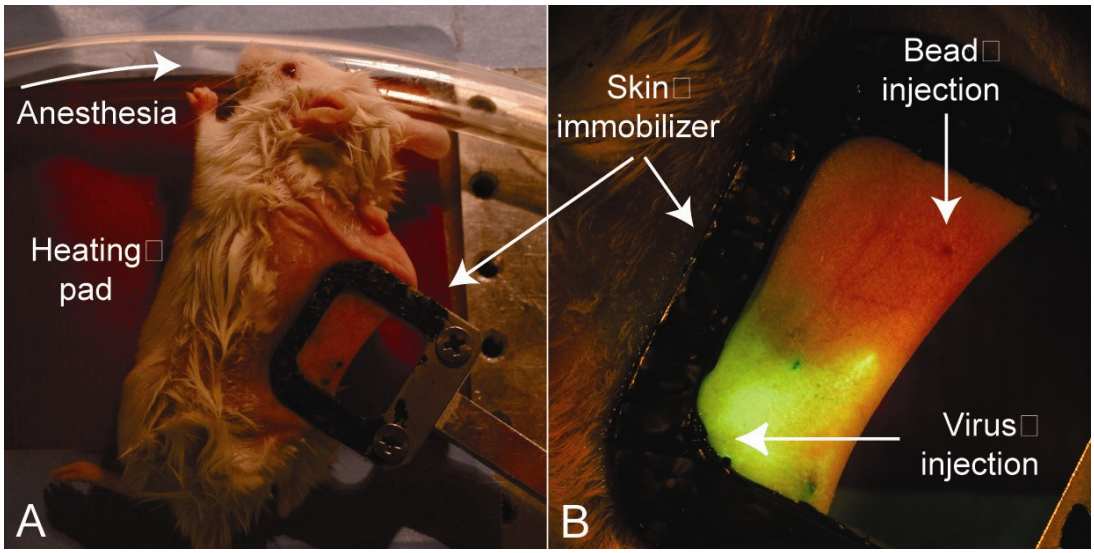

Figure 3.1 Preparing mouse for imaging. (*A*) Mouse is placed on imaging platform consisting of an anesthesia line (arrow), a heating pad (HP) and a skin immobilizer (SI). (*B*) Wide field fluorescence image of the EGFP distribution in skin. Note that leading edge of infected cells (arrow) is directed towards the location of heparin beads containing MCP1 (arrowhead). VI, place of Ad5CMVEGFP injection, SI, skin immobilizer. (*A*) and (*B*) are taken with white light and fluorescence microscopies respectively.

Ti:Sapphire laser is a Class 4 laser. A specular reflection directed into the eye could result in retina damage. A dark object in the beam path could result in a fire hazard. Appropriate cautions should be taken. The beam should be covered and stray reflections blocked from imaging personal.

2. Laser spectral analyzer (IST/Rees, Horseheads, NY).

3. Pockels cell for beam modulation (ConOptics, Danbury, CT).

4. Beam scanner with optics modified for IR transmission and associated image acquisition electronics (BioRad, Hercules, CA).

5. Microscope with laser port (Olympus, Melville, NY).

6. Non-descanned fluorescence and SHG detection unit integrated with beam scanner electronics (BioRad).

7. Appropriately selected microscope objective (Olympus).

3.4 Methods

The subsequent methods outline (1) mouse anesthesia, (2) labeling target cells with EGFP, (3) implanting beads with chemoattractant, (4) preparing mouse for imaging, and (5) multiphoton microscopy.

3.4.1 Mouse Anesthesia

Gas anesthesia (Fig. 3.2) enables the extended experimental durations that are necessary for these experiments.

1. Set the flow rate to 1 L/min.

2. Anesthetize the mouse in an induction chamber at 3.5% Isoflurane

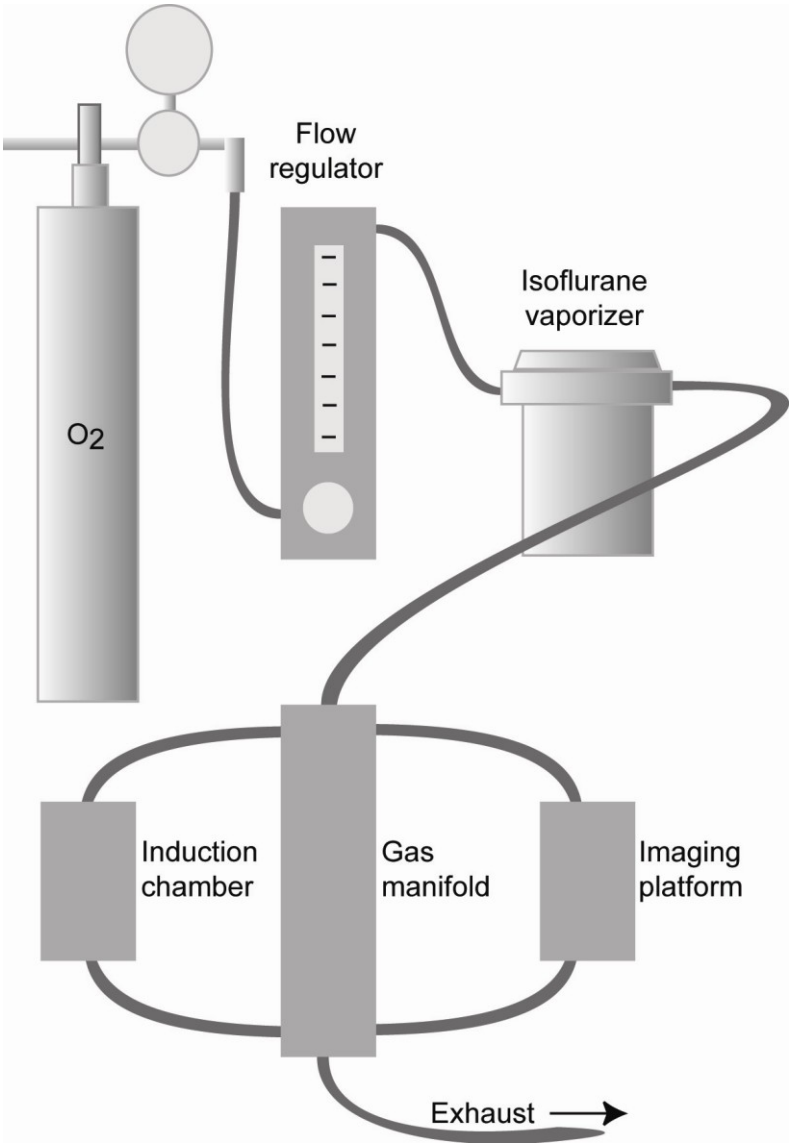

Figure 3.2 Diagram of anesthesia apparatus. Oxygen flow from a pressurized cylinder is directed through an Isoflurane vaporizer. A gas manifold directs the gas through either an induction chamber or an imaging/surgery platform. The output of the system is funneled directly to the building exhaust.

for several min. (*see* **Note 1**)

3. Transfer the mouse to the heated imaging/surgery platform and maintain them at approx 1.5% Isoflurane. Anesthesia masks small enough to fit under the microscope are not yet commercially available. Holes cut in the anesthesia tubing are an operable solution (Fig. 3.1*A*).

3.4.2 Labeling Target Cells with EGFP

Connective tissue cells are labeled by infection with recombinant adenovirus Ad5*CMVEGFP*. Ad5*CMVEGFP* is a modification of the adenovirus-5 genome, from which the *e1a* and *e1b* regions required for viral replication had been deleted and replaced with *EGFP* encoding sequence driven by the CMV immediate early regulatory sequence (Anderson et al., 2000); Gene Transfer Vector Core, University Iowa College of Medicine.

1. Freeze Ad5*CMVEGFP* in small aliquots, and store at -80ºC.

2. Thaw frozen Ad5*CMVEGFP* aliquots, dilute in isotonic saline to 5 x 10^8 pfu/ml and keep on ice until needed (see **Note 2**).

3. Anesthetize two-month old FVB/N mice with Isoflurane (see **Subheading 3.4.1)** place them on the heating pad, and shave on the left and right side of the upper and lower back.

4. Transfer the mice to a stereomicroscope with fiber optic illumination and position for the virus injection.

5. Inject 50 µl of virus with a 30-gauge hypodermic intradermally in both lower dorsal quadrants.

6. After injection, mark the areas of the visible virus bubble with four blue tissue dye dots (see **Note 2.**).

3.4.3 Implanting Beads with Chemoattractant

MCP1 is a chemoattractant known to induce positive chemotaxis of mononuclear phagocytic cells (Gu et al., 1999; Luini et al., 1994; Rollins et al., 1988). It is used to direct positive motility of macrophages infected with Ad5*CMVEGFP*.

1. Reconstitute a lyophilized sample of MCP1 in sterile PBS containing 0.1% bovine serum albumin to a concentration 100 µg/ml (*see* **Note 3**).
2. Suspend heparin beads in storage solution evenly by flipping the tube and add 90 µl of suspension to 1 *µ*g/10 µl MCP1 in 1.7-ml sterile micro centrifuge tubes.
3. After incubation for 1 h at room temperature, centrifuge the beads for 5 minutes at 600*g*, take out the supernatant, add 1 ml sterile PBS, suspend gently, and centrifuge as before.
4. After the washing, suspend the beads in sterile PBS to a final concentration of 10 *µ*g/ml MCP1 and store at room temperature until injection.
5. Incubate and wash control beads in PBS as described in **step 3**.
6. Immediately after the virus administration, inject 100 µl of MCP1 chemoattractant releasing beads intradermally with a 21-gauge hypodermic needle one centimeter above the area injected with adenovirus.

7. Control beads are injected in the opposite dorsal quadrant above the area injected with adenovirus.

3.4.4 Preparing Mouse for Imaging

1. Remove hair in region of interest with a small animal trimmer.
2. Apply Nair® lotion hair remover for 4 min (*see* **Note 4**)
3. Wash area with warm water and finish with 70% ethanol to remove optical interference caused by mineral oil component of the Nair®.
4. General motion of the skin as the result of breathing would make impossible the task of following individual cells with micron resolution. Thus, during imaging, the skin must be stretched into a skin immobilizer (Fig. 3.1*A*) to isolate the imaging area from the general body motion.
5. At this point the generalized distribution of fluorescent cells can be imaged using a low NA objective and fluorescent illumination (Fig. 3.1*B*).

3.4.5 Multiphoton Microscopy

Several commercial multiphoton microscopes now exist (such as the Bio-rad Radiance2100 MP, the Zeiss 510 NLO and the Leica TCS MP) and should be capable of imaging into the dermis. Our setup consists of a Ti:Sapphire laser (Milenia/Tsunami combination, Spectra Physics), Bio-Rad 600 laser scanner and modified Olympus AX-70 upright microscope (Fig. 3.3).

The excitation light is focused into the mouse dermis with a large-barrel Olympus 20X/0.95NA water objective, which provides a large field-of-view, a

Figure 3.3 Multiphoton microscope. Ti:Sapphire laser (Milenia/Tsunami combination, Spectra Physics) is directed into a Bio-Rad 600 beam scanner interfaced with a modified Olympus AX-70 upright microscope. A Conoptics 350-80 BKLA Pockel's Cell provides beam intensity modulation and blanking during scanner flyback when data is not being collected. A frequency spread in the output beam is necessary for supporting mode-locked (pulsed) operation and is monitored by a laser spectral analyzer (IST/Rees E201). The excitation light is focused into the mouse dermis with a large-barrel Olympus 20X/0.95NA water objective, which provides a large field-of-view, a relatively high NA, good IR transmission, and a few mm of working distance, which is usually necessary for maneuvering in live animals. The non-linear emissions are not directed back through the scanning mirrors like they are in confocal microscopy because background rejection is unnecessary. The emission beam is collected in epi mode, spectrally separated from the excitation beam and immediately detected within the microscope housing (termed "non-descanned" detection).

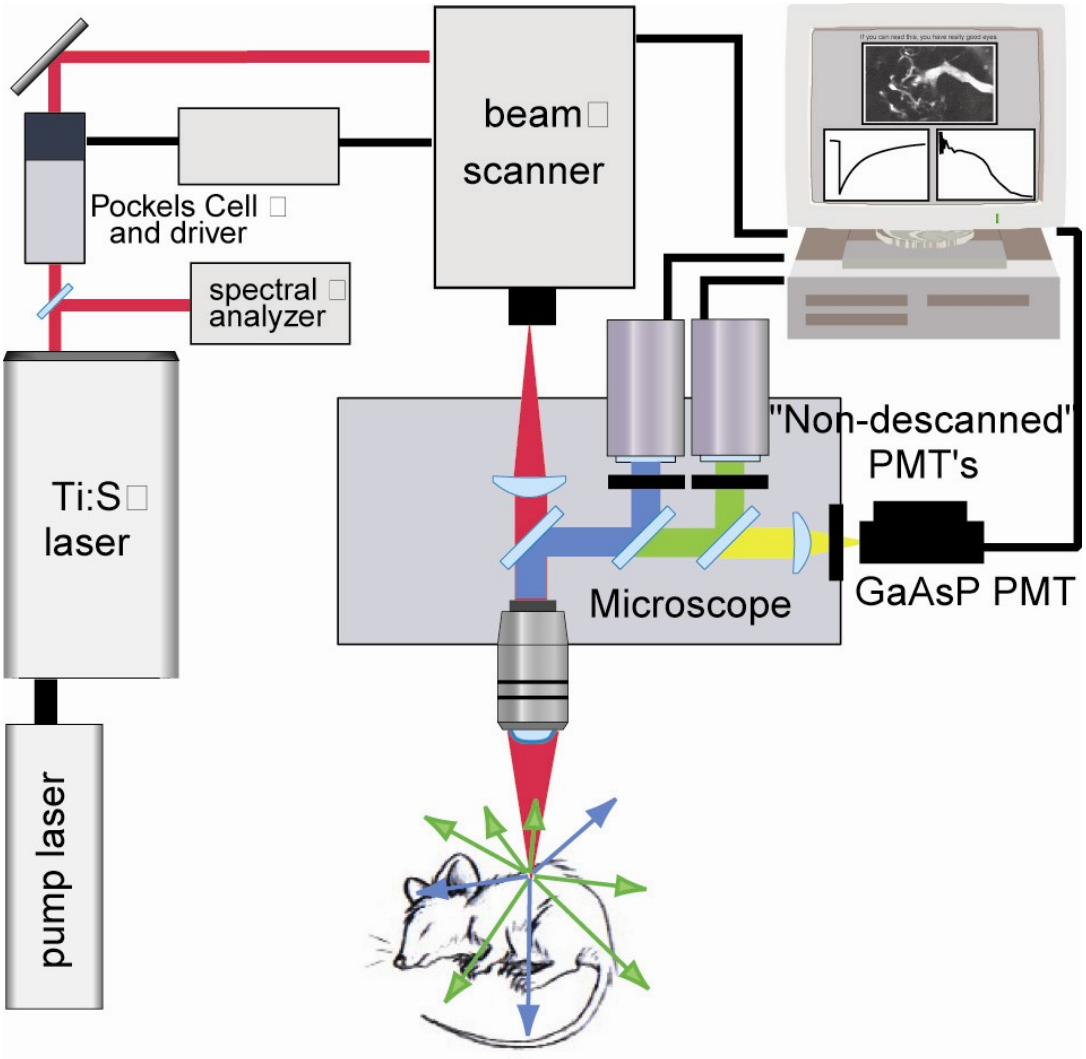
beam
scanner
Pockels Cell
and driver
spectral
analyzer
Ti:S
laser
pump laser
"Non-descanned"
PMT's
GaAsP PMT
Microscope

relatively high NA, good IR transmission, and a few mm of working distance.

The multiphoton excitation wavelength peak (λex) is tuned to 900 nm because EGFP absorbs well at this wavelength (Xu et al., 1996), whereas water and intrinsic cellular absorbers do not (Zipfel et al., 2003). The EGFP emission spectral profile is independent of the excitation wavelength; it peaks at 515 nm with a spectral width of approx 40 nm. The collagen SHG emission wavelength, however, will tune with the excitation wavelength; it peaks at λex/2 (and possesses a spectral width equal to that) of the exciting beam reduced by √2 (Zipfel et al., 2003). Non-linear emissions are collected in epi mode and immediately separated from the excitation beam directly after the objective with a 670DCXXRU long-pass dichroic filter. Emission filters are chosen for a clean blue, green (450 and 515 nm) separation (BGG22 and 580/150 filters with a separating 500DCXR dichroic filter, Chroma Technology) and a 10^7 rejection ratio of the exciting to emitting wavelengths. The resulting two emission beams are collected by Hamamatsu HC125-02 bialkali photomultiplier tube assemblies (see **Note 5**)

1. Tune laser wavelength to 900 nm.

2. Peak laser power.

3. Tune laser prisms for a stable, Gaussian-like frequency spread.

4. Image test slide to ensure system is operating properly.

5. Image mouse skin. One of the benefits of multiphoton microscopy is its ability to collect clean optical sections from live tissue. The thickness (full-width at half maximum) of each section is given by (Williams et al., 1994):

$$\Delta = \frac{0.31\lambda_{ex}}{n \sin^2(\theta/2)}$$

where $n \sin \theta$ is the NA of microscope objective and n is the refractive index of the immersion fluid. For the 20X/0.95NA water objective used in our experiments, this thickness is 1.4 μm. To follow cells, one can either acquire a time series at one plane or a time series of stacks at multiple planes. An example of time series at 8 min. intervals shows cell movement with an average speed of 1.4 μm/min (Fig. 3.4).

3.5 Notes

1. The amount of sufficient Isoflurane varies from mouse to mouse and especially with age. Breathing rate is the easiest way to monitor the health of the mouse. Higher Isoflurane levels correspond to slower breathing rates. We try to maintain the mouse at an "ideal" breathing rate of about 0.3 Hz, or 1-2 breaths per image. A "typical" 8 h-day of surgery and imaging will consume about one "medical-sized" oxygen tank and about one 200-ml bottle of Isoflurane.

Heating is critical to long-term maintenance of the mouse under anesthesia. We use a Fine Science Tools heating pad calibrated to a surface temperature (without the mouse) of 30-35^{o}C. While under anesthesia, the mouse is unable to regulate its own temperature well. Too much or too little heat can result in the death of the patient.

2. All aliquots are only thawed once and rest is discarded after the use. The use of sterile filter tips to aliquot and dilute the virus is recommended. All plasticware and instruments which had virus contact are soaked in 70% ethanol for decontamination. To perform the intradermal injection, a skin fold is hold up with a pair of micro dissection forceps. After penetrating the skin with a

Figure 3.4 Multiphoton images of cell migration. Detection of fluorescence of EGFP-expressing cells (EGFP, *A*-*D*) and SHG-producing collagen (SHG, *E*-*H*) in the dermis. (*I*-*L)* Photon emissions from both channels added together in order to show cell motion with respect to the stationary dermal structure. Images are acquired each 30 s, and displayed at 8-min intervals. Note that EGFP-labeled cell (arrows) moves in relation to stationary collagen fibers (arrowheads). Calibration bar, 20 μm.

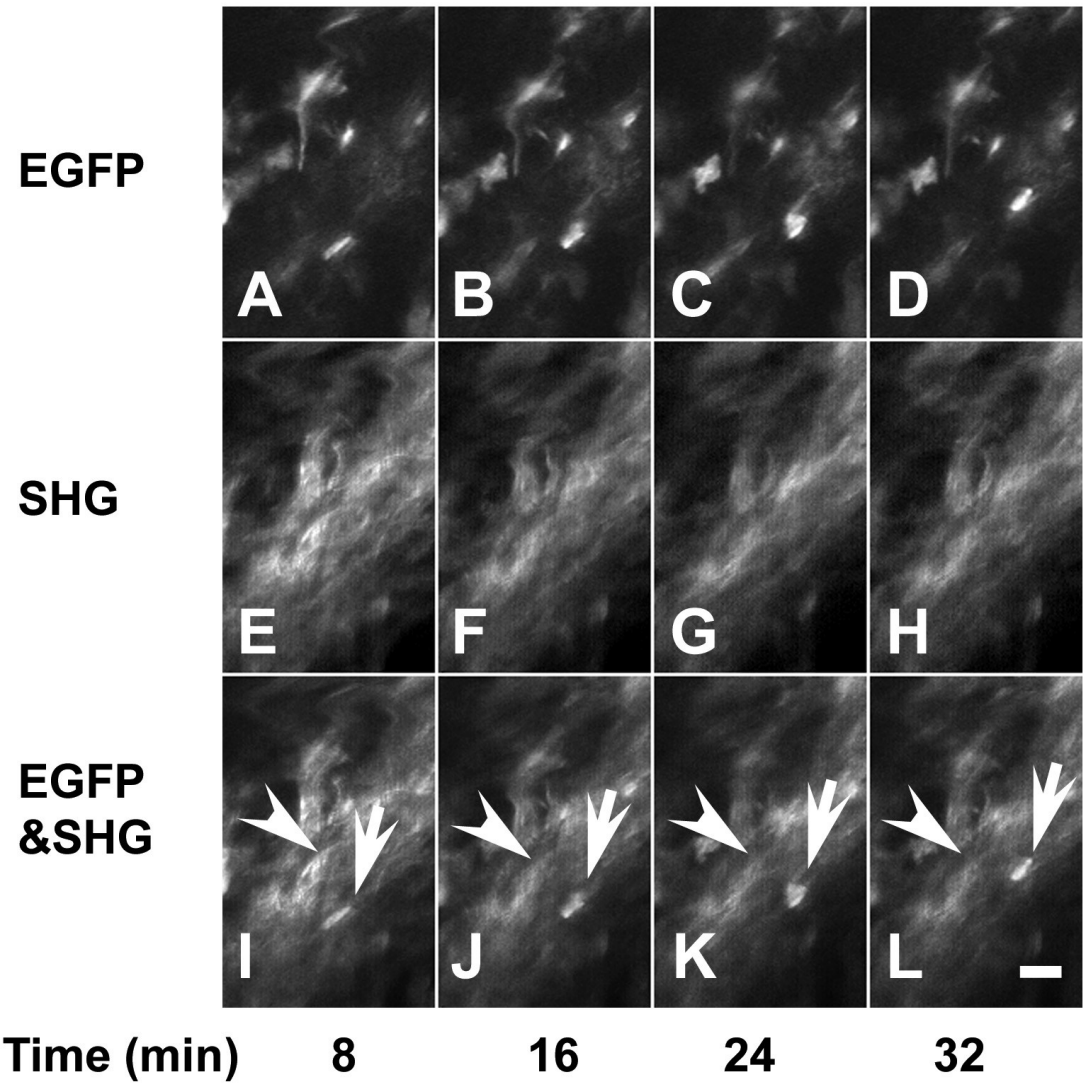
EGFP
SHG
EGFP
&SHG
A
B
C
D
E
F
G
H
I
J
K
L
Time (min)
8
16
24
32

30-gauge needle, the forceps are loosened and the fluid is allowed evenly to disperse. The needle is slowly withdrawn so that no liquid is able to leak out.

3. Upon reconstitution MCP1 can stored at -20º C no more than three months. See also **Notes 2** regarding intradermal injection.

4. For repeated imaging, the Nair® hair removal solution must be totally removed because it is quite caustic (pH > 11), and thus expected to be toxic to the mice when ingested during grooming.

5. Of utmost importance in imaging live specimens are the efficiency and placement of the emission detectors. Because non-linear emissions are only excited in the focal plane, they need not be descanned and focused through a confocal pinhole. Removing extraneous optics from the detection pathway and locating detectors close to the collecting objective increases the detector efficiency and enables the additional collection of photons deflected by the highly scattering skin on the way out.

Imaging a constant test slide, consisting of a fixed biological specimen or a fluorescent polymer or beads, before every microscopy session is an extremely valuable practice. Though the multiphoton microscope is a relatively complicated instrument, it should return consistent imaging results from day to day. When imaging highly variable specimens such as live mice, one should be sure that the instrument itself is not providing any of the experimental variability.

One irritating problem encountered in these experiments is that the immersion saline often wicks around the mouse and away from the objective, resulting in the loss of the image. A thin layer of bathroom caulk over the skin immobilizer eliminates this problem. Another difficulty encountered in the acquisition of time series images is focal plane drift over time. This problem is

best solved by identifying and alleviating any slight temperature variations around the microscope or specimen. Because skin pigmentation significantly impairs photon penetration, all experiments should be performed on white albino mice, such as FVB/N.

REFERENCES

Anderson, R.D., Haskell, R.E., Xia, H., Roessler, B.J., and Davidson, B.L. (2000). A simple method for the rapid generation of recombinant adenovirus vectors. Gene Ther *7*, 1034-1038.

Brown, E.B., Campbell, R.B., Tsuzuki, Y., Xu, L., Carmeliet, P., Fukumura, D., and Jain, R.K. (2001). In vivo measurement of gene expression, angiogenesis and physiological function in tumors using multiphoton laser scanning microscopy. Nat Med *7*, 864-868.

Charpak, S., Mertz, J., Beaurepaire, E., Moreaux, L., and Delaney, K. (2001). Odor-evoked calcium signals in dendrites of rat mitral cells. Proc Natl Acad Sci U S A *98*, 1230-1234.

Christie, R.H., Bacskai, B.J., Zipfel, W.R., Williams, R.M., Kajdasz, S.T., Webb, W.W., and Hyman, B.T. (2001). Growth Arrest of Individual Senile Plaques in a Model of Alzheimer's Disease Observed by In Vivo Multiphoton Microscopy. J Neurosci *21*, 858-864.

Denk, W., Strickler, J.H., and Webb, W.W. (1990). Two-photon laser scanning fluorescence microscopy. Science *248*, 73-76.

Gu, L., Tseng, S.C., and Rollins, B.J. (1999). Monocyte chemoattractant protein-1. Chem Immunol *72*, 7-29.

Lendvai, B., Stern, E.A., Chen, B., and Svoboda, K. (2000). Experience-dependent plasticity of dendritic spines in the developing rat barrel cortex in vivo. Nature *404*, 876-881.

Luini, W., Sozzani, S., Van Damme, J., and Mantovani, A. (1994). Species-specificity of monocyte chemotactic protein-1 and -3. Cytokine *6*, 28-31.

Rollins, B.J., Morrison, E.D., and Stiles, C.D. (1988). Cloning and expression of JE, a gene inducible by platelet-derived growth factor and whose product has cytokine-like properties. Proc Natl Acad Sci U S A *85*, 3738-3742.

Svoboda, K., Denk, W., Kleinfeld, D., and Tank, D.W. (1997). In vivo dendritic calcium dynamics in neocortical pyramidal neurons. Nature *385*, 161-165.

Wang, W., Wyckoff, J.B., Frohlich, V.C., Oleynikov, Y., Huttelmaier, S., Zavadil, J., Cermak, L., Bottinger, E.P., Singer, R.H., White, J.G*., et al.* (2002). Single cell behavior in metastatic primary mammary tumors correlated with

gene expression patterns revealed by molecular profiling. Cancer Res *62*, 6278-6288.

Williams, R.M., Piston, D.W., Webb, W.W. (1994). Two-photon molecular excitation provides intrinsic 3-dimensional resolution for laser-based microscopy and microphotochemistry. FASEB Journal *8*, 804-813.

Williams, R.M., Zipfel, W.R., and Webb, W.W. (2001). Multiphoton microscopy in biological research. Curr Opin Chem Biol *5*, 603-608.

Xu, C., Zipfel, W., Shear, J.B., Williams, R.M., and Webb, W.W. (1996). Multiphoton fluorescence excitation: New spectral windows for biological nonlinear microscopy. Proc Natl Acad Sci U S A *93*, 10763-10768.

Zipfel, W.R., Williams, R.M., Christie, R., Nikitin, A.Y., Hyman, B.T., and Webb, W.W. (2003). Live tissue intrinsic emission microscopy using multiphoton-excited native fluorescence and second harmonic generation. Proc Natl Acad Sci U S A *100*, 7075-7080.

CHAPTER 4

STRATEGIES FOR HIGH-RESOLUTION IMAGING OF EPITHELIAL OVARIAN CANCER BY LAPAROSCOPIC NONLINEAR MICROSCOPY*

4.1 Abstract

Ovarian cancer remains the most lethal of the gynecological cancers due to late detection of this disease. Here, by using human specimens and 3 mouse models of ovarian cancer we test the feasibility of nonlinear imaging approaches, such as multiphoton microscopy (MPM) and second harmonic generation (SHG) microscopy to serve as valuable complementary tools for ovarian cancer diagnosis. We demonstrate that MPM of intrinsic tissue fluorescence allows visualization of unfixed, unsectioned, and unstained tissues at a resolution comparable to that of routinely processed histological sections. In addition to permitting discrimination between normal and neoplastic tissues according to pathological criteria, such as alterations in size and shape of cellular compartments and tissue architecture, the method facilitates morphometric assessment of specimens and detection of very early cellular changes in the ovarian surface epithelium. A red-shift in cellular intrinsic fluorescence and collagen structural alterations have been identified as additional cancer-associated changes that are indiscernible by conventional pathologic techniques. Importantly, the feasibility of in vivo laparoscopic MPM/SHG is demonstrated by using a "stick" objective lens that allows direct access to and stabilization of imaged tissues. Intravital detection of neoplastic lesions has been further facilitated by low magnification identification of an

*Previously published as #Williams, #Flesken-Nikitin et al., #Equal contributions, (2010). Translational Oncology. 3 (3): 181-194.

indicator for cathepsin activity followed by MPM laparoscopic imaging. Taken together, these results demonstrate that MPM may be translatable to clinical settings as an endoscopic approach suitable for high resolution optical biopsies as well as a pathology tool for rapid initial assessment of ovarian cancer samples.

4.2 Introduction

Ovarian cancer is the most deadly gynecological cancer. It is estimated to be the fifth leading cancer in cancer related deaths in women in the United States. It will be responsible for about 21,550 (3% of total) of new cancer cases and 14,600 (5% of total) of cancer related deaths in 2009 (Jemal et al., 2009). When the disease is diagnosed at its early stages, the survival rate can be over 90%. However because the early stages are relatively asymptomatic, the vast majority of cases of ovarian carcinomas are not identified until late, rarely curable stages when almost 70% of tumors have already spread beyond the ovary (Bast et al., 2009). Cytoreductive surgery of metastatic ovarian cancer may extend patient's survival but its success greatly depends on effective detection and elimination of the bulk of tumor (Olson et al., 2001; Tingulstad et al., 2003; Zivanovic et al., 2009).

Development of new imaging diagnostic approaches is expected to significantly advance detection of ovarian cancer. Several recent studies have reported on improved detection of metastatic ovarian cancer by multi-targeted *in vivo* optical imaging (Kosaka et al., 2009) and fluorescence protease imaging in immunocompromised mice (Sheth et al., 2009). Unfortunately, resolution of these approaches has precluded evaluation of neoplasms at the

cellular level. Furthermore, feasibility of intravital detection of earlier stages of ovarian cancer has not been demonstrated.

A possible approach to address both issues is nonlinear imaging by multiphoton microscopy (MPM) and second harmonic generation (SHG). MPM is a type of incoherent nonlinear laser scanning microscopy that uses the simultaneous absorption of 2 near-infrared photons to excite an electronic transition equivalent to the absorption of a single higher energy, "bluer" photon (Denk et al., 1990) (Zipfel et al., 2003b). Use of near-infrared light instead of UV or higher energetic bands, which are required to excite most intrinsic emitters in biological tissues (Ramanujam et al., 2000; Richards-Kortum and Sevick-Muraca, 1996; Zipfel et al., 2003a), mitigates UV associated photodamage, optical aberrations and excitation light attenuation. These advantages, together with absence of out-of-focal plane excitation, allow MPM to penetrate about 2-fold deeper into optically scattering tissues with much cleaner subcellularly-resolved images compared to confocal microscopy (Helmchen and Denk, 2005; Zipfel et al., 2003b). MPM is frequently used simultaneously with SHG, an imaging strategy based on linear coherent scattering of the illumination light by certain tissue components, such as collagen. SHG always emits at exactly one half of the illumination wavelength and is easily separated from the broad generally blue fluorescence emission spectra characteristic of unstained tissue, enabling simultaneous imaging of collagen at the single fibril level (Zipfel et al., 2003a).

Owing to MPM's features, such as depth of penetration, reduced phototoxicity and intrinsic optical sectioning, and SHG's high-resolution assessment of fibrillar collagen structure not visible in standard hematoxylin and eosin stained (H&E)-stained sections these nonlinear imaging methods

have been recognized as a promising diagnostic approaches of cancer (Zipfel et al., 2003a). Optical biomarkers of ovarian cancer were specifically evaluated with nonlinear microscopy (Kirkpatrick et al., 2007). However, it remains unclear to what extent MPM/SHG imaging will allow for robust identification of routine diagnostic pathological features. Furthermore, applicability of MPM/SHG to characterization of various stages of ovarian carcinogenesis in autochthonous mouse models of cancer has not been tested. Most importantly, it is unknown whether there is adequate sensitivity to identify features *in vivo*, making the feasibility of practical high-resolution endoscopic MPM/SHG uncertain.

In this paper we assess of applicability of the MPM/SHG approach to pathological evaluation of epithelial ovarian carcinoma (EOC) in human samples and three syngeneic mouse models generated by us. We demonstrate that MPM of intrinsic tissue fluorescence in ovarian tissues allows reproducible identification of neoplastic features such as cellular atypia and architectural alterations at different stages of carcinogenesis. This information is further complemented by MPM/SHG-specific features such as cancer-associated alterations in intrinsic fluorescence and collagen structure. Finally, we demonstrate, in a proof-of-principle experiment, that high-resolution MPM/SHG optical biopsy can be accomplished by *in vivo* laparoscopy with a miniature stick objective lens. This approach can be further combined with pre-screening for neoplastic changes by a cathepsin-activated NIR fluorescent probe.

4.3 Materials and Methods

Mouse Models of Ovarian Cancer. Development of EOC in mice expressing Simian virus (SV) 40 T antigen under control of the Mullerian inhibitory substance receptor 2 promoter (Tg*MISIIR-TAg)* was described previously (Connolly et al., 2003). Induction of EOC by a single trans-infundibular intrabursal administration of recombinant adenovirus expressing Cre (AdCre) in mice carrying floxed copies of *p53* and *Rb* genes was also described elsewhere (Flesken-Nikitin et al., 2003). To prepare a syngeneic mouse model of disseminated peritoneal EOC, *p53*-, and *Rb*-deficient FVB/N ovarian surface epithelium (OSE), cell line OSN1 (Corney et al., 2007) was transduced with LNCX2 retrovirus containing mouse c-Myc (kind gift of Dr. Andrew Yen). Briefly, retrovirus was produced by EcoPack2-293 (protocol PT3132-1; Clontech Laboratories), and exponentially growing cells were infected with a medium containing 50% retroviral supernatant and 8 μg/ml polybrene (S2667; Sigma) for 24 hours. Medium was changed for complete growth medium and 500 μg/ml G418 (gentamicin sulfate) was added 48 hours afterwards. The resulting cell line OSN3 was intraperitoneally inoculated into 5- to 6-week-old FVB/N inbred mice (Taconic) at a concentration of $1x\ 10^7$ cells/0.5 ml of PBS. Mice injected with 0.5 ml PBS only were used for control. At scheduled time points or upon signs of illness the animals were either anesthetized or euthanized and their tissues were processed for *in vivo* or *ex vivo* imaging, respectively, followed by histological processing and pathological assessment as described later. As a control for morphological alterations during imaging, a part of some specimens was directly processed for histological analysis. In addition, a parallel identically treated group of animals was euthanized at the same time points and subjected to standard necropsy and processing procedures. All the mice were maintained identically following

recommendations of the Institutional Laboratory Animal Use and Care Committee.

Cell Culture. Preparations of primary normal and p53/Rb mutant OSE cells were performed as previously described (Corney et al., 2007; Flesken-Nikitin et al., 2003; Flesken-Nikitin et al., 2007). Briefly, OSE cells were isolated by collagenase-dispase digestions from ovaries of mice carrying floxed copies of *p53* and *Rb* genes (Flesken-Nikitin et al., 2003). Cells were expanded within three passages, exposed to AdCre and used after three passages. Complete Cre-*LoxP*-mediated gene excision was verified by polymerase chain reaction (Flesken-Nikitin et al., 2003). For control experiments OSE cells were exposed to adenovirus-expressing β-galactosidase (AdLacZ).

Human Materials. Using anonymous fresh surgical material tagged for disposal, specimens of morphologically normal ovaries and serous EOC were collected at the Weill Medical College of Cornell University. One- to three-millimeter-thick slices of the material were prepared, immediately placed into either Ringer's solution or serum- and phenol red-free, HEPES-buffered RPMI and kept on ice. The material was transported to imaging facilities and used for collection of images by multiphoton microscope within 6 to 20 hours after resection. All procedures were approved by the institutional review board.

Nonlinear (MPM and SHG) Imaging of Intrinsic Fluorescence. Multiphoton imaging was accomplished as previously described (Kloppenburg et al., 2000; Williams and Webb, 2000; Zipfel et al., 2003a). Briefly, a 780 nm, uncompensated beam from a mode-locked Ti:sapphire laser (Tsunami

pumped with a Millennia Xs; Spectra Physics, Mountain View, CA) was directed through a Pockels Cell (350-80LA; Conoptics, Danbury, CT) with laboratory-built electronics for beam modulation and blanking during scan fly-back. The beam was then directed into a modified BioRad scanner (MRC-600, Hercules, CA) interfaced with a modified (fixed stage) Olympus AX-70 upright microscope (Center Valley, PA). Specimens were imaged either with a standard objective (20x/0.95W XLUMPlanFI; Olympus) or with an endoscopic stick objective (27x/0.7W IV-OB35F22W20; Olympus). Tissue emissions were separated from the excitation beam using a 670DCXRU long-pass dichroic filter (Chroma Technology, Inc, Rockingham, VT) placed directly at the back aperture of the microscope objective. The emissions were subsequently separated into two channels with a 440DCXRU long-pass dichroic and HQ390/702-2P and BGG22 emission filters (Chroma Technology, Inc). The first channel (355-425 nm, pseudocolored blue in the figures) is designed for collecting second harmonic from fibrillar collagen and the second channel (~450-550 nm, pseudo-colored yellow) collects emissions from tissue intrinsic fluorescence such as cellular NAD(P)H and retinoid compounds. Both signals were detected using blue bialkali-photocathode PMT assemblies (HC125-02; Hamamatsu, Bridgewater, NJ). For determining intrinsic fluorescence color -- long-wavelength (LW) *versus* short-wavelength (SW) emission--signals were instead separated using a 500DCXRU dichroic splitter to BGG22 (SW) and 580DF150MP (LW) emission filters (Chroma Technology, Inc). All imaging on freshly excised mouse samples occurred within 15 min after removal. Analysis of collagen fibril alignment in the peritoneum was analyzed by calculating two-dimensional fast Fourier tranforms (FFTs) of high-resolution SHG image stacks (164 x 110 x 10 μm^3). The resulting Fourier images were fit to two-

dimensional Gaussian surfaces, and their asymmetry was defined as the ration of major-minor axes. Image stacks were collected from the peritoneum around tumors of two EOC mice (*n* = 4 stacks) and in two control mice (*n* = 4 stacks).

Quantitative Assessment of Intrinsic Fluorescence: Intensity, Color, and Anisotropy. For quantification of intensity, color, and steady-state emission anisotropy of the intrinsic fluorescence in cell cultures, cell regions were automatically defined by pixel intensities greater than the measured image background plus the image SD. In tissue explants, cells of interest were masked manually using the paint tool and an additional channel in Adobe Photoshop. All pixel tabulation routines were custom-written using the IDL data analysis environment (ITT Visual Information Solutions, White Plains, NY).

For anisotropy measurements the excitation polarization was adjusted for linear polarization (~50/1 ellipticity) directly after the objective by means of a Berek compensator (5540; New Focus, San Jose, Ca) placed before the scanning box. The emitted fluorescence was separated into parallel and perpendicular components after the collecting objective with a broadband polarizing beam splitter (10FC16PB.3; Newport, Irvine, CA) and two polarizers (5511; New Focus) placed immediately before the emission filters (BGG22; Chroma Technology, Inc.). The fluorescence anisotropy A was defined as the normalized difference between the emission intensities parallel ($I_{\parallel}$) and perpendicular ($I_{\perp}$) to the exciting polarization:

$$A = \frac{I_{\parallel} - I_{\perp}}{I_{\parallel} + 2I_{\perp}}$$

Calibration of the relative detected efficiencies ($I'_{\parallel}$ and $I'_{\perp}$) was accomplished by rotating the excitation polarization so that the parallel channel becomes the perpendicular channel and *vice versa*. For an isotropic sample, the measured anisotropy is the same with both excitation polarizations so that:

$$A = \frac{I'_{\parallel} - gI'_{\perp}}{I'_{\parallel} + 2I'_{\perp}} = A_{rot} = \frac{I'_{\parallel,rot} - (1/g)I'_{\perp,rot}}{I'_{\parallel,rot} + 2I'_{\perp,rot}}$$

This relationship was used to determine *g,* the relative scaling factor between the two channels accounting for differential emission path efficiencies, and PMT gain variations. Average anisotropy values for the masked regions were calculated by an algorithm written within IDL.

Quantification of red shift in cellular intrinsic fluorescence of tissues was accomplished by masking normal OSE or tumor regions in images from the disseminated metastasis mouse model. Average pixel values from the LW *versu*s SW channels from those regions were tabulated using a custom-written algorithm within IDL.

In Vivo Imaging. The mouse to be imaged was shaved and anesthetized in an induction chamber with 3.5% isoflurane gas. After 1 to 2 minutes, it was transferred to the imaging stage where gas was delivered through a 0.5-inch-diameter tube with a small opening to insert the mouse snout, and warming was accomplished with a heating pad with feedback from a rectally inserted probe monitoring core temperature (FHC model 40-90-8C A720D). Gas percentage was adjusted to 1% to 2%, maintaining a ~60/min breathing rate as described previously (Flesken-Nikitin et al., 2004). For imaging with a standard water immersion objective (Olympus XLUNPlanFl 20x/0.95 W), a Parafilm bed was suspended over the mouse as a platform to isolate the ovary from mouse breathing motions. The ovary was threaded through an incision in

the abdomen and a precut opening in the suspended Parafilm bed. Immersion saline necessary for optimal imaging was kept around the ovary by the Parafilm bed. Imaging directly into the mouse abdomen was accomplished using the 3.2 mm diameter Olympus stick objective lens (IV-OB35F22W20 27x/0.7 W). In addition to the microprobe optic, two other developments were required for obtaining high-quality cellularly resolved tumor images within the abdominal cavity: 1) a mechanism for flushing blood and other optically unfavorable, tissue-derived substances away from the imaging region, and 2) a mechanism for stabilizing the tissues from mouse movements. We initially designed a sleeve through which the microprobe slid for focusing; the sleeve was connected to perfusion piping and provided stabilization to the tissue. This design turned out to be too bulky and drew the tissue into it when the probe was moved away from the specimen. A simpler design in which a small tube (2 mm in diameter) was mounted on a separate micromanipulator proved better for flushing tissues in the field of view. The hose also acted to stabilize the tissue, reducing tissue motion due to mouse breathing and objective focusing.

Imaging of Cathepsin Activity. For administering ProSense 680 (VisEn Medical, Inc., Woburn, MA), mice were anesthetized with Avertin (2.5% v/v in 0.85% NaCl; 0.020 ml/g body weight) and the ProSense 680 was injected into a tail vein at 2 nmol/150 µl in PBS. Mouse tissues were imaged *ex vivo* 24 hrs after ProSense 680 administration. Overall fluorescence images were collected using the RFP2 filter on an Olympus SZX12 fluorescence stereomicroscope. Multiphoton imaging of ProSense 680 was accomplished as previously described for intrinsic fluorescence, except that the fluorescence

emission was instead split by a 560DCXRU into blue- (BGG22; Chroma Technology, Inc.) and red- (650DF100MP, Chroma Technology, Inc.) pseudocolored channels. The blue emission was detected with a bialkali PMT (HC125-02; Hamamatsu) and the NIR ProSense 680 emission (pseudocolored red in the figures) was detected using a red-sensitive GaAsP photocathode PMT (H7422P-40; Hamamatsu) with custom-designed amplifier circuitry. ProSense 680 imaging required significantly (typically fivefold) less excitation power than that for imaging intrinsic fluorescence.

Pathological Assessment. Human and mouse specimens were labeled by ink for orientation, placed into PBS-buffered 4% paraformaldehyde, fixed overnight, and processed for paraffin embedding. Before sectioning, samples were carefully oriented in order to ensure direct comparison of MPM/SHG and routine microscopic images. Prepared sections were stained with H&E and evaluated under a light microscope. All ovarian lesions were identified according to the Classification Guidelines endorsed by the Mouse Models of Human Cancer Consortium (MMHCC Davis et al., 2001; Nikitin et al., 2004) and World Health Organization's classification of human ovarian cancer (Scully and Sobin, 1999). Histological images were collected by SPOT-RT or Insight cameras (Diagnostic Instruments, Sterling Heights, MI) and compared to MPM/SHG images of the same or parallel specimens.

*Morphometric Analysis***.** Digital MPM images of z series with 5-μm steps were imported into SPOT software (v. 4.6; Diagnostic Instruments). Comparable areas of optical sections across OSE covering the corpus luteum were identified and nuclear and cytoplasmic contours were manually marked by

individuals that were blinded to the experimental parameters. Image overlays were recorded and parameters calculated using the *measurements* function.

Statistical Analysis. For statistical analysis, two-sided unpaired Student's *t* tests were performed using InStat 3.05 and Prism 4.03 software (GraphPad, Inc., La Jolla, CA).

4.4 Results

4.4.1 High-Resolution Multiphoton Microscopy of Intrinsic Fluorescence in Mouse and Human Ovarian Cancer. Previously we demonstrated that histological architecture of the normal ovary and its cellular composition can be accurately identified by MPM of intrinsic fluorescence of freshly excised samples (Zipfel et al., 2003a). Therefore, to determine the value of MPM for pathological assessments of neoplastic lesions, we compared images taken with MPM/SHG without added fluorescent labels with those from sections after routine histological processing and H&E staining of the normal OSE and its neoplasms (both mouse and human). As visualized using H&E staining, normal OSE presented as a single layer with squamous morphology (Fig. 4.1*A*). In contrast, ovarian carcinomas of Tg*MISIIR-TAg* mice (n = 12) contained densely packed polygonal atypical epithelial cells (Fig. 4.1*D*). In agreement with our previously reported observations (Connolly et al., 2003), the neoplastic cells were arranged in solid sheets and separated by a limited stroma. MPM/SHG imaging of fresh unstained tissues provided the same level of resolution in terms of the overall histological and cellular features of the normal (Fig. 4.1, *B* and *C*) and neoplastic tissues (Fig. 4.1, *E* and *F*). Similar to

Figure 4.1 Evaluation of MPM (yellow) and SHG (blue and grayscale) potential for examination of (EOC). Normal mouse ovary (*A*-*C*), ovarian carcinomas of Tg*MISIIR-TAg* (*D*-*F*) and disseminated peritoneal EOC (*G*-*M*) mouse models were visualized by H&E staining (*A, D* and *G*). MPM intrinsic emission (*B*, *E* and *H*) and SHG imaging (*B, C, E, F, H, I*-*M*). (*A*-*C*) The ovarian surface epithelium (OSE, arrow), part of the corpus luteum (CL) and the ovarian bursa (OB) are all clearly resolvable by MPM and resemble those in conventional histological image. In addition, SHG demonstrates collagen in the ovarian bursa and the basement membrane (BM) underneath of OSE. (*D*-*F*) Monomorphous polygonal neoplastic cells (arrow) are detectable by H&E and MPM. Note that SHG demonstrates presence of collagen with most collagen fibers near tumor periphery being located perpendicular towards its surface (arrowhead), a feature not evident in conventionally prepared tissue. (*G*-*H*) A group of neoplastic cells (arrow) invading the parietal peritoneum. Low -(*J* and *L*) and high- (*K* and *M*) magnification projection images of collagen architecture from normal peritoneum (*J* and *K*) and around tumor regions (*L* and *M*). (*N* and *O*) Representative Fourier transforms from the full images shown in *K* and *M*, respectively. Gaussian ellipses (blue) are fit to determine the collagen fibril asymmetry. MPM images were acquired using 780-nm excitation. Blue and yellow pseudo colors represent 355 to 425 nm and 450 to 550 nm emission, respectively. For clarity, the SHG images are reproduced in gray in *C, F*, and *I* to *M*. Scale bars: 30 *μ*m (*A*-*C*), 22 *μ*m (*D*-*F*), 45 *μ*m (*G*-*I, J*, and *L*) and 12 *μ*m (*K*, and *M*).

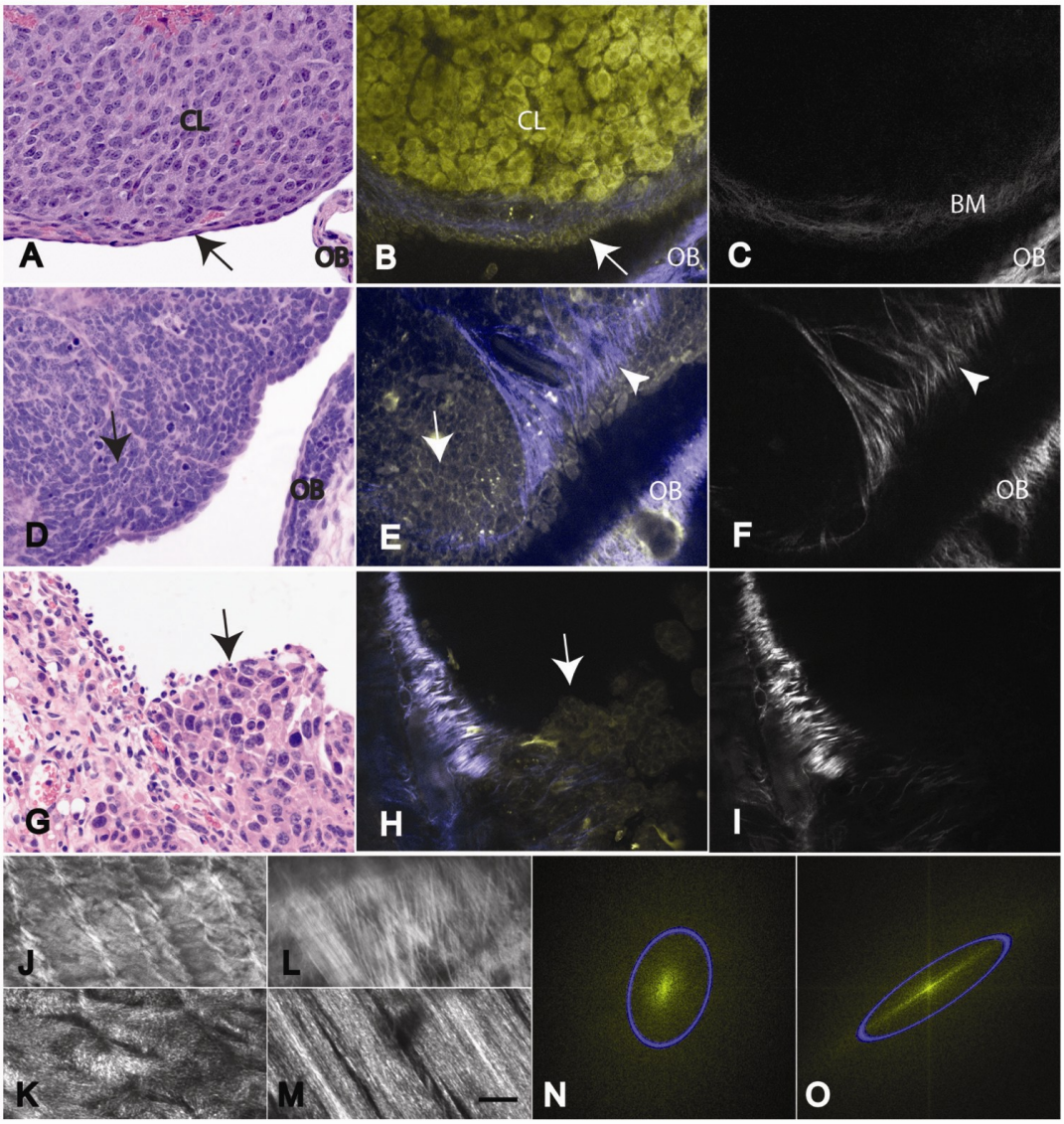
CL
A
OB
CL
B
OB
BM
C
OB
D
OB
E
OB
F
OB
G
H
I
J
L
K
M
N
O

H&E staining, neoplastic features, such as high nuclear-cytoplasmic ratios, variations in cell sizes and altered tissue architecture were easily identifiable. MPM/SHG imaging also allowed better visualization of collagenous stroma (Fig. 4.1, *B*, *C*, *E* and *F*) and demonstrated that the majority of collagen fibers near the invasive edge are located perpendicular towards its surface (Fig. 4.1, *E* and *F*). At the same time, H&E sections were essential for evaluation of such key pathological characteristics as nucleoli, chromatin condensation and overall tinctorial properties of tissues. Identification of mitotic and apoptotic cells was also problematic with MPM/SHG alone.

To extend the generality of these observations, we developed and evaluated a new model of disseminated peritoneal EOC. In this model, OSE transformed by *p53* and *Rb* inactivation and c-Myc overexpression form multiple neoplastic tumors on the visceral and parietal walls of the abdominal cavity 3 to 5 weeks after intraperitoneal injection. Similar to neoplasms of Tg*MISIIR-TAg* mice, neoplastic cells were identified by both H&E and MPM/SHG imaging (Fig. 4.1, *G* and *H)* in all 10 studied cases. Notably, these tumors also had an aberrant appearance and orientation of collagen (Fig. 4.1, *H* and *I*). Fibrils underlying normal peritoneal mesothelium were relatively uniform and had a wavy appearance, whereas those around tumor masses had variable diameter and a straight-rigid appearance. Uniformity and appearance aberrations were well discernable (at low and high resolution, respectively) by projecting optical slices from a collagen image stack underlying mesothelium (Fig. 1, *J* and *K*) or neoplastic cells (Fig. 4.1, *L* and *M*). Alignment properties were automatically analyzed by computing FFT's of the projected images and fitting Gaussian ellipses to the resulting Fourier components. FFT's from normal (Fig. 1*N*) and carcinomatous (Fig. 4.1*O*)

peritoneum image stacks revealed a significant increase in asymmetry (P = 0.0456) of the tumor fibrils with respect to normal fibrils (mean ± SE; 3.0 ± 0.6, n = 4 *vs.* 1.49 ± 0.02, n = 4). A potential difference in segmental collagen indicative of fibrillogenesis (observable as micron-scale spots in the images, see Williams et al., 2005) was also investigated. Collagen segments were hypothesized to be more numerous in the cancer tissues owing to an increased collagen turnover in these tissues (see for example Kenny and Lengyel, 2009). However, the amount of observable segmental collagen was found to be fairly equivalent in the cancer and control tissues. We next tested the application of MPM/SHG to human samples. Comparative analysis of normal ovary (Fig. 4.2, *A* and *B*, n = 8) and ovarian adenocarcinomas (Fig. 4.2, *C* and *D*, n = 4) confirmed that this approach provides a level of detail similar to that obtained with standard histological processing, with previously noted advantages and limitations. Consistent with observations in mouse models and studies in human tissues (Kirkpatrick et al., 2007), collagen from human EOC tumors was generally observed in thicker, less uniform bands than that from normal ovaries (Fig. 4.2, *D* versus *B*).

4.4.2 MPM-based Morphometric Analysis Allows Detection of Early Changes during Ovarian Carcinogenesis. According to literature reports, in humans, early ovarian lesions can be identified according to their morphometric parameters, such as enlarged cellular and nuclear size (Deligdisch et al., 1995; Deligdisch and Gil, 1989; Deligdisch et al., 1999; Deligdisch et al., 1993; Gil and Deligdisch, 1989). However, because identification of such lesions is usually accompanied by ovariectomy, their progression to carcinoma remains unconfirmed. In order to reproducibly

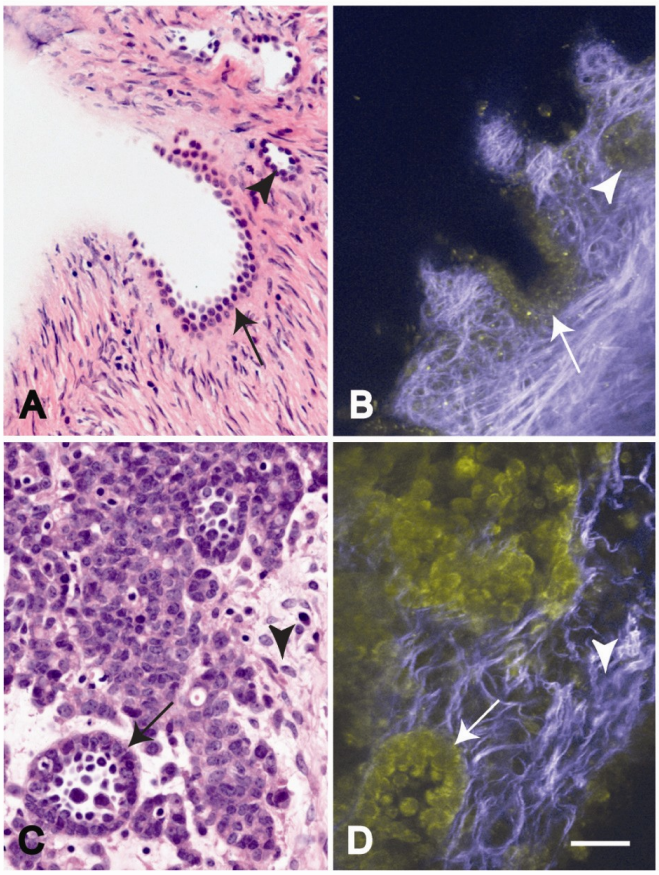

Figure 4.2. Standard histology and MPM/SHG of human ovarian epithelium and poorly differentiated adenocarcinoma. The same tissue specimens were visualized after formalin fixation and paraffin embedding followed by H&E staining (*A* and *C*) and before fixation using MPM/SHG of intrinsic tissue emissions (*B* and *D*). (*A*, *B*) Morphologically normal ovarian epithelium in the invaginations (arrow) and simple cysts (arrowhead) near the surface of of the ovary. (*C-D*) Atypical neoplastic cells forming glandular structure (arrow) within desmoplastic stroma (arrowhead). Note presence of collagen fibrils imaged via second harmonic generation (SHG; blue), a feature not readily evident in conventionally prepared tissue. MPM/SHG images are acquired as in Fig. 1. Scale bar, 30 μm in all images.

examine early events associated with ovarian carcinogenesis we turned to our model of serous ovarian adenocarcinoma initiated by conditional inactivation of OSE *p53* and *Rb* after a single transinfundibular intrabursal injection of AdCre (Flesken-Nikitin et al., 2003). This model is uniquely suited for such studies because of temporal and local control of the initiating event. EOC develop relatively synchronously and lead to death in 97% of mice with median survival of 227 days after gene inactivation (Flesken-Nikitin et al., 2003).

Similar to other ovarian samples, neoplastic lesions discernable by pathological evaluation of H&E sections were readily detectable by MPM/SHG (Fig. 4.3, *A* and *B*). Furthermore, MPM/SHG allowed detection of a thickening of the collagen fibers at or near the basement membrane underlying early dysplastic lesions (compare Fig. 4.3, *C* and *D* to Fig. 4.1, *B* and *C*). After confirming our earlier observations that over 90% of OSE cells are infected after administration of 5 x 10^7 pfu/µl of adenovirus (Fig. 3*E* and Flesken-Nikitin et al., 2003), we next tested whether MPM/SHG optical sectioning could facilitate detection of morphological alterations at 8 and 34 days after conditional inactivation of p53 and Rb. No changes in cellular morphology and histological architecture were detected by visual evaluation of either H&E or MPM sections. However, a quantitative morphometric assessment of MPM sections taken in parallel to the ovarian surface, demonstrated a significant enlargement of nuclei and cytoplasm of OSE 8 and 34 days after initiation of carcinogenesis (Figue 4.3, *F-H*). Interestingly nuclear-cytoplasmic ratios were not changed to any significant extent (P = .6547 and .3761 at day 8 and 34, respectively).

Figure 4.3 Ovarian surface epithelium carcinogenesis associated with conditional inactivation of *p53* and *Rb* genes. Multilayered atypical cells forming papillary structures (arrows) can be identified by conventional microscopy (*A*) and MPM/SHG (*B*). Thickening of the collagen fibrils (arrowheads) near and at the basement membrane of early dysplastic lesion (arrow) is evident in the MPM/SHG image (*C*) with the SHG reproduced in grayscale for clarity (*D*). (*E*) Expression of eGFP in the OSE of a mouse ovary after a single ovarian intrabursal injection with 5 x 10^7 pfu/μl of AdCMVEGFP. Arrow indicates OSE; *CL*, corpus luteum; *F*, follicle; and *V*, vessel. Green pseudocolor is GFP fluorescence and yellow is intrinsic fluorescence (< 500 nm emission). (*F*) Morphometric evaluation of intrinsic emission images of mouse OSE. Size of individual cells and their nuclei and cytoplasm was assessed by estimation of area (white rings, μm^2, mean ± SE). (*G*) Results are plotted for images collected at 8 days after intrabursal administration of AdCMVCre (Cre) or AdCMVLacZ (LacZ) to p53floxPRb1floxP mice. Unpaired t test yielded 2-tailed *P* values of .0002 for whole cell Cre versus LacZ (171.4 ± 12.4, *n* = 45 vs. 120.4 ± 6.0, *n* = 53), *P* = .0466 for nucleus Cre versus LacZ (74.8 ± 5.3, *n* = 45 *vs* 53.0 ± 10.7, *n* = 26) and *P* = .0009 for cytoplasm Cre versus LacZ (96.58 ± 8.7, *n* = 45 vs. 65.6 ± 3.78, *n* = 53). (*H*) At 34 days after transformation, unpaired *t* test yielded 2-tailed *P* = .0007 for whole-cell Cre versus LacZ (130.4 ± 6.5, *n* = 40 *vs* 92.1 ± 8.8, *n* = 36), *P* = .015 for nucleus Cre versus LacZ (70.0 ± 4.5, *n* = 40 *vs* 53.4 ± 4.9, *n* = 36), and *P* = .0007 for cytoplasm Cre versus LacZ (60.38 ± 4.3, *n* = 40 *vs* 38.6 ± 4.3, *n* = 36). All experiments have been performed in duplicates, and yielded similar results. Scale bars, 15 μm (*A, B*), 20 μm (*C*, *D*), 30 μm (*E*) and 12 μm (*F*).

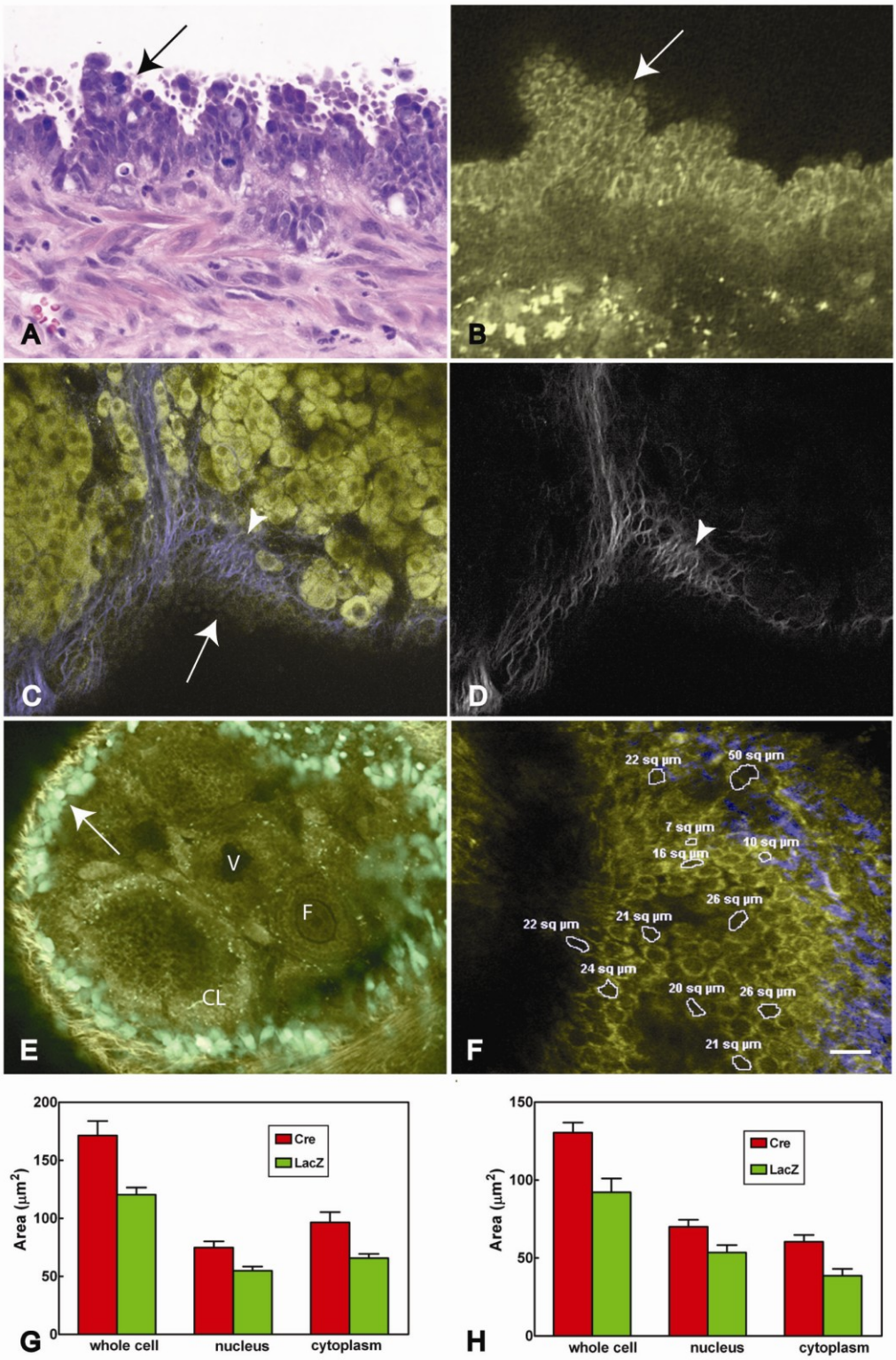
A
B
C
D
V
F
CL
E
22 sq µm
50 sq µm
7 sq µm
16 sq µm
10 sq µm
26 sq µm
22 sq µm
21 sq µm
24 sq µm
20 sq µm
26 sq µm
21 sq µm
F
Area (µm²)
200
150
100
50
0
Cre
LacZ
whole cell
nucleus
cytoplasm
G
Area (µm²)
150
100
50
0
Cre
LacZ
whole cell
nucleus
cytoplasm
H

4.4.3 Quantitative Changes in Intrinsic Fluorescence Properties of Ovarian Cancers. Because the intracellular fluorescence signal in epithelial cells is thought to derive primarily from NAD(P)H, we hypothesized that characteristics of this signal - intensity, spectrum or anisotropy - may yield further information about the metabolic state of cells. We initially tested these parameters in primary OSE cells carrying floxed *p53* and *Rb* genes three passages after exposure to AdCre or AdLacZ (control). Indeed intensity in cells with *p53*/*Rb* deletion was significantly lower (60 ± 4%, mean ± SE, n = 32 images) than that of the normal population (100 ± 12, n = 16 images, P = .0003). We also observed a slight spectral red shift in cell cultures (not shown). Both characteristic changes seemed correlated with a vesicular production of a fluorescent material not evident in the normal cells *in vivo*.

The third parameter tested was steady state emission anisotropy of the intrinsic fluorescence signal. Such a measurement is expected to yield information about the amount of time the fluorophore has rotated with respect to its fluorescence lifetime. For example, the rotation time (and fluorescence lifetime) can change upon NADH binding to a high molecular weight protein. Intrinsic fluorescence anisotropy in neoplastic OSE cells (0.301 ± 0.001, mean ± SE, n = 25 images) was significantly (P < .0001) lower than that found in normal OSE cells (0.319 ± 0.003 mean ± SE, n = 25 images). These results may indicate that more metabolically active cells, such as neoplastic cells, have a higher fraction of free to bound NAD(P)H (as has been shown in transformed mammary cell cultures, Yu and Heikal, 2009).

However, in mice, we determined that intensity and anisotropy values were highly sensitive to tissue scattering and thus depended on the amount and type of tissue through which the image was obtained. Accordingly,

intensity and anisotropy analyses of tissues have yielded inconsistent results (not shown).

At the same time, a red-shift in the average cellular intrinsic fluorescence was reproducibly observed in tumor-derived cell masses as compared to normal OSE. MPM images of freshly excised tissue from the disseminated metastasis model (Fig. 4.4) exhibited a LW/SW ratio that was significantly higher in neoplastic *versus* normal cells (1.3 ± 0.1, mean ± SE, n = 7 tumors, *vs* 1.00 ± 0.03, n = 9 ovaries, P = .0064). Intriguingly, the spectral shift in tumors appeared to arise mainly from a separate population of red-emitting cells within the tumor mass (Fig. 4.4*D*). These red-emitting cells were found to be viable by analysis of NADH intensity and co-staining with the vital stain calcein-AM (data not shown).

4.4.5 Intravital MPM of ovarian cancer using laparoscopic stick objective.

It has been previously demonstrated that under specific experimental conditions, usually in combination with research fluorophores, MPM may be used for imaging in living animals (Zipfel et al., 2003; Brown et al., 2001; Condeelis and Segall, 2003). To examine the feasibility for *in vivo* applications without contrast agents, we imaged ovaries from live mice (Fig. 4.5, *A*-*F*) by exteriorizing the ovary to isolate it from the body cavity. This method was sufficient for resolving single OSE cells in unstained ovaries (Fig. 4.5, *A*-*C*) and for discriminating these normal OSE from early EOC neoplasias using the floxed *p53/Rb* model (Fig. 4.5, *D*-*F*).

However, standard large diameter microscope objectives preclude access to internally located organs and tissues. In addition, to collect images at micronmeter-scale resolution, strategies for mitigating motion artifacts

Figure 4.4 Emission color changes in intrinsic fluorescence of epithelial ovarian carcinoma (EOC). Normal OSE (*A* and *B*) and neoplastic cells from the disseminated peritoneal EOC model (*C* and *D*) were analyzed for the relative amounts of long-to-short wavelength (LW/SW, 510-650 nm/410-490 nm, green/red pseudocolor) intrinsic fluorescence. For reference, SHG from the collagen of the ovarian bursa is shown in blue pseudocolor. Intrinsic fluorescence images of OSE are manually marked (green masked areas, *A* and *C*). The white boxes mark the zoomed regions shown in *B* and *D* respectively. (*E*) Analysis of average pixel intensities in the green masked areas shows that tumor intrinsic fluorescence is red-shifted with respect to normal OSE due to a distinct red-emitting cell population (arrows, *D*). Average LW/SW ratios are 1.00±0.03 (mean±SE, n = 9; RU, relative units) for normal OSE and 1.3±0.1 (P value=0.0064, n = 7) for neoplasms. Data was acquired from 450 images at 780 nm excitation. The calibration bar is 50 μm (*A* and *C*) and 25 μm (*B* and *D*).

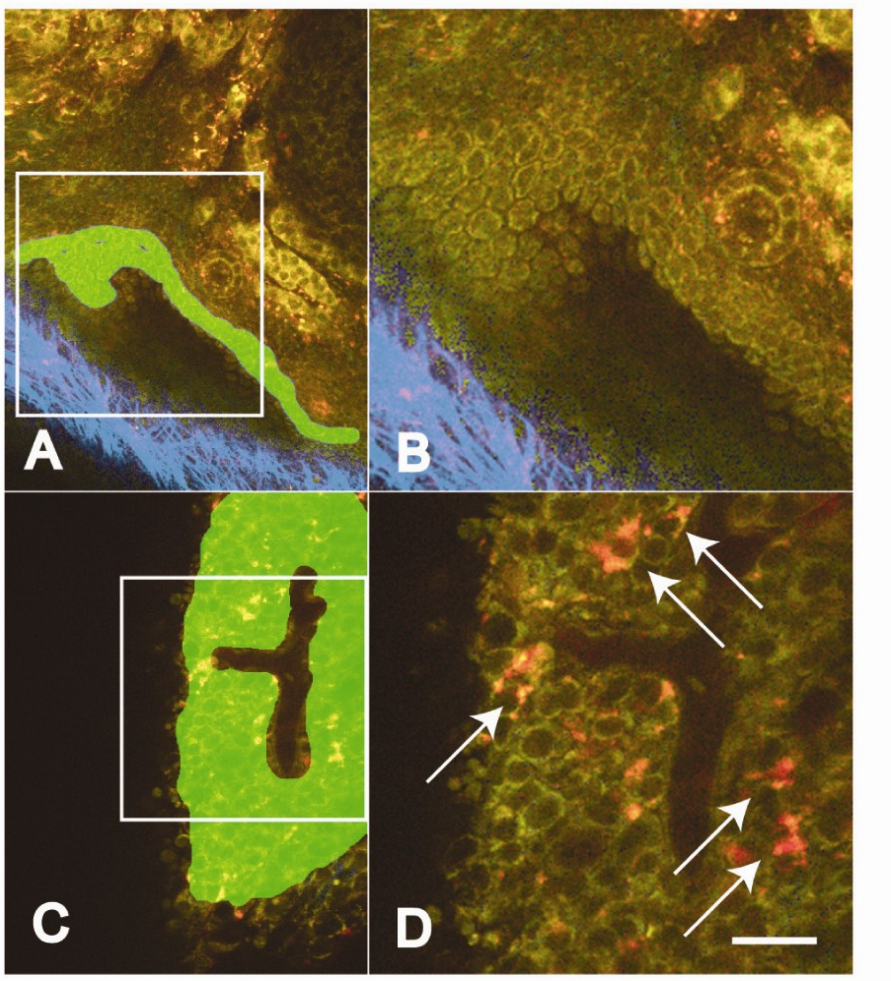
A
B
C
D

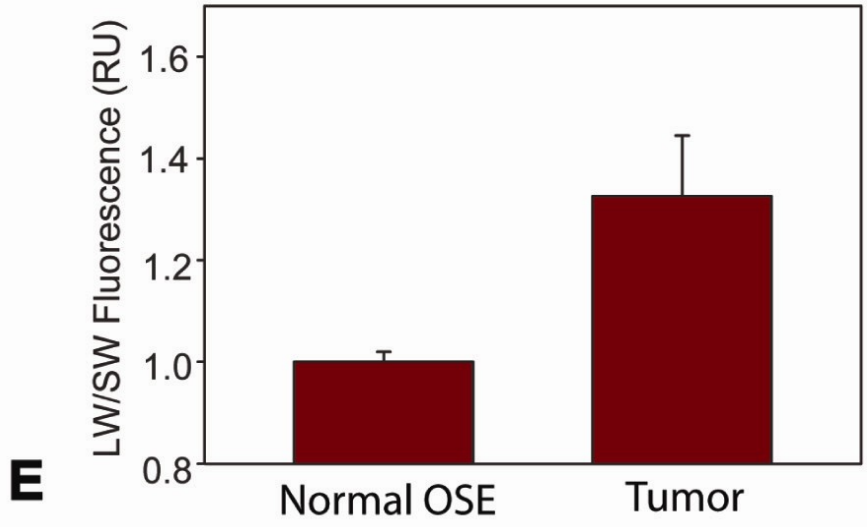
E
LW/SW Fluorescence (RU)
1.6
1.4
1.2
1.0
0.8
Normal OSE
Tumor

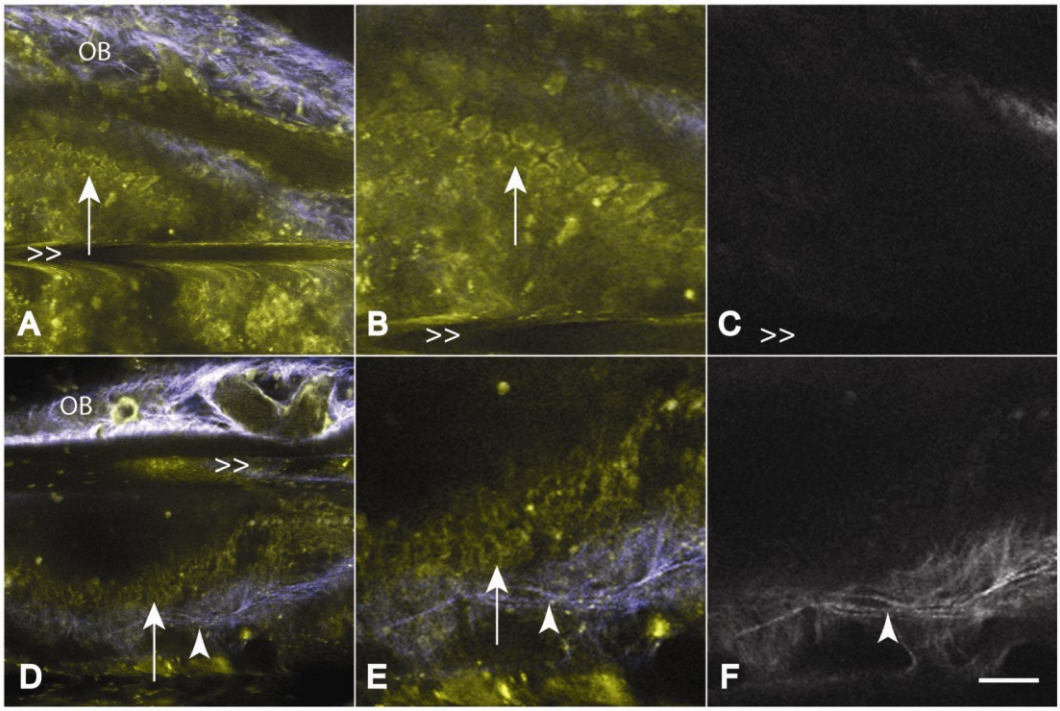

Figure 4.5. Discriminating normal from neoplastic OSE in live mice using MPM/SHG. Images of normal (*A*-*C*) and transformed (*D*-*F*) OSE mice from the conditional inactivation of *p53* and *Rb* model are acquired by exteriorizing the ovary and imaging with a standard objective lens. In zoomed images from *A* and *D* respectively, OSE (arrows) are resolvable as a single layer in normal ovaries (*B*) and in multiple layers in neoplasia (*E*). In addition, the SHG channel (*C*, *F*) shows that the collagenous layer underneath of the OSE is visibly thicker in the neoplasia (arrowhead). OB marks the ovarian bursa and >> marks horizontal motion artifacts due to mouse breathing. Scale bars, 30 *μ*m (*A* and *D*) and 15 *μ*m (*B*, *C*, *E* and *F*).

primarily due to patient breathing must be in place. To address these challenges we tested a microprobe "stick" objective recently developed by Olympus. This series of optics are fully aberration corrected objective lenses with small-diameter (1.2 and 3.2 mm) centimer-long tips. We found simple GRIN lenses to be ineffective for collection of high-quality intrinsic emission images due presumably to their more significant aberrations. In agreement with our previous results demonstrating the applicability of the Olympus microprobe objective for MPM imaging of intrinsic fluorescence of excised colon tissues (Rogart et al., 2008), we could successfully image ovarian and peritoneal tissues without staining (not shown). After additional improvements for tissue rinsing and stabilization by supplementary tubing, we were able to image the parietal and visceral mesothelium and underlying tissues of the peritoneal cavity. Importantly, neoplastic cells were readily discernable from surrounding normal tissues in the mouse model of disseminated peritoneal EOC (Fig. 4.6).

4.4.6 Combination of low magnification screening with high resolution MPM optical biopsy. A potential limitation of the stick objective lens is its small field of view. To facilitate intravital screenings of neoplastic lesions across large areas, mice were intraperitoneally injected with ProSense 680, a complex that emits red light upon cathepsin B-mediated hydrolysis. In agreement with previous results (Gounaris et al., 2008), this indicator of protease activity has been effective in detection of neoplastic disseminated peritoneal EOC cells by low magnification both with standard and multiphoton excitation (Fig. 4.7, *A*-*D*). Selected areas were subsequently visualized by the laparoscopic objective lens (Fig. 4.7, *E* and *F*) enabling visualization of

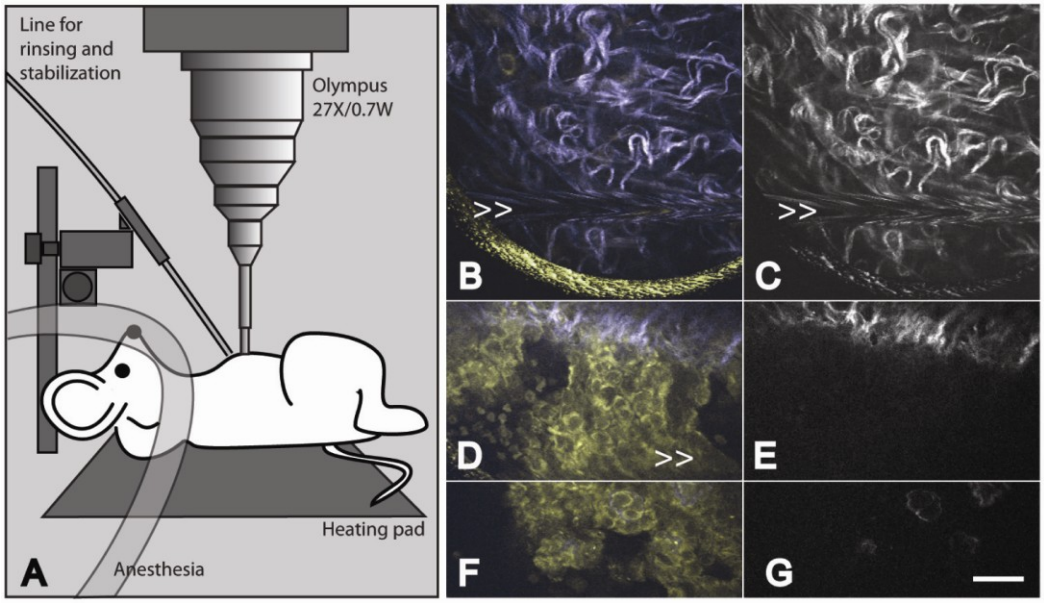

Figure 4.6 Intravital MPM/SHG imaging in the abdominal cavity using a microprobe objective lens (diagram, A). Normal peritoneum (*B* and *C*) and neoplastic cells of the disseminated peritoneal EOC model (*D*-*G*) imaged *in vivo* and *in situ* through an abdominal incision. Normal mesothelium is very thin, has low intrinsic fluorescence and is essentially invisible using intravital MPM. However neoplastic lesions are clearly visible at the invasive edge (*D* and *E*) and at the tumor surface (*F* and *G*). For clarity SHG images are reproduced in grayscale in *C*, *E* and *G*. Motion artifacts due to mouse breathing are marked with >>. The yellow meniscus at the bottom of (*B*) is the edge of field of view of the stick objective lens. The calibration bar is 30 *μ*m.

Figure 4.7 Imaging cathepsin activity using MPM/SHG. Images of the normal peritoneum (*A, C*, *E*, and *G*) and peritoneal tumors (*B*, *D*, *F* and *H*, arrows) from the disseminated peritoneal model after administration of ProSense 680 (red). Detection of neoplastic lesion using standard stereo fluoroscopy (*A* and *B*) and subsequent mapping its tumor boundaries (*D*, arrowheads) in three dimensions with MPM/SHG. In this case normal (*C*) and tumor (*D*) images were collected with a low-magnification objective (4x/0.28 NA) and displayed as projections, each from 100 images at 5-*μ*m intervals. Discrimination between normal abdominal wall (*E*) and neoplasm (*F*) at cellular resolution with the stick objective. High-resolution MPM/SHG images demonstrate cathepsin activity in certain stromal cells (*G*, arrowheads) and neoplastic cells (*H*, arrow). Additionally they show alterations in the size and shape of neoplastic cells and tissue architecture as well as the orientation of collagen fibrils towards tumor boundary (*H*, arrowhead). Scale bars, 1000 *μ*m (*A*, *B*), 500 *μ*m (*C*, *D*), 80 *μ*m (*E*, *F*), and 100 *μ*m (*G*, *H*).

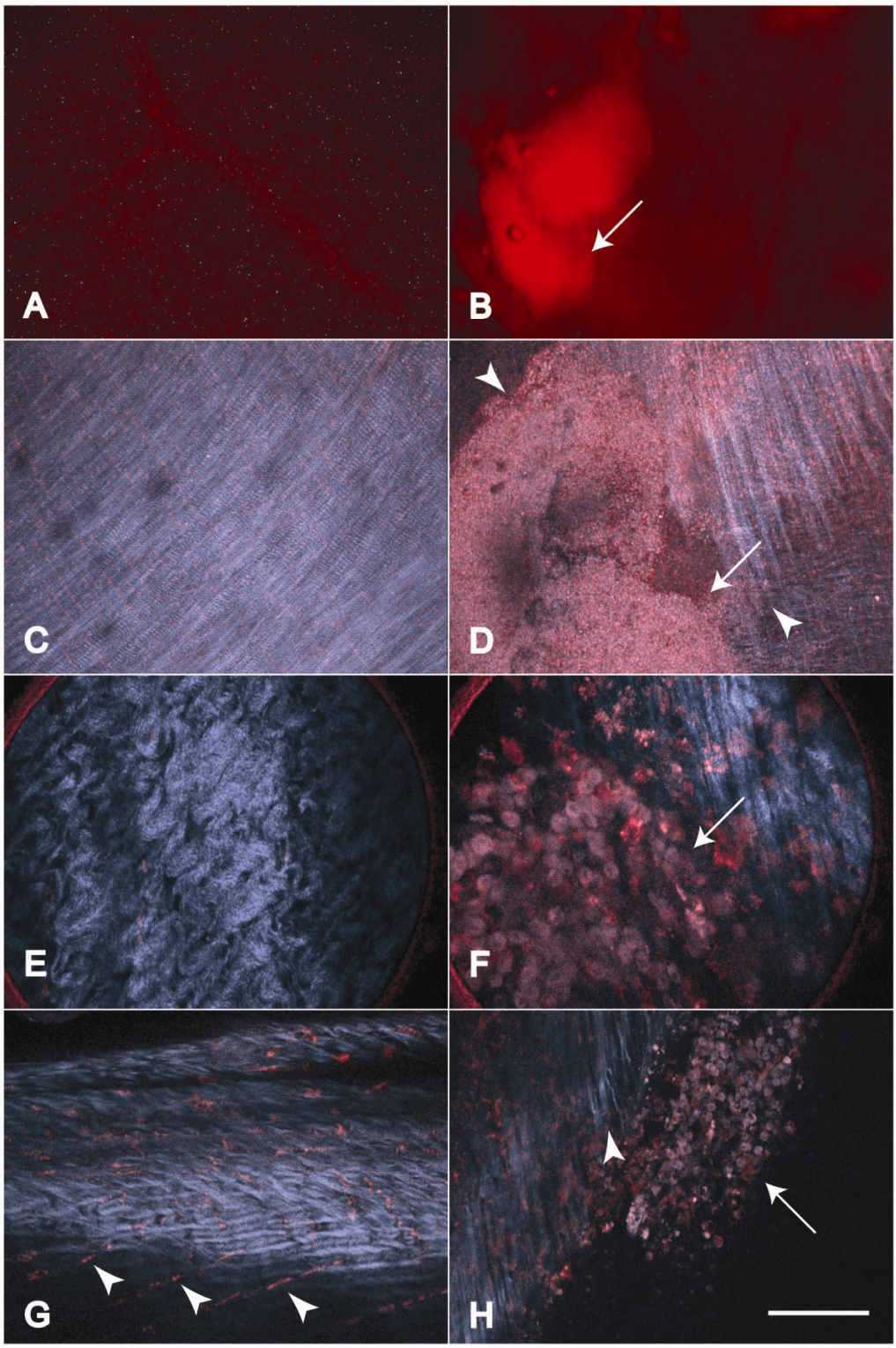
A
B
C
D
E
F
G
H

individual cells with cathepsin B activity. Whereas most fluorescent cells were neoplastic cells, capillaries and intra-muscular cells underneath of the parietal peritoneum (Fig. 4.7*G*) were also detected in agreement with earlier observations (Gounaris et al., 2008). MPM/SHG enabled a detailed mapping of the tumor boundary in three dimensions, confirming our earlier observations that collagen fibrils around tumors were straighter and orientated towards the tumor boundary at the invasive front (Fig. 4.7*H*).

4.5 Discussion

Minimally invasive or noninvasive methods of cancer diagnosis and therapeutic assessment in humans and real-time monitoring of carcinogenesis in experimental animals remain among the most coveted, challenging goals of cancer research. Undoubtedly, such abilities would tremendously facilitate our understanding of cancer initiation and progression, as well as enable development of patient-tailored therapeutic approaches. Two recent developments have provided an exciting premise for further studies. Firstly, there has been recent remarkable progress in technologies allowing noninvasive imaging of molecular and cellular processes (Weissleder and Ntziachristos, 2003; Weissleder and Pittet, 2008). Secondly, technological progress in manipulating and genetically modifying the mouse genome has led to rapidly expanded repertoire of accurate cancer models that genetically and phenotypically mimic human cancers (reviewed in Jonkers and Berns, 2002; Van Dyke and Jacks, 2002; Frese and Tuveson, 2007).

Both advances have stimulated the evolution of fluorescent contrast agents for detection and monitoring of cancer (Pierce et al., 2008; Weissleder

and Ntziachristos, 2003). Problems with these agents include reporter specificity, induced toxicity and appropriate delivery strategies. Endogenous emitters, in contrast, are integral to the tissue. Although their photophysical characteristics are generally inferior (dim and emitting at short wavelengths that scatter easily in tissue), intrinsic tissue emissions exhibit signature properties of the natural tissue (Zipfel et al., 2003a). Because emission spectra are independent of the mode of excitation (i.e., conventional UV illumination *vs* two-photon excitation), the interpretation of multiphoton intrinsic tissue fluorescence images initially relies on a broad body of one-photon excitation tissue spectroscopy and imaging experiments (for reviews, see Ramanujam et al., 2000; Richards-Kortum and Sevick-Muraca, 1996), in which significant effort has been dedicated towards identifying spectral characteristics of intrinsic tissue that discriminate between normal and dysplastic or neoplastic tissues. Generally empirical diagnostic criteria are established by analyzing the spectral shape of the intrinsic fluorescence excitation and/or emission curves by using a training set of cancerous *versus* normal specimens. This strategy has proven successful for a wide variety of cancerous tissues (Avrillier et al., 1997; Brancaleon et al., 2001; Coghlan et al., 2001; Heintzelman et al., 2000; Li and Xie, 2005; Majumder et al., 2000; Qu et al., 2002; Qu et al., 2000; Ramanujam et al., 1994; Wang et al., 1999; Zheng et al., 2003) and has been implemented in endoscopic devices for early detection of cancerous lesions in cervix (Ramanujam et al., 1994), colon (Wang et al., 1999), bladder (Avrillier et al., 1997), skin (Brancaleon et al., 2001), oral cavity (Heintzelman et al., 2000; Majumder et al., 2000; Qu et al., 2000), and esophagus (Georgakoudi and Feld, 2004). Typically, spectral measurements are taken at a single point in the tissue, the location of which is

guided by a white-light endoscope. Recently, however, imaging intrinsic fluorescence endoscopes have been developed (the LIFE-GI and Olympus Auto-Fluorescence Videoscope systems) that show diagnostic potential for gastric (Namihisa et al., 2003), lung (Kobayashi et al., 2001) and colon (Ikeda et al., 2003) cancers.

Albeit useful, the resolution of these systems is in the millimeter range, precluding detection and characterization of microscopic lesions as well as evaluation of tissue properties at the single-cell level. Nonlinear imaging approaches, such as MPM and SHG have the potential to address this current limitation (Zipfel et al., 2003b). However, their applicability to clinical settings greatly depends on several advances including 1) the development of diagnostic criteria comparable to those obtained from routine histological imaging; 2) the ability to obtain clear images in a difficult environment with significant optical scattering from blood (Cheong et al., 1990) and motion artifacts from breathing and heart beat; 3) the development of endoscopic instruments compatible with ultrafast optics, enabling minimally invasive access to target organs and tissues; with high enough sensitivity to collect weak intrinsic fluorescence signals, and (4) improvements in the ability to locate regions for high resolution assessment by MPM/SHG (better integration of the low- to high-magnification switch).

4.5.1 MPM/SHG Diagnostic Criteria. In the present study we have tested the feasibility of MPM/SHG imaging in ovarian cancer, where the need for early diagnosis and thorough assessment of effectiveness of debulking surgery is of particular importance. Because translation of new diagnostic tests and approaches into clinical practice and, particularly into pathology greatly

depends on the ability for linking new diagnostic criteria with already established and clinically proven sets of features, we have taken a particular attention to advantages and disadvantages of imaging of native tissues with MPM as compared to routine microscopy of H&E histological slides. Side-by side- evaluation of EOC specimens from human patients and mouse models has demonstrated that MPM/SHG was sufficient to detect features of neoplasia such as size and shape of cellular compartments and tissue architecture. In addition, MPM/SHG images of tissue emissions provided information that was different to that obtained using standard histological protocols. For instance, SHG clearly delineates fibrillar collagen structure, which is not visible in standard H&E sections. However absent in MPM/SHG images were diagnostic nuclear information such as nucleoli size and shape, chromatin condensation, and localization. Furthermore, H&E color variations are also absent; cytosolic spaces are instead largely delineated by NAD(P)H fluorescence, which is sensitive to redox state (Chance et al., 2004).

The origins of many reproducible fluorescent features in the intrinsic tissue fluorescence images are still unknown. Our work contributes to the development of an atlas or database for interpreting intrinsic tissue emission changes characteristic of different lesions. Such efforts complement those by other laboratories (Han et al., 2008; Kirkpatrick et al., 2007; Mukherjee et al., 2009; Provenzano et al., 2008; Rogart et al., 2008; Skala et al., 2005).

In addition to the direct applicability of MPM/SHG imaging for diagnosis of neoplasia according to established pathological criteria, several of its intrinsic features are particularly attractive for facilitation of diagnosis. Firstly, MPM/SHG imaging allows rapid and three-dimensional pathological assessment of excised tissue with virtually no tissue preparation. This

methodology should be useful in a clinical situation requiring fast three-dimensional images of biopsies or in live tissue studies where tissue fixation cannot be used because it perturbs the tissue architecture or processes under study. We demonstrate here that MPM/SHG “optical sections" allow us to avoid time-consuming serial histological sectioning required for the accurate evaluation of a single-layered OSE. It is anticipated that further studies using this approach will simplify morphometric assessments of early ovarian lesions in humans.

Secondly, MPM/SHG imaging allowed better estimation of location and characterization of collagenous stroma. Because, metastatic progression of ovarian cancer is known to coincide with increased collagen synthesis and degradation (Kenny and Lengyel, 2009; Petri et al., 2009); we analyzed images for an increase in segmental collagen associated with fibrillogenesis in the regions surrounding tumors, but found comparable amounts. Instead we observed a thickening of collagen at the basement membrane in early ovarian neoplasias and straighter, less uniform collagen fibrils around peritoneal neoplastic implants, consistent with previous reports that stromal matrix components become rearranged in tight, linearly aligned fibers in invasive ovarian carcinomas (Quiros et al., 2008; Yamada and Cukierman, 2007). In addition, we demonstrated that most collagen fibers near the invasive edge are located perpendicular towards its surface. These results are consistent with previous reports from breast tumors (Provenzano et al., 2008), suggesting that fibrils oriented perpendicular to the tumor were correlated to tumor cell infiltration to the host stromal tissue.

Thirdly, MPM allows comprehensive evaluation of spectral changes in intrinsic fluorescence with cellular resolution. We determined that intensity and

anisotropy analyses of tissues are unlikely to yield consistent results owing to their high sensitivity to tissue scattering. Similar to a previous report from human tissue (Kirkpatrick et al., 2007), we detected a red-shift in fluorescence of neoplastic cells in mice with advanced EOC. Kirkpatrick et al. (Kirkpatrick et al., 2007), attributed this spectral shift to an increase in the overall FAD to NAD(P)H ratio. However, according to our observations, this alteration in intrinsic cellular fluorescence derives not from an average color change but from a specific population of redder-emitting cells within the tumor. These cells were determined to be alive by cellular NAD(P)H expression and calcein-AM staining, and may represent porphyrin -containing cells (Li and Xie, 2005; Nilsson et al., 1997; Onizawa et al., 2003).

4.5.2 Towards an In Vivo Implementation of Intrinsic Tissue Fluorescence MPM/SHG. Clearly, a standard multiphoton microscope cannot be used for microscopic imaging in humans. However, several recent technologic advances have made an endoscopic version of MPM/SHG - a device for *in vivo* collection of histologic-like images - to be a realistically achievable goal. Several recently developed confocal endoscopes offer remarkable cellular-scale imaging *in vivo* and are undergoing clinical trials (Lin et al., 2008; Smith et al., 2008). In these devices, motion artifacts are minimized with catheter tissue stabilization and use of suction ports. An endoscopic implementation of MPM may complement such efforts with the additional ability for imaging intrinsic tissue fluorescence and an expected several-fold increase in depth penetration (Zipfel et al., 2003b). The first challenge has been to engineer fibers through which sufficiently powerful femtosecond laser pulses can propagate with minimal temporal pulse

broadening due to dispersion. An uncompensated 1- nJ, 100 fs pulse will lengthen to ~4000 fs after traveling through a meter of optical fiber (reducing the 2P excitation potential by a factor of 40). Pulse dispersion can be partially compensated at low powers. But for higher power delivery, microstructured fibers are necessary. These are relatively large (keeping average intensities low), but only propagate a single mode due to intricate boundary conditions (Ouzounov et al., 2002a; Ouzounov et al., 2002b). Scanning is done either by wiggling the fiber (Bao et al., 2008; Delaney et al., 1994; Engelbrecht et al., 2008; Myaing et al., 2006; Smith et al., 2008) or through MEM devices (Tang et al., 2009) transferred to a gradient-index or micro-lens for focusing (Barretto et al., 2009). Several researchers have demonstrated collagen imaging through an MPM endoscope (Fu et al., 2006; Tang et al., 2009), but not yet *in vivo*. The real challenge has been to design an endoscope with the sensitivity for imaging intrinsic cellular fluorophores, which are typically 100-fold dimmer than standard fluorophores (Zipfel et al., 2003a). In the current study, we demonstrate cellular visualization *in vivo* using MPM/SHG of intrinsic emissions that can be used to identify neoplasias in several mouse models of ovarian cancer. In addition,-we demonstrate the feasibility of an *in vivo* laparoscopic implementation of MPM/SHG by using a recently developed 3-mm diameter stick objective that allows direct access to imaged tissues. In this case a separate small tube served to stabilize and rinse the tissue, the latter capability being particularly relevant to tumors that present with internal bleeding.

4.5.3 Contrast Agents for Targeting MPM/SHG to Putative Neoplastic Lesions Regions. In addition to endogenous intrinsic fluorescence, it is likely

that fluorescent contrast agents (for example ALA, Loning et al., 2006) and/or smart indicators (Mahmood and Weissleder, 2003; Pierce et al., 2008) will improve diagnostic information and signal once issues of toxicity and delivery are better understood. Others have demonstrated the utility of the cathepsin activity indicator ProSense 680 for ovarian cancer diagnostics (Sheth et al., 2009). We showed that this signal can be used to quickly identify lesions with standard fluoroscopy for subsequent cellular-resolved interrogation using MPM/SHG. ProSense 680 can be imaged simultaneously with intrinsic tissue emissions providing a contextual tissue background. Because it fluoresces in the NIR, ProSense 680 may also substantially improve the depth and accuracy to which lesions can be mapped with MPM/SHG in the difficult *in vivo* environment.

Taken together, our results demonstrate the feasibility of high resolution imaging of epithelial ovarian cancer by laparoscopic nonlinear microscopy. They also demonstrate the value of MPM/SHG imaging for rapid initial assessment of ovarian cancer samples. Further advances in photonics and microfabrication should make it possible to produce an efficient fiber-coupled multiphoton endoscope with capabilities for a minimally invasive, all-optical biopsy for a cellularly resolved diagnostic assessment of ovarian cancer lesions, as well as other malignancies.

REFERENCES

Avrillier, S., Tinet, E., Ettori, D., and Anidjar, M. (1997). Laser-induced autofluorescence diagnosis of tumors. Physica Scripta *T72*, 87-92.

Bao, H., Allen, J., Pattie, R., Vance, R., and Gu, M. (2008). Fast handheld two-photon fluorescence microendoscope with a 475 microm x 475 microm field of view for in vivo imaging. Opt Lett *33*, 1333-1335.

Barretto, R.P., Messerschmidt, B., and Schnitzer, M.J. (2009). In vivo fluorescence imaging with high-resolution microlenses. Nat Methods *6*, 511-512.

Bast, R.C., Jr., Hennessy, B., and Mills, G.B. (2009). The biology of ovarian cancer: new opportunities for translation. Nature reviews *9*, 415-428.

Brancaleon, L., Durkin, A.J., Tu, J.H., Menaker, G., Fallon, J.D., and Kollias, N. (2001). In vivo fluorescence spectroscopy of nonmelanoma skin cancer. Photochemistry and Photobiology *73*, 178-183.

Chance, B. (2004). Mitochondrial NADH redox state, monitoring discovery and deployment in tissue. Methods Enzymol *385*, 361-370.

Cheong, W.F., Prahl, S.A., and Welch, A.J. (1990). A Review of the Optical-Properties of Biological Tissues. Ieee Journal of Quantum Electronics *26*, 2166-2185 (with update at http://omlc.ogi.edu/pubs/pdf/cheong2190a.pdf).

Coghlan, L., Utzinger, U., Richards-Kortum, R., Brookner, C., Zuluaga, A., Gimenez-Conti, I., and Follen, M. (2001). Fluorescence spectroscopy of epithelial tissue throughout the dysplasia-carcinoma sequence in an animal model: Spectroscopic changes precede morphologic changes. Lasers in Surgery and Medicine *29*, 1-10.

Connolly, D.C., Bao, R., Nikitin, A.Y., Stephens, K.C., Poole, T.W., Hua, X., Harris, S.S., Vanderhyden, B.C., and Hamilton, T.C. (2003). Female mice chimeric for expression of the simian virus 40 TAg under control of the MISIIR promoter develop epithelial ovarian cancer. Cancer Res *63*, 1389-1397.

Corney, D.C., Flesken-Nikitin, A., Godwin, A.K., Wang, W., and Nikitin, A.Y. (2007). MicroRNA-34b and MicroRNA-34c are targets of p53 and cooperate in control of cell proliferation and adhesion-independent growth. Cancer Res *67*, 8433-8438.

Davis, B., Harleman, J.H., Heinrichs, M., Maekawa, A., McConnell, R.F., Reznik, G., and Tucker, M. (2001). Female Genital System. In International Classification of Rodent Tumors The Mouse, U. Mohr, ed. (Berlin, Springer), pp. 211-268.

Delaney, P.M., King, R.G., Lambert, J.R., and Harris, M.R. (1994). Fibre optic confocal imaging (FOCI) for subsurface microscopy of the colon in vivo. J Anat *184 (Pt 1)*, 157-160.

Deligdisch, L., Einstein, A.J., Guera, D., and Gil, J. (1995). Ovarian dysplasia in epithelial inclusion cysts. A morphometric approach using neural networks. Cancer *76*, 1027-1034.

Deligdisch, L., and Gil, J. (1989). Characterization of ovarian dysplasia by interactive morphometry. Cancer *63*, 748-755.

Deligdisch, L., Gil, J., Kerner, H., Wu, H.S., Beck, D., and Gershoni-Baruch, R. (1999). Ovarian dysplasia in prophylactic oophorectomy specimens: cytogenetic and morphometric correlations. Cancer *86*, 1544-1550.

Deligdisch, L., Miranda, C., Barba, J., and Gil, J. (1993). Ovarian dysplasia: nuclear texture analysis. Cancer *72*, 3253-3257.

Denk, W., Strickler, J.H., and Webb, W.W. (1990). Two-Photon Laser Scanning Fluorescence Microscopy. Science *248*, 73-76.

Engelbrecht, C.J., Johnston, R.S., Seibel, E.J., and Helmchen, F. (2008). Ultra-compact fiber-optic two-photon microscope for functional fluorescence imaging in vivo. Opt Express *16*, 5556-5564.

Flesken-Nikitin, A., Choi, K.C., Eng, J.P., Shmidt, E.N., and Nikitin, A.Y. (2003). Induction of carcinogenesis by concurrent inactivation of p53 and Rb1 in the mouse ovarian surface epithelium. Cancer Res *63*, 3459-3463.

Flesken-Nikitin, A., Toshkov, I., Naskar, J., Tyner, K.M., Williams, R.M., Zipfel, W.R., Giannelis, E.P., and Nikitin, A.Y. (2007). Toxicity and biomedical imaging of layered nanohybrids in the mouse. Toxicol Pathol *35*, 804-810.

Flesken-Nikitin, A., Williams, R.M., Zipfel, W.R., Webb, W.W., and Nikitin, A.Y. (2004). Use of multiphoton imaging for studying cell migration in the mouse. Methods Mol Biol *294*, 335-346.

Fu, L., Jain, A., Xie, H., Cranfield, C., and Gu, M. (2006). Nonlinear optical endoscopy based on a double-clad photonic crystal fiber and a MEMS mirror. Opt Express *14*, 1027-1032.

Georgakoudi, I., and Feld, M.S. (2004). The combined use of fluorescence, reflectance, and light-scattering spectroscopy for evaluating dysplasia in Barrett's esophagus. Gastrointest Endosc Clin N Am *14*, 519-537, ix.

Gil, J., and Deligdisch, L. (1989). Interactive morphometric procedures and statistical analysis in the diagnosis of ovarian dysplasia and carcinoma. Pathol Res Pract *185*, 680-685.

Gounaris, E., Tung, C.H., Restaino, C., Maehr, R., Kohler, R., Joyce, J.A., Ploegh, H.L., Barrett, T.A., Weissleder, R., and Khazaie, K. (2008). Live imaging of cysteine-cathepsin activity reveals dynamics of focal inflammation, angiogenesis, and polyp growth. PLoS One *3*, e2916.

Han, X., Burke, R.M., Zettel, M.L., Tang, P., and Brown, E.B. (2008). Second harmonic properties of tumor collagen: determining the structural relationship between reactive stroma and healthy stroma. Opt Express *16*, 1846-1859.

Heintzelman, D.L., Utzinger, U., Fuchs, H., Zuluaga, A., Gossage, K., Gillenwater, A.M., Jacob, R., Kemp, B., and Richards-Kortum, R.R. (2000). Optimal excitation wavelengths for in vivo detection of oral neoplasia using fluorescence spectroscopy. Photochemistry and Photobiology *72*, 103-113.

Helmchen, F., and Denk, W. (2005). Deep tissue two-photon microscopy. Nat Methods *2*, 932-940.

Ikeda, N., Hiyoshi, T., Kakihana, M., Honda, H., Kato, Y., Okunaka, T., Furukawa, K., Tsuchida, T., Kato, H., and Ebihara, Y. (2003). Histopathological evaluation of fluorescence bronchoscopy using resected lungs in cases of lung cancer. Lung Cancer *41*, 303-309.

Jemal, A., Siegel, R., Ward, E., Hao, Y., Xu, J., and Thun, M.J. (2009). Cancer Statistics, 2009. CA Cancer J Clin.

Kenny, H.A., and Lengyel, E. (2009). MMP-2 functions as an early response protein in ovarian cancer metastasis. Cell Cycle *8*, 683-688.

Kirkpatrick, N.D., Brewer, M.A., and Utzinger, U. (2007). Endogenous optical biomarkers of ovarian cancer evaluated with multiphoton microscopy. Cancer Epidemiol Biomarkers Prev *16*, 2048-2057.

Kloppenburg, P., Zipfel, W.R., Webb, W.W., and Harris-Warrick, R.M. (2000). Highly Localized Ca2+ Accumulation Revealed by Multiphoton Microscopy in an Identified Motoneuron and Its Modulation by Dopamine. J Neurosci *20*, 2523-2533.

Kobayashi, M., Tajiri, H., Seike, E., Shitaya, M., Tounou, S., Mine, M., and Oba, K. (2001). Detection of early gastric cancer by a real-time autofluorescence imaging system. Cancer Lett *165*, 155-159.

Kosaka, N., Ogawa, M., Longmire, M.R., Choyke, P.L., and Kobayashi, H. (2009). Multi-targeted multi-color in vivo optical imaging in a model of disseminated peritoneal ovarian cancer. J Biomed Opt *14*, 014023.

Li, B.H., and Xie, S.S. (2005). Autofluorescence excitation-emission matrices for diagnosis of colonic cancer. World J Gastroenterol *11*, 3931-3934.

Lin, K.Y., Maricevich, M., Bardeesy, N., Weissleder, R., and Mahmood, U. (2008). In vivo quantitative microvasculature phenotype imaging of healthy and malignant tissues using a fiber-optic confocal laser microprobe. Transl Oncol *1*, 84-94.

Loning, M.C., Diddens, H.C., Holl-Ulrich, K., Loning, U., Kupker, W., Diedrich, K., and Huttmann, G. (2006). Fluorescence staining of human ovarian cancer tissue following application of 5-aminolevulinic acid: fluorescence microscopy studies. Lasers Surg Med *38*, 549-554.

Mahmood, U., and Weissleder, R. (2003). Near-infrared optical imaging of proteases in cancer. Mol Cancer Ther *2*, 489-496.

Majumder, S.K., Mohanty, S.K., Ghosh, N., Gupta, P.K., Jain, D.K., and Khan, F. (2000). A pilot study on the use of autofluorescence spectroscopy for diagnosis of the cancer of human oral cavity. Current Science *79*, 1089-1094.

Mukherjee, S., Wysock, J.S., Ng, C.K., Akhtar, M., Perner, S., Lee, M.M., Rubin, M.A., Maxfield, F.R., Webb, W.W., and Scherr, D.S. (2009). Human bladder cancer diagnosis using Multiphoton microscopy. Proc Soc Photo Opt Instrum Eng *7161*, nihpa96839.

Myaing, M.T., MacDonald, D.J., and Li, X. (2006). Fiber-optic scanning two-photon fluorescence endoscope. Opt Lett *31*, 1076-1078.

Namihisa, A., Ogihara, T., Nakaniwa, N., Ohkawa, A., Sakamoto, N., Abe, S., Kobayashi, O., Terai, T., Sasaki, J., Miwa, H.*, et al.* (2003). Newly developed Auto-Fluorescence Imaging videoscope system for the detection of colonic neoplasms. Gastrointestinal Endoscopy *57*, Ab175-Ab175.

Nikitin, A.Y., Connolly, D.C., and Hamilton, T.C. (2004). Pathology of ovarian neoplasms in genetically modified mice. Comp Med *54*, 26-28.

Nilsson, H., Johansson, J., Svanberg, K., Svanberg, S., Jori, G., Reddi, E., Segalla, A., Gust, D., Moore, A.L., and Moore, T.A. (1997). Laser-induced

fluorescence studies of the biodistribution of carotenoporphyrins in mice. Br J Cancer *76*, 355-364.

Olson, S.H., Mignone, L., Nakraseive, C., Caputo, T.A., Barakat, R.R., and Harlap, S. (2001). Symptoms of ovarian cancer. Obstet Gynecol *98*, 212-217.

Onizawa, K., Okamura, N., Saginoya, H., and Yoshida, H. (2003). Characterization of autofluorescence in oral squamous cell carcinoma. Oral Oncol *39*, 150-156.

Ouzounov, D., Homoelle, D., Zipfel, W., Webb, W.W., Gaeta, A.L., West, J.A., Fajardo, J.C., and Koch, K.W. (2002a). Dispersion measurements of microstructured fibers using femtosecond laser pulses (vol 192, pg 219, 2001). Optics Communications *205*, 227-227.

Ouzounov, D.G., Moll, K.D., Foster, M.A., Zipfel, W.R., Webb, W.W., and Gaeta, A.L. (2002b). Delivery of nanojoule femtosecond pulses through large-core microstructured fibers. Opt Lett *27*, 1513-1515.

Petri, A.L., Simonsen, A.H., Yip, T.T., Hogdall, E., Fung, E.T., Lundvall, L., and Hogdall, C. (2009). Three new potential ovarian cancer biomarkers detected in human urine with equalizer bead technology. Acta Obstet Gynecol Scand *88*, 18-26.

Pierce, M.C., Javier, D.J., and Richards-Kortum, R. (2008). Optical contrast agents and imaging systems for detection and diagnosis of cancer. Int J Cancer *123*, 1979-1990.

Provenzano, P.P., Inman, D.R., Eliceiri, K.W., Knittel, J.G., Yan, L., Rueden, C.T., White, J.G., and Keely, P.J. (2008). Collagen density promotes mammary tumor initiation and progression. BMC Med *6*, 11.

Qu, J.N.Y., Chang, H.P., and Xiong, S.M. (2002). Fluorescence spectral imaging for characterization of tissue based on multivariate statistical analysis. Journal of the Optical Society of America a-Optics Image Science and Vision *19*, 1823-1831.

Qu, J.Y., Wing, P., Huang, Z., Kwong, D., Sham, J., Lee, S.L., Ho, W.K., and Wei, W.I. (2000). Preliminary study of in vivo autofluorescence of nasopharyngeal carcinoma and normal tissue. Lasers Surg Med *26*, 432-440.

Quiros, R.M., Valianou, M., Kwon, Y., Brown, K.M., Godwin, A.K., and Cukierman, E. (2008). Ovarian normal and tumor-associated fibroblasts retain in vivo stromal characteristics in a 3-D matrix-dependent manner. Gynecol Oncol *110*, 99-109.

Ramanujam, N. (2000). Fluorescence Spectroscopy In Vivo. In Encyclopedia of Analytical Chemistry, R.A. Meyers, ed. (Chichester, John Wiley & Sons Ltd.), pp. 20-56.

Ramanujam, N., Mitchell, M.F., Mahadevan, A., Warren, S., Thomsen, S., Silva, E., and Richards-Kortum, R. (1994). In vivo diagnosis of cervical intraepithelial neoplasia using 337-nm-excited laser-induced fluorescence. Proc Natl Acad Sci U S A *91*, 10193-10197.

Richards-Kortum, R., and Sevick-Muraca, E. (1996). Quantitative optical spectroscopy for tissue diagnosis. Annu Rev Phys Chem *47*, 555-606.

Rogart, J.N., Nagata, J., Loeser, C.S., Roorda, R.D., Aslanian, H., Robert, M.E., Zipfel, W.R., and Nathanson, M.H. (2008). Multiphoton imaging can be used for microscopic examination of intact human gastrointestinal mucosa ex vivo. Clin Gastroenterol Hepatol *6*, 95-101.

Scully, R.E., and Sobin, L.H. (1999). Histological Typing of Ovarian Tumours, Second edn (Berlin, Germany: Springer).

Sheth, R.A., Upadhyay, R., Stangenberg, L., Sheth, R., Weissleder, R., and Mahmood, U. (2009). Improved detection of ovarian cancer metastases by intraoperative quantitative fluorescence protease imaging in a pre-clinical model. Gynecol Oncol *112*, 616-622.

Skala, M.C., Squirrell, J.M., Vrotsos, K.M., Eickhoff, J.C., Gendron-Fitzpatrick, A., Eliceiri, K.W., and Ramanujam, N. (2005). Multiphoton microscopy of endogenous fluorescence differentiates normal, precancerous, and cancerous squamous epithelial tissues. Cancer Res *65*, 1180-1186.

Smith, L.A., Tiffin, N., Thomson, M., Cross, S.S., and Hurlstone, D.P. (2008). Chromoscopic endomicroscopy: in vivo cellular resolution imaging of the colorectum. J Gastroenterol Hepatol *23*, 1009-1023.

Tang, S., Jung, W., McCormick, D., Xie, T., Su, J., Ahn, Y.C., Tromberg, B.J., and Chen, Z. (2009). Design and implementation of fiber-based multiphoton endoscopy with microelectromechanical systems scanning. J Biomed Opt *14*, 034005.

Tingulstad, S., Skjeldestad, F.E., Halvorsen, T.B., and Hagen, B. (2003). Survival and prognostic factors in patients with ovarian cancer. Obstet Gynecol *101*, 885-891.

Wang, T.D., Crawford, J.M., Feld, M.S., Wang, Y., Itzkan, I., and Van Dam, J. (1999). In vivo identification of colonic dysplasia using fluorescence endoscopic imaging. Gastrointest Endosc *49*, 447-455.

Weissleder, R., and Ntziachristos, V. (2003). Shedding light onto live molecular targets. Nat Med *9*, 123-128.

Weissleder, R., and Pittet, M.J. (2008). Imaging in the era of molecular oncology. Nature *452*, 580-589.

Williams, R.M., and Webb, W.W. (2000). Single granule pH cycling in antigen-induced mast cell secretion. J Cell Sci *113 Pt 21*, 3839-3850.

Williams, R.M., Zipfel, W.R., and Webb, W.W. (2005). Interpreting second-harmonic generation images of collagen I fibrils. Biophys J *88*, 1377-1386.

Yamada, K.M., and Cukierman, E. (2007). Modeling Tissue Morphogenesis and Cancer in 3D. Cell *130*, 601-610.

Yu, Q., and Heikal, A.A. (2009). Two-photon autofluorescence dynamics imaging reveals sensitivity of intracellular NADH concentration and conformation to cell physiology at the single-cell level. J Photochem Photobiol B *95*, 46-57.

Zheng, W., Lau, W., Cheng, C., Soo, K.C., and Olivo, M. (2003). Optimal excitation-emission wavelengths for autofluorescence diagnosis of bladder tumors. International Journal of Cancer *104*, 477-481.

Zipfel, W.R., Williams, R.M., Christie, R., Nikitin, A.Y., Hyman, B.T., and Webb, W.W. (2003a). Live tissue intrinsic emission microscopy using multiphoton-excited native fluorescence and second harmonic generation. Proc Natl Acad Sci U S A *100*, 7075-7080.

Zipfel, W.R., Williams, R.M., and Webb, W.W. (2003b). Nonlinear magic: multiphoton microscopy in the biosciences. Nat Biotechnol *21*, 1369-1377.

Zivanovic, O., Aldini, A., Carlson, J.W., and Chi, D.S. (2009). Advanced cytoreductive surgery: American perspective. Gynecol Oncol *114*, S3-9.

CHAPTER 5

TOXICITY AND BIOMEDICAL IMAGING OF LAYERED NANOHYBRIDS IN THE MOUSE*

5.1 Abstract

Layered nanohybrids (LNH) are a promising non-viral system allowing controlled drug and DNA delivery. In order to test the toxicity of LNH consisting of a magnesium/aluminum core, mice were subjected to subcutaneous, intraperitoneal, and intravenous injections of these nanoparticles at three doses. Intravenous injections resulted in 8% (1 out of 12) lethality at doses 100 µl and 200 µl of 6.96 x 10^{-4} M solution, while all mice survived after LNH administration by any other routes. Histopathological alterations were limited to mild localized inflammatory lesions in the lungs and the dermis after intravenous and subcutaneous administration, respectively. LNH labeled with Lucifer Yellow were readily detectable in both locations by fluorescent microscopy. To test their potential for intravital imaging, LNH-Lucifer Yellow were injected into the ovarian bursa and successfully visualized by multiphoton microscopy within the ovarian surface epithelial cells. In similar experiments, the ovary and the ovarian bursa were readily detectable by magnetic resonance imaging after administration of modified LNH, where aluminum was substituted for gadolinium. Taken together, these results demonstrate minimal *in vivo* toxicity of LNH and illuminate their potential as multifunctional nanoscale particles suitable for combination of intravital biomedical imaging with controlled drug release.

*Previously published as Flesken-Nikitin et al., (2007). Toxicologic Pathology. 35:806-812.

5.2 Introduction

Nanotechnology is expected to be one of the leading technologies of the future. The reduction of material size from micro- to nano scale offers benefits to diverse scientific fields and has the potential to revolutionize medical diagnostics and care (Roco et al., 2003; Stix et al., 2001). The development of multifunctional nanoparticles for biomedical and biotechnological applications may improve cancer therapy, DNA transfection, intravital imaging, targeted drug delivery, and enzyme immobilization (Ferrari et al., 2005; Hirsch et al., 2003; La Van et al., 2002; Vijayanathan et al., 2002; Wagner et al., 2006). Though there is a growing literature on application of nanoparticles and nanotechnology, only limited information on the biological effects of nanoparticles on cells and tissues and their potential risks to humans and the environment is available (Chen and von Mikecz, 2005; Colvin et al., 2003; Donaldson et al., 2006; Holsapple et al., 2005; Oberdoerster et al., 2005; Peter et al., 2004; Service et al., 2004).

Layered nanohybrids (LNH) represent a promising class of therapeutic delivery systems. These nanoscale platform particles are based on a layered inorganic host that can intercalate various biological molecules into the nanometer size galleries between the layers. The host consists of positively charged layers of a mixed divalent/trivalent hydroxide (e.g. magnesium/aluminum as well as other cation combinations described later). The inorganic core of an LNH is like a nanoscale deck of cards. Various molecules can be incorporated between the cards while the outer surface of the deck can be treated and conjugated to different molecules for targeting. LNH are based on self-assembly, a robust, common approach in biological

systems. Traditional uses for LNH have focused on both medical and non-medical applications, for example LNH based on Mg/Al have been used for years as oral antacids. More recently, several reports describe the use of LNH in other pharmaceutical/medical applications including gene and drug storage, drug and gene delivery and enzyme immobilization (Ambrogi et al., 2003; Ambrogi et al., 2001; Choy et al., 2000a; Choy et al., 2000b; Hussein et al., 2002; Khan et al., 2001; Kwak et al., 2002; Tyner et al., 2004a; Tyner et al., 2004b). Recently, LNH were developed for delivering the nonionic, poorly water-soluble drug camptothecin or whole gene and promoter using magnesium-aluminum layered double hydroxide (Tyner et al., 2004a; Tyner et al., 2004b). These studies on glioma and choriocarcinoma cell lines and primary culture of cardiac myocytes showed that the nanohybrids were well tolerated, caused no pronounced toxicity and delivered the cytostatic drug and the functioning gene in all cell lines tested. Furthermore, they also demonstrated that LNH could be successfully functionalized and coupled with an antibody. However, biological toxicity of LNH in vivo remained unclear.

In this communication we perform initial testing to evaluate LNH toxicity *in vivo*. We further demonstrate that, in addition to their value as vehicles for controlled drug release, LNH may be suitable agents for biomedical imaging, including such advanced technologies as multiphoton microscopy and magnetic resonance imaging.

5.3 Materials and Methods

Experimental Animals. FVB/N inbred mice and mice with floxed copies of *p53* and *Rb* genes were maintained in our laboratory animal facility under 12 hours

light/dark cycle at a temperature of 20^{o}C and relative humidity of 20-50% and were monitored daily following recommendations of the Institutional Laboratory Animal Use and Care Committee of Cornell University.

Preparation of LNH. LNH were synthesized according to a previously described method (Tyner et al., 2004a; Tyner et al., 2004b). In brief, positively charged magnesium-aluminum (Mg/Al) double hydroxide forming the layered nanoparticle cores was mixed with the potassium salt of Lucifer Yellow fluorescence dye. Ion exchange allowed the incorporation of the negatively charged dye into the nanometer size galleries between the layers. Nanoparticles with inorganic gadolinium/magnesium (Gd/Mg) double hydroxide core were synthesized similarly.

Administration of LNH. LNH were administered to two to four months old mice intravenously (i.v.), intraperitoneally (i.p.) or subcutaneously (s.c.) at 6.96 x 10^{-4} M in 50, 100, and 200 µl of distilled water and mice were euthanized 3, 7, 21 and 35 days post injection. For each concentration at least 3 animals were used per each time point in each treatment group. As a control, mice were injected with distilled water and collected over the same time schedule.

Pathological Analysis. Moribund and scheduled for material collection mice were anesthetized with avertin (2.5% v/v in 0.85% NaCl, 0.020 ml/g body weight) followed by CO_2 euthanasia and subjected to careful pathological evaluation. Brain, lungs, liver, kidney, spleen, pancreas, tight muscle, eye, and skin were fixed in phosphate-buffered 4% paraformaldehyde and representative specimens were processed routinely and embedded in paraffin

as described previously (Flesken-Nikitin et al., 2003; Zhou et al., 2006). Our preliminary results demonstrated that LNH containing Lucifer Yellow (LNH-LY) can be equally well detected both in frozen and paraffin material. Thus, parallel paraffin sections were used for hematoxylin and eosin (H&E) staining and LNH detection. Distribution of LNH was assessed in either unstained or DAPI counterstained sections mounted with GEL/MOUNT (Biomeda Corp. Foster City, CA), sealed with Clarion Mounting Medium (Biomeda Corp. Foster City, CA), and imaged by fluorescence microscopy (Carl Zeiss Axioskop 2).

Primary Culture of the Ovarian Surface Epithelium (OSE). Individual ovaries were dissected from mice with floxed copies of *p53* and *Rb* genes, placed in DMEM/F12 (Ham's) medium containing Collagenase-Dispase at 5% CO_2 for 1 hour and expanded as described previously (Flesken-Nikitin et al., 2003). Inactivation of *p53* and *Rb* was achieved by recombinant adenovirus-mediated expression of Cre recombinase and gene excision was monitored by PCR as in (Flesken-Nikitin et al., 2003). Primary cell cultures of OSE deficient for *p53* and *Rb* were incubated with 6.96 x 10^{-4} mol of LNH-Lucifer Yellow for 3 to 6 hrs hours, washed three times with PBS, fixed with 4% paraformaldehyde, mounted with GEL/MOUNT and imaged by fluorescence microscopy 4 days after LNH administration.

Administration of Nanohybrids to Mouse OSE in vivo. Ten µl of LNH was delivered into the ovarian bursa by transinfundibular injection with a Hamilton syringe and a 30-gauge beveled needle under the control of a dissection microscope after deep anesthesia with intraperitoneal avertin as described

previously (Flesken-Nikitin et al., 2003). As a control, a vehicle solution was injected into the contralateral ovarian bursa.

Multiphoton and Magnetic Resonance Imaging. For multiphoton imaging freshly dissected ovaries were placed in saline and imaged within 10 min after dissection as described previously (Flesken-Nikitin et al., 2004; Zipfel et al., 2003a). Multiphoton imaging was accomplished with a water immersion Olympus XLUMPlanFl 20x/0.95NA objective and excitation at 780 nm. The tissue emission was spectrally resolved into 2 channels; a 360-500 nm band (pseudocolored yellow) was used to image tissue structure: cellular autofluorescence and second harmonic generation from collagen, and a 500-650 nm band (pseudocolored green) was used to detect the Lucifer yellow fluorescence. For magnetic resonance imaging (MRI) mice were anesthetized with avertin, placed on a heating pad and imaged in a 2 Tesla MRI scanner at the Cornell University Hospital for Animals 3 days after injection of Gd/Mg LNH.

5.4 Results

5.4.1 LNH Toxicity and Biodistribution. To assess the potential in vivo toxicity of LNH, groups of mice were subjected to single i.v., i.p. and s.c. injections with three different doses of nanoparticles as described in the Materials and Methods. One mouse per each group of 12 (8%) died within 3 days after i.v. administration of 100 µl and 200 µl at concentration 6.96×10^{-4} M of LNH. Necropsy findings included extension of alveolar capillaries by

blood, alveolar septal edema and focal intraalveolar hemorrhage. These features were consistent with acute pulmonary congestion, most likely due to the capillary obstruction by nanoparticles. No abnormal clinical signs or behaviors were detected in the remaining mice of the same groups, as well as in all mice of 50 µl i.v. group and all groups subjected to i.p. or s.c. injections. Mice were euthanized 3, 7, 21 and 35 days post injection and subjected to careful gross and microscopic pathological evaluation. Most treated organs and tissues from the treated mice showed no significant changes compared to corresponding samples from the control animals exposed to aqueous vehicle. Exceptions were the presence of inflammatory lesions at sites of subcutaneous injections and limited inflammatory lesions detected in the lungs of mice with i.v. administration of LNH.

Solitary infiltrates of mixed inflammatory cells including neutrophils, macrophages, lymphocytes and plasma cells were located in the dermis (Fig. 5.1*A*) 3 days after SC injection. At 7 and 21 days postinjection some lesions became somewhat larger and contained necrotic center surrounded by infiltrating cells and fibrous connective tissue. The lesions become smaller and more compact by 35 days after injection. In agreement with these observations, LNH-specific fluorescence was observed within inflammatory lesions 3 (Fig. 5.1*B*), 7 and 21 days after LNH administration.

Three days after i.v. administration of LNH the lungs contained small perivascular inflammatory lesions consisting of neutrophils, macrophages and lymphocytes (Fig. 5.1*C*). By 35 days postinjection these lesions were smaller in size and mainly composed of macrophages (Fig. 5.1*D*, *E*).The number of lesions decreased in a dose-dependent manner, and only a few of them were detected in the lungs of mice exposed to 50 µl of LNH. Bright and

Figure 5.1. **Histological lesions associated with injection of layered nanohybrids.** (*A*) Inflammatory response (arrow) composed of neutrophils, macrophages, lymphocytes and plasma cells in the skin of a mouse at the injection site 3 days after SC administration of 200 µl LNH. (*B*) Parallel section of the same site showing LNH-Lucifer Yellow specific fluorescence (arrow). (*C*). Small inflammatory lesion (arrow) consisting of neutrophils, macrophages, and lymphocytes 3 days after i.v. injection with LNH. (*D* and *E*) Granuloma (arrow) containing macrophage derived epithelioid cells with pale pink cytoplasm and indistinct cell borders surrounding a blood vessel 35 days after IV injection with LNH. (*F*) Lucifer Yellow fluorescence indicating LNH uptake in cells (arrow) of the same lesion as in (*E*) in a parallel section. (*A, C, D*, and *E*) Hematoxylin and Eosin. (*B* and *F*) Lucifer Yellow fluorescence. Calibration bar, A-F, 50 *µ*m.

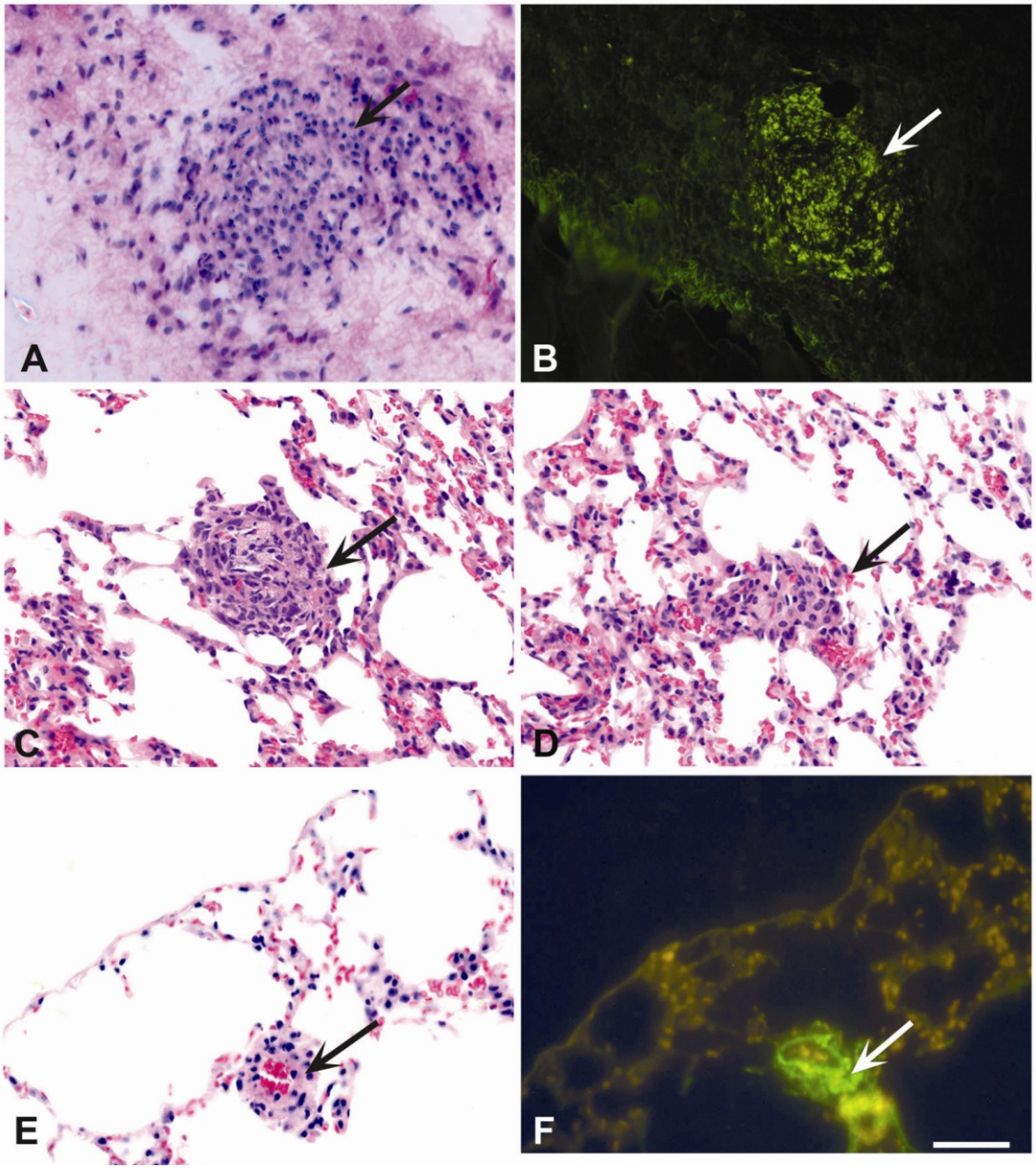
A
B
C
D
E
F

particulate fluorescence of LNH was observed within inflammatory lesions of the lung at all time points of observation including 35 days postinjection (Fig. 5,1*F*). Punctate fluorescence was also detected in single liver Kupffer cells of IV-treated mice, although no pathological changes were observed. No specific nanohybrid fluorescence was detected in any other tissues at the time points and routes of application studied.

5.4.2 Biomedical Imaging of LNH

For assessment of potential clinical applications of the LNH, recently established approaches for targeting ovarian surface epithelium (Flesken-Nikitin et al., 2003; Nikitin and Hamilton, 2005) were undertaken.

Since prior LNH toxicity and delivery studies on epithelial cells mainly utilized established cell lines, such as 9L glioma cells and JEG3 choriocarcinoma (Tyner et al., 2004a; Tyner et al., 2004b), we tested the efficacy of LNH targeting in primary culture of mouse OSE cells acutely transformed by *p53* and *Rb* inactivation. Four days after administration over 80% of OSE retained LNH with no detectable change in their morphology (Fig. 5.2 *A -D*), extent of cell death or rate of proliferation (not shown).

To extend these studies to animal models, LNH were injected into the ovarian bursa of living mouse resulting in exposure of OSE *in situ* (Flesken-Nikitin et al., 2003). Using multiphoton microscopy (Zipfel et al., 2003a; Zipfel et al., 2003b), LNH were easily detected in the OSE four days after administration (Fig. 5.2 *E-F*). Serial optical section of confirmed intracellular location of LNH. Parallel histological evaluation did not demonstrate any

Figure 5.2 Detection of fluorescent layered nanohybrids in the ovarian surface epithelium in cell culture and living mice. Nanobiohybrids labeled with Lucifer Yellow (*A, B, E*) or control aqueous solvent (*C, D, F*) have been administered to primary cell culture of OSE deficient for *p53* and Rb (*A-D*) or to the ovarian bursa of living mouse (*E, F*). Phase contrast (*A, C*), fluorescent (*B, D*) and multiphoton images (*E, F*) were collected 4 days after nanobiohybrid administration. Lucifer yellow fluorescence is present in *B*, and *E* (pseudocolored in green). OSE is indicated by arrows in *E* and *F*. Calibration bar, *A-D*, 50 *μ*m, *E, F*, 40 *μ*m.

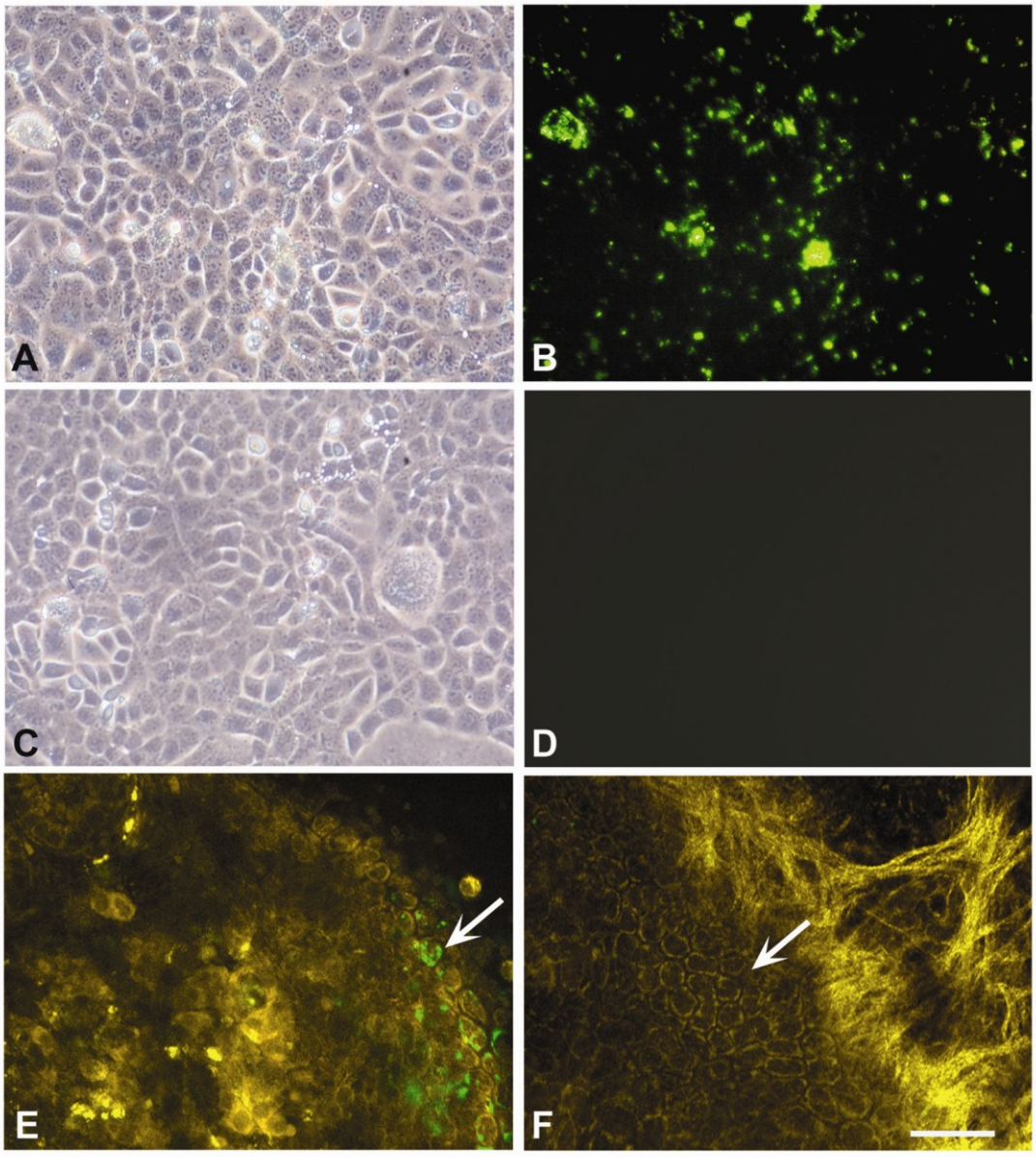
A
B
C
D
E
F

significant toxicological effects of LNP within this time frame after their administration.

In order to test potential application of LNH in conjunction with MRI, the aluminum of the Al/Mg double hydroxide core was substituted with gadolinium, which is commonly used for clinical MRI as a contrasting agent. The intrabursal administration of Gd-based nanoparticles (n = 4) was tolerated well, resulted in increased contrast of the mouse ovary and demonstrated periovarian retention of nanoparticles 3 days after injection (Fig. 5.3).

5.5 Discussion

With the exponential increase of new types and uses of nanoparticles there is clearly a call for more research on toxicology of nanomaterials in order to determine potential health risks (Maynard et al., 2006; Service et al., 2005). The risk assessment studies on graphite, metal oxide and quartz nanoparticles revealed complex relationship between adverse biologic effects and particle composition, size, and other characteristics and their toxicity and adverse biologic effects (Tsuji et al., 2006). The toxicity of airborne nanoparticles is relatively well studied, but other routes of exposure, such as subcutaneous, intravenous and intraperitoneal administrations remain largely terra incognita.

The present study on the systemic and localized administration of LNH represents an initial evaluation of their possible *in vivo* toxicological effects of these nanoparticles, as they have great potential for application as tools for delivery of anti-tumor and anti-inflammatory drugs and genes (Tyner et al., 2004a; Tyner et al., 2004b).

The s.c., i.p. and i.v. administration of LNH did not cause pronounced

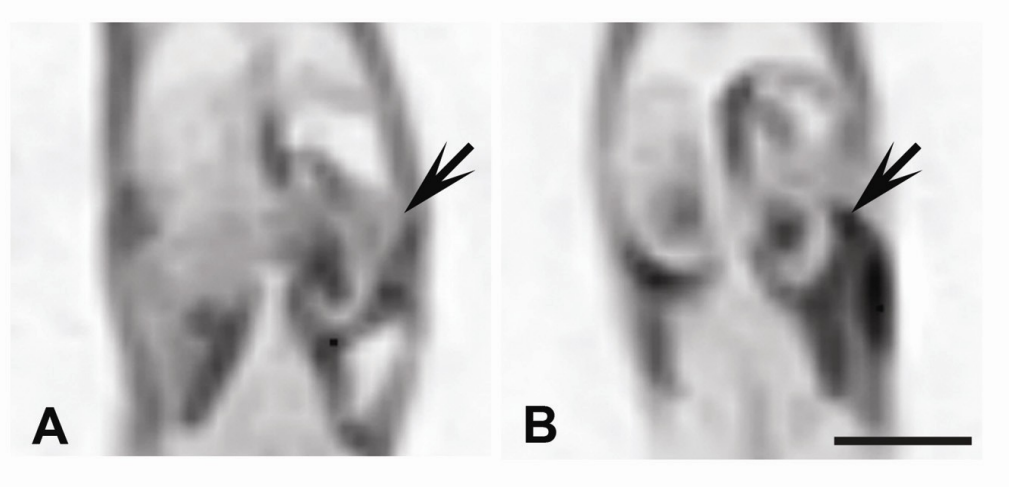

Figure 5.3 Detection of gadolinium layered nanohybrids by magnetic resonance imaging (MRI). MRI of 6-month old female mice 3 days after transoviductal intrabursal injection with vehicle solution (*A*) or gadolinium-based nanoparticles (*B*). Injected left ovaries are indicated with arrows. Increase in density indicates location of the ovary contrasted with gadolinium nanoparticles. Inverse coronal images. Top, head. Calibration bar, 1 cm.

toxicity in the FVB/N mice, as demonstrated by their high survival and lack of clinical and behavior signs. This is in accord with the decade-long good safety record of aluminum and magnesium oxides and salts as vaccine adjuvants, antacids and laxatives (Verdier et al., 2005).

In the s.c.-treated mice LNH remained close to the injection site for 21 days in cutaneous and subcutaneous tissue. The microscopic changes in the site of SC injection of LNH resemble the local reaction after administration of aluminium-containing vaccines (Valtulini et al., 2005).

In the i.p.-injected mice, no specific fluorescence was detected on the peritoneum covering liver, spleen, pancreas or kidney, as well as in the adjacent mesenteric lymph nodes and additional studies are needed to determine the fate of the LNH administered in this fashion.

After i.v. application specific nanohybrid fluorescence was observed in chronic inflammatory lesions in the lungs and in macrophages in the liver. The lesions in the lungs were comparable in principle to those of rat lung exposed to inhaled nanoparticles reported by Tsuji et al. (Tsuji et al., 2006), who established that macrophage-mediated immunological responses occurred following a transient (24-hour postexposure) neutrophil-associated inflammation. Further studies would be necessary for comprehensive examination of the uptake, metabolism and excretion of the layered nanohybrids similar to those done by Flarend et al.(Flarend et al., 1997).

The minor pathologic changes caused in lung of mice treated IV with layered nanohybrids, as compared to the control tissues speaks in favor of the relative safety for their use. It should be noted that tested doses of LNH administration far exceed those likely to be required for targeted delivery of

therapeutic compounds. Toxic properties of LNH could be further attenuated by substituting aluminum for more biologically safe metals, such as iron.

Since LNH can incorporate fluorescent molecules we used this approach to monitor LNH distribution within the body and to co-localize their presence with potential pathological lesions. After the initial experiments showed that LNH can be readily detected in tissues we extended these studies to evaluate the clinical potential of LNH as imaging and reporting enablers. Our work indicates that LNH are well tolerated both in primary OSE cell culture and OSE in situ. As compared to our previous work with adenoviral vectors (Flesken-Nikitin et al., 2003; Manor et al., 2003; Riley et al., 1996) and lipid-polycation-DNA (LPD) formulations (Nikitin et al., 1999), LNH provide efficiency exceeding and approaching those of adenoviral vectors and LPD, respectively. Importantly, LNH fluorescence was detected even 35 days after IV administration indicating a possibility of longer intracellular retention of the vector than that of LPD (up to 2 weeks) and on par with that of adenovirus.

Fluorescent photon emission-based and magnetic resonance imaging are among the most common and practical methods for biological assessment of nanoparticles. The fluorescence approach provides an inherent subcellular resolution. But biological specimens are notoriously scattering within distances ~ 50 μm so that a relatively thick specimen will appear as a blur. Generally one obtains information histologically by fixing the tissue, sectioning it to ~1 - 5 μm slices and staining those slices. Multiphoton microscopy, achieves subcellular resolution in optically thick specimens without having to section them. It works by a quantum mechanical trick in which the photoexcitation (and any phototoxicity or photobleaching) are confined to the focal plane. It enables high-resolution imaging of live mice with minimal photodamage (Zipfel

et al., 2003a; Zipfel et al., 2003b). The availability of highly specific targeting vectors with bright and specific reporters allows imaging of cell-based processes with the promise of minimizing phototoxicity to clinically acceptable levels.

MRI is currently used in clinical practice. It provides high-resolution images of anatomical structures and allows functional assessment of organs and tissues. For example, it is used for estimating the partial pressure of oxygen and determining the presence of hypoxic tumor cells (Kachur et al., 1999; Seddon et al., 2002), detection of apoptosis in tumors (Schellenberger et al., 2004), and evaluation of angiogenesis, tumor blood volume, and microvessel permeability (Kiessling et al., 2004; Marzola et al., 2003). Although the rate of image acquisition is significantly slower than photon emission-based methods, and structural resolution does not reach subcellular levels comparable to that of fluorescence-based imaging, MRI is one of the best methods for non-invasive imaging. For a comprehensive analysis, probes that can be detected by both strategies are ideal, such as the multimodal proteins described in Schellenberger et al. (Schellenberger et al., 2004).

Our current study demonstrated that layered magnesium/aluminum and magnesium/gadolinium-based nanoparticles can be successfully detected in the ovary by multiphoton and magnetic resonance imaging. Further functionalization of LNH with specific peptides and antibodies should allow imaging and monitoring ovarian and other tumors while subjecting them to selective anticancer drug delivery.

The results of the current study on biologic effects and biomedical applications of LNH demonstrate only minor toxicity and are encouraging with respect of their use as imaging enablers. Taken together with established

properties of LNH as effective drug and nucleic acid delivery vehicles, this work provides a basis for further development of LNH as multifunctional nanoparticles suitable for a broad variety of biomedical applications.

REFERENCES

Ambrogi, V., Fardella, G., Grandolini, G., Nocchetti, M., and Perioli, L. (2003). Effect of hydrotalcite-like compounds on the aqueous solubility of some poorly water-soluble drugs. J Pharm Sci *92*, 1407-1418.

Ambrogi, V., Fardella, G., Grandolini, G., and Perioli, L. (2001). Intercalation compounds of hydrotalcite-like anionic clays with anti-inflammatory agents-I. Intercalation and in vitro release of ibuprofen. Int J Pharm *220*, 23-32.

Chen, M., and von Mikecz, A. (2005). Formation of nucleoplasmic protein aggregates impairs nuclear function in response to SiO2 nanoparticles. Exp Cell Res *305*, 51-62.

Choy, J.H., Kwak, S.Y., Jeong, Y.J., and Park, J.S. (2000a). Inorganic layered double hydroxides as nonviral vectors. Angew Chem Int Ed *39*, 4042-4045.

Choy, J.H., Park, J.S., Kwak, S.Y., Jeong, Y.J., and S., H.Y. (2000b). Layered double hydroxide and gene reservoir. Mol Cryst Liq Crys *341*, 425- 429

Colvin, V.L. (2003). The potential environmental impact of engineered nanomaterials. Nature Biotechnol *21*, 1166-1170.

Donaldson, K., Aitken, R., Tran, L., Stone, V., Duffin, R., Forrest, G., and Alexander, A. (2006). Carbon nanotubes: a review of their properties in relation to pulmonary toxicology and workplace safety. Toxicol Sci *92*, 5-22.

Ferrari, M. (2005). Cancer nanotechnology: opportunities and challenges. Nat Rev Cancer *5*, 161-171.

Flarend, R.E., Hem, S.L., Whithe, J.L., Elmore, D., Suckow, M.A., and Rudy, A.C. (1997). In vivo absorbtion of aluminium-containing vaccine adjuivants using 26Al. Vaccine *15*, 12-13.

Flesken-Nikitin, A., Choi, K.C., Eng, J.P., Shmidt, E.N., and Nikitin, A.Y. (2003). Induction of carcinogenesis by concurrent inactivation of p53 and Rb1 in the mouse ovarian surface epithelium. Cancer Res *63*, 3459-3463.

Flesken-Nikitin, A., Williams, R. M., Zipfel, W. R., Webb, W. W., and Nikitin, A. Y. (2004). Use of multiphoton imaging for studying cell migration in the mouse. . Methods Mol Biol *294*, 335-346.

Hirsch, L.R., Stafford, R.J., Bankson, R.A., Sershen, S.A., Rivera, B., Price, R.E., Hazle, J.D., Halas, N.J., and West, J.L. (2003). Nanoshell-mediated

near-infrared thermal therapy of tumors under magnetic resonance guidance. Proc Natl Acad Sci U S A *100*, 13549-13554.

Holsapple, M.P., Farland, W.H., Landry, T.D., Monteiro-Riviere, N.A., Carter, J.M., Walker, N.J., and Thomas, K.V. (2005). Research strategies for safety evaluation of nanomaterials, part II: toxicological and safety evaluation of nanomaterials, current challenges and data needs. Toxicol Sci *88*, 12-17.

Hussein, M.Z.B., Sainal, Z., Yahaya, A.H., and Foo, D.W.V.F. (2002). Controlled release of a plant growth regulator, a-naphthalene acetate from the lamella of Zn-AL-layered double hydroxide nanocomposite. J Control Release *82*, 417-427.

Kachur, A.V., Dolbier, W.R., Jr., Evans, S.M., Shiue, C.Y., Shiue, G.G., Skov, K.A., Baird, I.R., James, B.R., Li, A.R., Roche, A.*, et al.* (1999). Synthesis of new hypoxia markers EF1 and [18F]-EF1. Appl Radiat Isot *51*, 643-650.

Khan, A.I., Lei, L., Norquist, A.J., and O'Hare, D. (2001). Intercalation and controlled release of pharmaceutically active compounds from a layered double hydroxide. Chem Commun *22*, 2342-2343.

Kiessling, F., Farhan, N., Lichy, M.P., Vosseler, S., Heilmann, M., Krix, M., Bohlen, P., Miller, D.W., Mueller, M.M., Semmler, W.*, et al.* (2004). Dynamic contrast-enhanced magnetic resonance imaging rapidly indicates vessel regression in human squamous cell carcinomas grown in nude mice caused by VEGF receptor 2 blockade with DC101. Neoplasia *6*, 213-223.

Kwak, S.Y., Jeiong, Y.J., Park, J.S., and Choy, J.H. (2002). Bio-LDH nanohybrids for gene therapy. Solid State Ionics *151*, 229-234.

La Van, D.A., Lynn, D.M., and Langer, R. (2002). Moving smaller in drug discovery and delivery. Nat Rev Drug Discov *1*, 77-84.

Manor, D., Shmidt, E.N., Budhu, A., Flesken-Nikitin, A., Zgola, M., Page, R., Nikitin, A.Y., and Noy, N. (2003). Mammary carcinoma suppression by cellular retinoic acid binding protein-II. Cancer Res *63*, 4426-4433.

Marzola, P., Farace, P., Calderan, L., Crescimanno, C., Lunati, E., Nicolato, E., Benati, D., Degrassi, A., Terron, A., Klapwijk, J.*, et al.* (2003). In vivo mapping of fractional plasma volume (fpv) and endothelial transfer coefficient (Kps) in solid tumors using a macromolecular contrast agent: correlation with histology and ultrastructure. Int J Cancer *104*, 462-468.

Maynard, A.D., Aitken, R.J., Butz, T., Colvin, V., Donaldson, K., Oberdorster, G., Philbert, M.A., Ryan, J., Seaton, A., Stone, V.*, et al.* (2006). Safe handling of nanotechnology. Nature *444*, 267-269.

Nikitin, A.Y., and Hamilton, T.C. (2005). Modeling ovarian cancer in the mouse. In Research Advances in Cancer, R.M. Mohan, ed. (Kerala, Global Research Network).

Nikitin, A.Y., Juárez-Pérez, M.I., Li, S., Huang, L., and Lee, W.-H. (1999). RB-mediated suppression of multiple neuroendocrine neoplasia and lung metastases in $Rb^{+/-}$ mice. Proc Natl Acad Sci USA *96*, 3916-3921.

Oberdoerster, G., Oberdoerster, E., and Oberdoerster, J. (2005). Nanotoxicology: an emerging discipline evolving from studies of ultrafine particles. Evironm Health Perspectives *113*, 823-839.

Peter, H.H., Irene, B.H., and Oleg, V.S. (2004). Nanoparticles—known and unknown health risks. J Nanobiotechnol *2*, 12.

Riley, D.J., Nikitin, A.Y., and Lee, W.-H. (1996). Adenovirus-mediated retinoblastoma gene therapy suppresses spontaneous pituitary melanotroph tumors in $Rb^{+/-}$ mice. Nature Medicine *2*, 1316-1321.

Roco, M.C. (2003). Nanotechnology: convergence with modern biology and medicine. Curr Opin Biotechnol *14*, 337-346.

Schellenberger, E.A., Sosnovik, D., Weissleder, R., and Josephson, L. (2004). Magneto/optical annexin V, a multimodal protein. Bioconjug Chem *15*, 1062-1067.

Seddon, B.M., Maxwell, R.J., Honess, D.J., Grimshaw, R., Raynaud, F., Tozer, G.M., and Workman, P. (2002). Validation of the fluorinated 2-nitroimidazole SR-4554 as a noninvasive hypoxia marker detected by magnetic resonance spectroscopy. Clin Cancer Res *8*, 2323-2335.

Service, R.F. (2004). Nanotoxicology. Nanotechnology grows up. Science *304*, 1732-1734.

Service, R.F. (2005). Nanotechnology. Calls rise for more research on toxicology of nanomaterials. Science *310*, 1609.

Stix, G. (2001). Little big science, Nanotechnology. Sci Am *285*, 32-37.

Tsuji, J.S., Maynard, A.D., Howard, P.C., James, J.T., Lam, C.W., Warheit, D.B., and Santamaria, A.B. (2006). Research strategies for safety evaluation of nanomaterials, part IV: risk assessment of nanoparticles. . Toxicol Sci *89*, 42-50.

Tyner, K.M., Roberson, M.S., Berghorn, K.A., Li, L., Gilmour Jr., R.F., Batt, C.A., and Giannelis, E.P. (2004a). Intercalation, Delivery, and Expression of

the Gene Encoding Green Fluorescence Protein. J Control Release *100*, 399-409.

Tyner, K.M., Schiffman, S.R., and Giannelis, E.P. (2004b). Nanobiohybrids as delivery vehicles for camptothecin. J Control Release *95*, 501-514.

Valtulini, S., Macchi, C., Ballanti, P., Cherel, Y., Laval, A., Theaker, J.M., Bak, M., Ferretti, E., and Morvan, H. (2005). Aluminium hydroxide-induced granulomas in pigs. . Vaccine *23*, 3999-4004.

Verdier, F., Burnett, R., Michelet-Habchi, C., Moretto, P., Fievet-Groyne, F., and Sauzeat, E. (2005). Aluminium assay and evaluation of the local reaction at several time points after intramuscular administration of aluminium containing vaccines in the Cynomolgus monkey. Vaccine *23*, 1359-1367.

Vijayanathan, V., Thomas, T., and Thomas, T.J. (2002). Nanoparticles and the development of DNA delivery vehicles for gene therapy. Biochemistry *41*, 14085-14094.

Wagner, V., Dullaart, A., Bock, A.-K., and Zweck, A. (2006). The emerging nanomedicine landscape. Nat Biotech *24*, 1211-1217.

Zhou, Z., Flesken-Nikitin, A., Corney, D.C., Wang, W., Goodrich, D.W., Roy-Burman, P., and Nikitin, A.Y. (2006). Synergy of p53 and Rb Deficiency in a Conditional Mouse Model for Metastatic Prostate Cancer. Cancer Res *66*, 7889-7898.

Zipfel, W.R., Williams, R.M., Christie, R., Nikitin, A.Y., Hyman, B.T., and Webb, W.W. (2003a). Live tissue intrinsic emission microscopy using multiphoton-excited native fluorescence and second harmonic generation. Proc Natl Acad Sci USA *100*, 7075-7080.

Zipfel, W.R., Williams, R.M., and Webb, W.W. (2003b). Nonlinear magic: multiphoton microscopy in the biosciences. Nature Biotechnol *21*, 1369-1377.

CHAPTER 6

THE HILUM REGION IS A PUTATIVE STEM CELL NICHE FOR THE OVARIAN SURFACE EPITHELIUM

6.1 Abstract

The ovarian surface epithelium (OSE) is formed by a monolayer of squamous or cuboidal cells surrounding the ovary. During ovulation the OSE is ruptured and its loss requires a constant supply of new epithelial cells. Recently putative ovarian surface epithelium (OSE) stem/progenitor cells (OSE-SC) cells have been identified based on their slow proliferation in label retention assays. However, the self-renewal ability of these cells remains unknown. Furthermore, it is unknown if OSE-SC occupy any anatomically defined areas. By using a stem cell marker, aldehyde dehydrogenase (ALDH) 1, we have been able to identify an OSE subpopulation which efficiently forms clonal ovaspheres. These ALDH1$^+$ cells are slowly cycling *in vivo* and are mainly located in the hilum region of the mouse ovary, the transitional area between OSE, mesothelium and oviductal epithelium. Hilum OSE cells expressed the stem cell markers CK6, CD44, Notch 1, Notch2, CD133, and p63 as well as epithelial markers calretinin, and PAX8. Importantly, cells isolated from the hilum display increased proliferative potential and extended self-renewal properties in serial sphere generation assay. We propose a model of OSE homeostasis in which OSE-SC cells are concentrated in the hilum region of the ovary. Identification of a putative OSE-SC stem cell niche may have

important implications for understanding epithelial ovarian cancer (EOC) pathogenesis.

6.2 Introduction

Approximately 90% of ovarian cancers are of epithelial origin (Auersperg et al., 2001; Cho and Shih Ie, 2009). Due largely to asymptomatic development, the majority of patients are diagnosed with having an advanced stage of the disease, by which time treatment options are of limited therapeutic value and accordingly, the 5-year survival is below 30% (Jemal et al., 2010). Pathological observations of human EOC, as well as experimental induction of EOC (Auersperg et al., 2001; Scully et al., 1999) in mice (Clark-Knowles et al., 2007; Dinulescu et al., 2005; Flesken-Nikitin et al., 2003; Orsulic et al., 2002; Wu et al., 2007), indicate that the majority of EOC arises from the OSE, a monolayer of squamous or cuboidal cells that line the ovary. Additionally some EOC may derive from the epithelium of the Fallopian tube fimbriae (Dubeau et al., 2008; Medeiros et al., 2006).

Unlike the majority of epithelial tissues, presence of OSC remains insufficiently established and no unique markers have been identified. Recently, using pulse-chase experiments with BrdU/IdU (5-bromo-2'-deoxyuridine/5-iodo-2'deoxyuridine) and tetracycline-regulated (doxycycline responsive) tetO-H2B-GFP transgenic mice, Szotek and colleagues (Szotek et al., 2008) have identified the existence of ovarian epithelial label retaining cells (LRC). This putative somatic stem/progenitor cell population exhibits properties of quiescence, functional response to estrous cycling by proliferation in the mouse, enhanced colony forming ability in tissue culture

and ability for exclusion of the DNA-binding dye Hoechst 33342 (Szotek et al., 2008). However, long-term self-renewal, the key feature of the stem cells, has not been tested. Furthermore, it is unknown if OSE-SC occupy anatomically defined areas, similar to those in other organs, such as the intestine, hair follicle, cornea and prostate (Blanpain et al., 2007; Nikitin et al., 2009).

Recent reports identified a detoxifying enzyme ALDH1 as a useful marker of stem/progenitor cells in a number of cell lineages, such as mammary (Ginestier et al., 2007), prostate (Burger et al., 2009), colon (Huang et al., 2009), hematopoietic (Storms et al., 1999), neural (Corti et al., 2006), and mesenchymal (Gentry et al., 2007). Strikingly, enzymatic activity of ALDH1 correlates well with its expression, thereby allowing assessment of ALDH1 function by conversion of ALDH1 substrate into the fluorescent product (ALDEFLUOR reaction), as well as by immunodetection, such as immunohistochemistry (IHC) and western blotting (Deng et al., 2010). Moreover, it has been reported that about 7.6 % of OSE cells express ALDH1 (Deng et al., 2010). However, it is unknown if such cells have any stem cell-related properties.

In the present study we combine a classic approach, the identification of replication quiescent BrdU (5-bromo-2'-deoxyuridine) label-retaining cells (LRCs), with the detection of ALDH1 and *ex vivo* functional characterization of OSE-SCs in three dimensional (3D) clonogenic sphere formation assays. Based on these assays we demonstrate that $ALDH1^+$ cells are slowly cycling *in vivo* and are mainly located in the hilum area of the mouse ovary. Centering on the characterization of hilum OSE versus OSE covering other regions we report that hilum cells express in higher frequency the stem cell markers CK6,

CD44, CD133, Notch1, Notch2 and p63, as well as epithelial markers calretinin, and PAX8.

6.3 Materials and Methods

Experimental Animals. FVB/NCr mice were purchased from NCI-Frederick Animal Production Program, Charles River Laboratories, Inc., Frederick, Maryland or breed in house. Wild type mice were breed in house. The *ß*-actin GFP [C57BL/6-Tg(CAG-EGFP01Osb/J], and *ß*-actin DsRed mice [B6.Cg-Tg(ACTB-DsRed*MST)1Nagy/J] were purchased from The Jackson Laboratory (Bar Harbor, ME). All of the mice were maintained identically, following recommendations of the Institutional Laboratory Animal Use and Care Committee.

BrdU pulse-chase experiments were performed three times with postpubertal 6 to 7 weeks old virgin FVB mice. Animals were injected daily with 250 µl of BrdU (5-bromo-2'deoxyuridine, Sigma, 1mg/ml) intraperitonially for 10 days (pulse) and euthanized after the pulse and at monthly intervals for 4 months (Fig.6.3).

Primary Culture of Hilum and Ovary parts. Individual hilum and anterior ovary parts were dissected under dissection microscope from 6 to 8 weeks old virgin FVB mice (Fig. 6.6*A*), minced in a drop of PBS with 25G needles, transferred to 100 µl digestion-buffer: 4 mg/ml Collagenase-Dispase(Roche) supplemented with 30 mg/ml bovine albumin (Sigma) and 1 µl DNaseI (1 mg/ml, Sigma) , incubated and allowed to adhere for 24 hr as described onto 24 well-plates in complete OSE Stem Cell Medium (OSE-SCM), DMEM/F12

(Ham's) medium containing 5% fetal bovine serum, 4 mM L-glutamine, 1 mM sodium pyruvate, 10 ng/ml epidermal growth factor, 500 ng/ml hydrocortisone, 5 µg/ml insulin, 5 µg/ml transferring, 5 ng/ml sodium selenite, 0.1 mM MEM non-essential amino acids, 10^{-4} M ß-mercaptoethanol, 10^3 u/ml leukemia inhibitory factor (Millipore).

Cellular proliferation assay. Primary hilum/ovary part cells, passage 0, were harvested, reseeded in triplicates at 1 x 10^4 cells/3.5cm dish in OSE-SCM, grown for three days, then stained with Giemsa solution, air-dried and images were taken (Fig. 6.6*B*). Total area analyzed was 4.92 cm^2.

Cultivation of OSE-spheres. Cell populations from 2 x 10^4 to 1 x 10^5 cells/assay were collected in 0.5 ml OSE-SCM, centrifuged and pellets were suspended in 1:1 Geltrex/OSE-SCM (Invitrogen) in a total volume of 120 µl. Following a modified protocol of Lawson et al(Lawson et al., 2007) each cell population was plated around the rim of a well of a 12 well plate and allowed to solidify for 25 minutes at 37°C in a 5% CO2 incubator before adding 1.5 ml OSE-SCM. Spheres were grown from 7 to 12 days. For passaging of spheres, media was aspirated and Geltrex was digested by incubation in 750 µl digestion-buffer for 1 h, at 37°C, during incubation spheres were suspended 2 – 3 times manually by pipetting using a blue 1 ml tip. Digested cultures were pelleted and incubated in 0.3 ml 0.25% Trypsin/EDTA for 10 min at 37°C, cells were suspended and the enzyme reaction was stopped by adding 4 ml OSE-SCM. Cells were harvested and counted by hemocytometer and replated at different densities as described above.

For analysis the following calculation was applied: OSE-CFC (%) = # of OSE-Clones x 100 / # of input cells. Corresponding OSE-Clone Forming Units in the hilum region: OSE-CFU = # of input cells / # of OSE-Clones formed, were determined (Table 6.6*E*).

Cytospin preparations. Cells suspended at concentrations from 0.5 x 10^4 to 1 x 10^5 / 100 µl OSE-SCM / slide were spin down for 5 min. at speed 13 in a CytoFuge2 (StatSpin Inc.), immersed in PBS for 4 minutes, fixed with 4% paraformaldehyde for 30 minutes on ice, rinsed with PBS and stored in PBS until immunofluorescence analysis.

Immunohistochemistry, Immunofluorescence, and Image Quantitative Analysis. Immunohistochemical analysis of paraffin sections of paraformaldehyde-fixed tissue was performed by a modified ABC technique (Nikitin and Lee, 1996; Zhou et al., 2006). The antibodies to calretinin (Abcam, Cambridge, MA, 1:50),E-Cadherin (Cell Signaling, Danvers, MA, 1:10)PAX8 (Abcam, 1:1000), cIAP1 (Abcam 1:300), CK5 (Covance, Berkeley, CA, USA, 1:1000), p63 (Santa Cruz, Santa Cruz, CA, 1:200), BrdU (Abcam; 1:100) ALDH1A1 (Abcam; 1:100), were incubated with deparaffinized sections for 1 h at room temperature. Ten-min treatment with 4N hydrochloric acid and 10 min boiling in 10 mM citric buffer was used for antigen retrieval for detection of BrdU. For immunofluorescence analysis, deparaffinized sections or cells fixed in 4% paraformaldehyde were incubated with the antibodies to BrdU or ALDH1A1 as above, CK6 (Covance, 1:300), CD44 (Santa Cruz Biotechnology; 1:25), CD133 (Miltenyi Biotec; 1:50), Notch1 (bTAN20; 1:25, Developmental Studies Hybridoma Bank), Notch2 (C651.6DbHN; 1:25). For Runx1 enzymatic detection of bacterial ß-galactosidase was performed as previously described

(Flesken-Nikitin et al., 2003). Samples were analyzed under an Axioskop 2 (Zeiss) fluorescence microscope equipped with a CCD camera described in (Zhou et al., 2007). Digital images were computer processed with Adobe Photoshop 7.0. For the quantitative analysis of IHC and IF experiments performed with cytospin samples (Fig. 6.*5A-G*), the ImageJ image-analysis software (W. Rasband, National Institutes of Health) was used.

Statistical Analyses. All statistical analyses in this study were done using InStat 3.06 and Prism 5.01 software (GraphPad, Inc., San Diego, CA) as described previously (Zhou et al., 2006).

6.4 Results

6.4.1 Generated OSE-spheres are monoclonal. To initiate assessment of putative OSE-SC we have established OSE-sphere formation rim assay suitable for evaluation of normal OSE cells. See for further details Materials and Methods. In these assays single cell suspension of OSE cells were placed in Geltrex/OSE-SCM around the rim of a well of a 12 well plate and grown for 7-12 days. To confirm single cell derivation of spheres, cell suspensions of primary OSE were derived from of Tg*ß*-actin EGFP or *ß*-actin DsRed mice and mixed at various ratios. The resulting spheres were exclusively monochromatic, indicating their clonal origin (Fig. 6.1*A, B*).

6.4.2 ALDH activity is enriched in an OSE sub-population. To assess if ALDH activity can be used to enrich for cells with functional properties of stem/progenitor cells, primary OSE cell populations were separated into

Figure 6.1 Formation of clongenic spheres and self-renewal properties by a subset of OSE cells. Single cell suspensions of the OSE were prepared from Tg*ß*-actin EGFP (EGJ) or *ß*-actin DsRed (DsR) mice and mixed in various ratios (4+1 and 1+4). All individual spheres were exclusively monochromatic, indicating clonal origin. (*A*) Phase contrast (left) and fluorescence (right) images of DsRed (red) and EGFP (green) positive OSE-spheres (arrows). Bar, *A* - *B*, 50 µm. (*B*) Quantitative assessments of fluorescent spheres grown for 10 to 12 days. Number (mean± SD) of EGFP positive (EGFP) and DSRed positive (DsRed) spheres in individual groups: "EGFP only": EGFP 163.5 ± 25.9, *n* = 6, DsRed 0; "4 + 1": EGFP 169.7 ± 29.8, *n* = 3, DsRed 44.3 ± 14.2, *n* = 3; "1+4"; EGFP 46.0 ± 19.3, *n* = 3, DsRed 208.7 ± 69.0, *n* = 3: "DsRed": EGFP 0, DsRed 273.0 ± 62.0, *n* = 3. The table indicates the number of cells seeded. (*C*) FACS plot depicturing gating of $ALDH^-$ (GFP low) and $ALDH^+$ (GFP high) cells. (*D*). Efficiency of sphere formation by $ALDH1^+$ and $ALDH1^-$ OSE cells (*P* = 0.0001) at second generation (G2). (*E*) Growth of $ALDH1^+$ and $ALDH1^-$ cells in OSE-sphere assays.

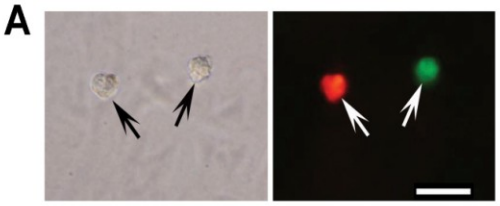

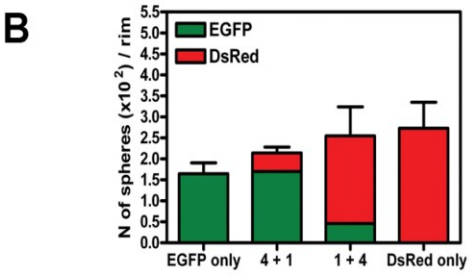

EGFP cells, n	10 000	8 000	2 000	-
DsR cells, n	-	2 000	8 000	10 000

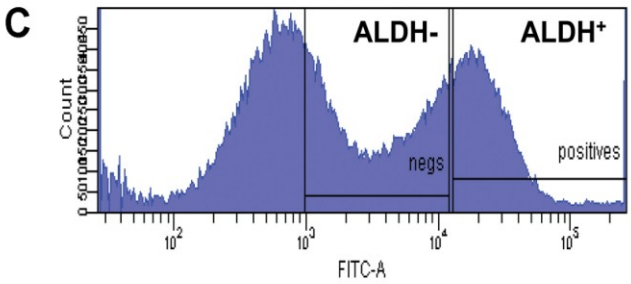

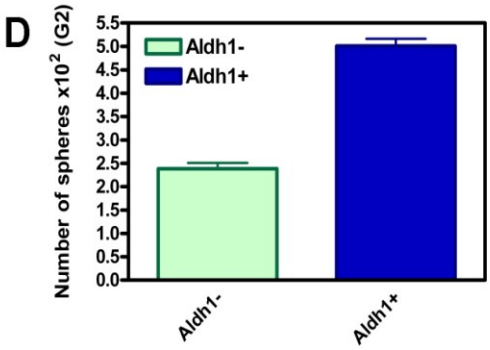

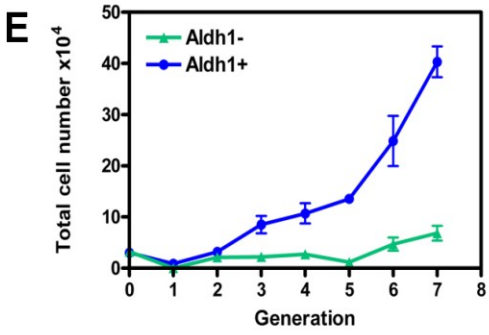

ALDH1 high ($ALDH1^+$) and ALDH1 low ($ALDH1^-$) cells according to their level of ALDEFLUOR fluorescence by fluorescence activated cell sorting (FACS, Fig. 6.1*C*) and subjected to OSE-sphere formation assays. After two rounds of sphere generation (G2) $ALDH1^+$ cells formed clonogenic OSE spheres at significantly higher frequency and continued to show enhanced growth as compared to those of $ALDH1^-$ cells (Fig. 6.1*D*). Indicating self-renewal properties of OSE-sphere forming cells, spheres were formed from a single cell suspension in at least up to 7 consecutive rounds of sphere dissociation/generation (Fig. 6.1*E*).

6.4.3 ALDH1 is highly expressed in OSE located in the hilum area of the mouse ovary. Towards identification of OSE-SC in the mouse ovary by regions we performed immunohistochemical analysis for ALDH1 of ovarian tissues from 3, 6 and 8 weeks old virgin FVB mice. Since the ovary has well defined anatomical regions, we have evaluated expression of ALDH1 in the OSE covering the corpus luteum, the distal-, antral and the hilum region. Strikingly, cells with high ALDH1 activity have been predominantly detected in the hilum region (Fig. 6.2).

6.4.4 BrdU label retaining cells (LRCs) co-localize with $ALDH1^+$ cells. To test if slow proliferating cells are preferentially located in the hilum, pulse chase experiments were performed by injecting 6 – 7 weeks old virgin FVB mice for 10 days with a BrdU solution (Fig. 6.3) followed by detection of LRCs immediately after the pulse and monthly for up to 4 months. Ovarian regional analysis revealed that the hilum contains the highest percent of slow-cycling OSE cells by 3 months after BrdU pulse (Fig. 6.4*A*). Consistently with these

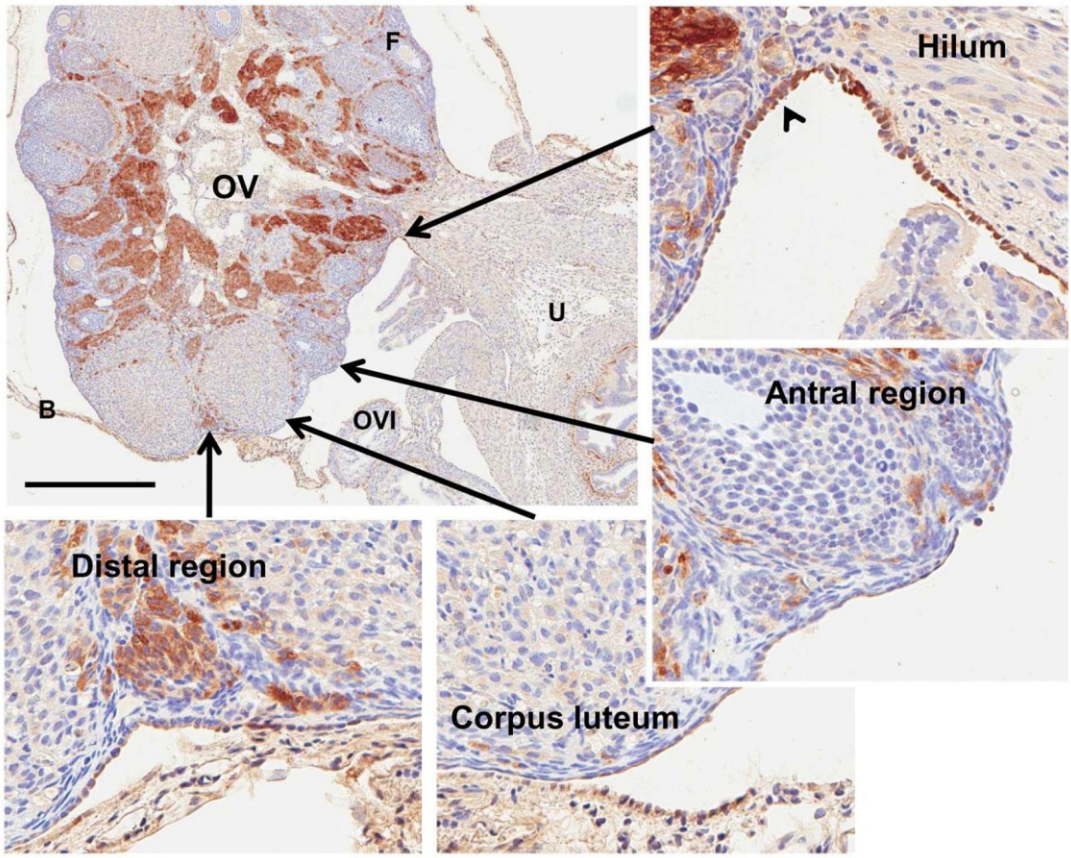

Figure 6.2 Detection of ALDH1 in the OSE of different areas of the ovary. ALDH1 (brown color) is preferentially expressed in the OSE of the hilum region (Hilum, arrowhead) as compared to the antral region, corpus luteum or distal region. Arrows indicate location of the corresponding regions in the mouse ovary. B, bursa; F, follicle; OV, ovary; OVI, oviduct; U, uterus. Paraffin ovarian sections from 6 weeks old mouse. ABC Elite method, hematoxylin counterstaining. Bar, upper left image, 500 *μ*m; all other images, 5000 *μ*m.

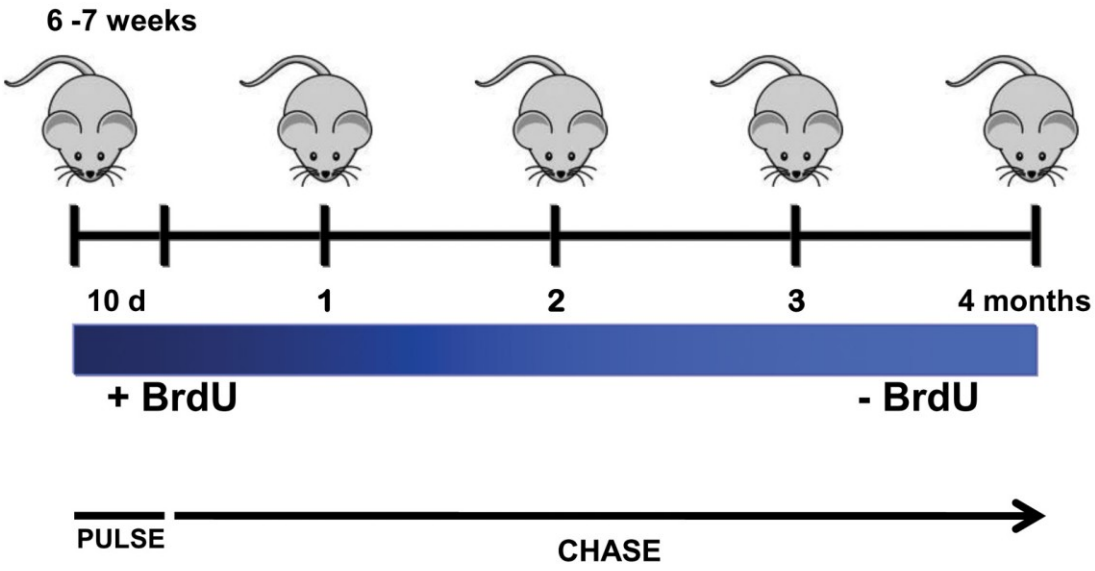

Figure 6.3 Schematic of BrdU pulse-chase timeline. Animals were injected continuously with BrdU for 10 days (pulse) and their ovaries were collected after the pulse and at monthly intervals for 4 months for analysis.

Figure 6.4 Identification of BrdU label-retaining cells (LRC) and LRCs/ALDH1 co-localization. (*A*) Quantification of LRCs in the corpus luteum (CL), antral, distal and hilum regions (n = 4). At 3 months after BrdU pulse hilum versus CL, $P < 0.001$; versus antral region, $P = 0.0005$; versus distal region, $P < 0.0001$). (*B*-*E*) Detection of BrdU LRCs (*B*, green, arrow), ALDH1 (*E*, red, arrow) and overlay (*D*, orange, arrow) after 3 months of chase in the hilum. (*C*, counterstaining with DAPI, blue). Bar, B - E, 50 μm.

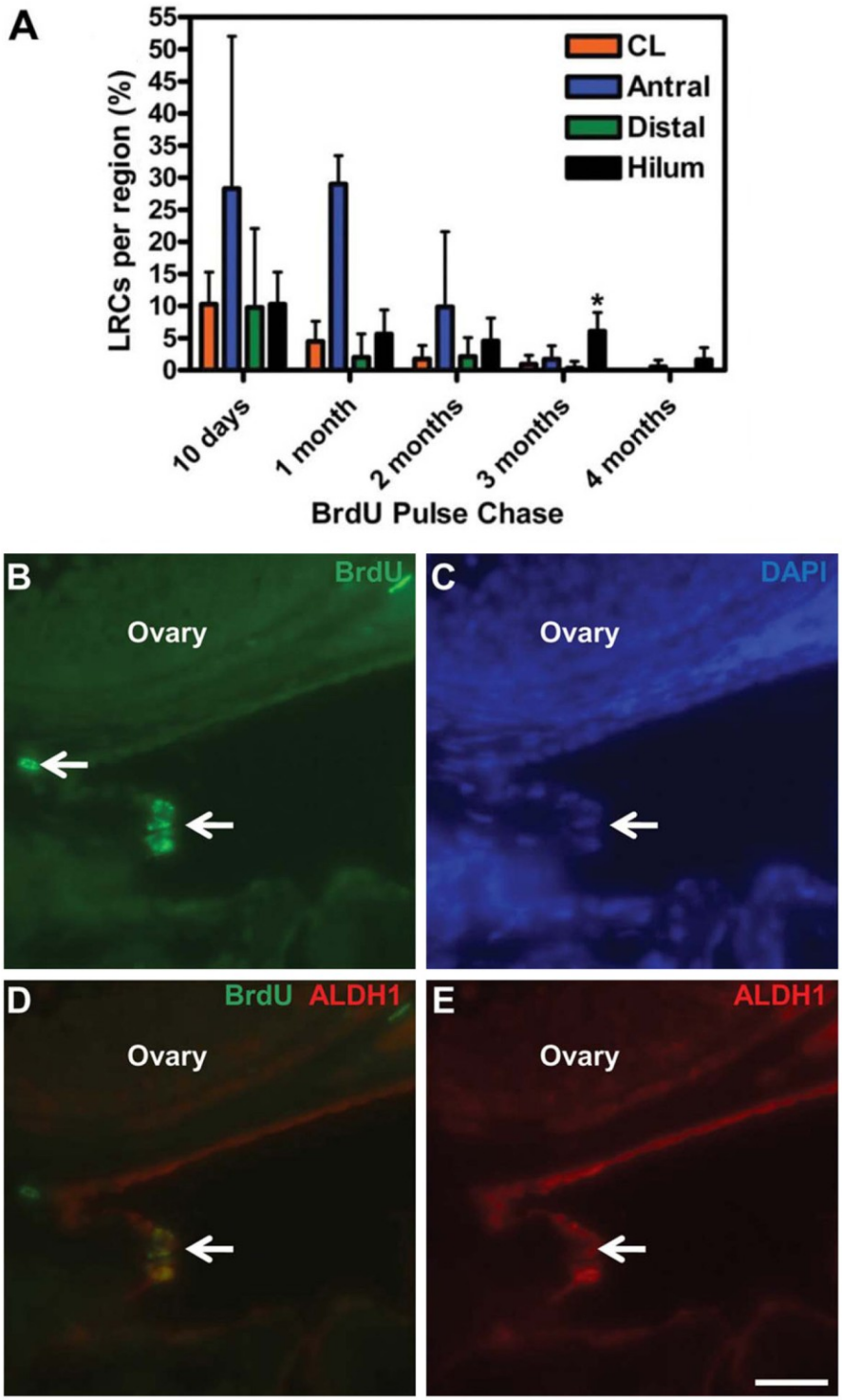
A
LRCs per region (%)
55
50
45
40
35
30
25
20
15
10
5
0
CL
Antral
Distal
Hilum
*
10 days
1 month
2 months
3 months
4 months
BrdU Pulse Chase
B
BrdU
Ovary
C
DAPI
Ovary
D
BrdU ALDH1
Ovary
E
ALDH1
Ovary

findings, double-immunofluorescence of LRCs in the OSE demonstrated that most of them expressed ALDH1 (Fig. 6.4*B-E*).

6.4.5 Hilum cells express a number of stem cell markers. For phenotypical characterization of OSE cells isolated from different region of the ovary and grown in sphere assays, cytospin preparations were used for immunostaining for a panel of markers (Fig. 6.5, *A* - *F*). As compared to the rest of the ovary, cytospins prepared form hilum-derived OSE-spheres had significantly fractions of cells positive for stem cell markers ALDH1, CK6, CD44 and Notch2. Importantly, according to double immunofluorescence staining, the hilum-derived set had significantly higher number cells co-expressing ALDH1 and CD44, as well as ALDH1 and Notch2, as compared to OSE cells derived from other ovary regions. Higher percentages of CD133, Notch1, $ALDH1^+/CD133^+$ and $ALDH1^+/Notch1^+$ expressing hilum cells were also found, compared to the ovary part cells, although the *P* values were considered not quite significant (Fig. 6.5*G*).

To perform semiquantitative expression analysis *in situ*, a panel of epithelium and stem cell markers E-Cadherin, calretinin, PAX8 and stem cell markers cIAP1, CK5, CK6, CD44, CD133, GATA3, Notch1, Notch2, p63, ABCG2/BCRP and Runx1 were tested for their expression levels in the OSE and oviductal epithelium *in situ*. Hilum OSE stained positively for calretinin, Pax8, ABCG2/BCRP, CD44, CD133, CK6, Notch1 and p63 (Fig. 6.5*H*). The oviductal epithelium but not OSE stained positive for E-Cadherin. The oviductal epithelium also expressed, albeit weakly and with preferential staining of cilia, calretinin, as well as PAX8 and CD44. (Fig. 6.5*H*). Staining results for markers cIAP1, CK5, GATA3 and Runx1 were negative in the hilum

Figure 6.5 Functional characterization of primary hilum OSE versus rest of the ovary OSE. (*A*-*F*) ALDH1 detection in cytospin preparations of OSE cells grown in sphere assays at sphere generation 3. Immunofluorescence with (*A*, *B*) and without (*C*) anti-ALDH1 antibody and DAPI counterstaining (*D, E, F*) of OSE cells from the hilum (*A, D, C, F*) and the rest of the ovary (*B, E*). Bar, all images, 50 *μ*m. (*G*) Quantitative assessment of stem cell marker expression in the OSE cells prepared as in (*A*-*F*). Percent of positive cells from the hilum versus the rest of the ovary (ovary): $CK6^+$, $P = 0.0101$, $ALDH1^+$, $P = 0.0037$, $CD44^+$, $P = 0.0042$, $ALDH1^+/CD44^+$, $P = 0.083$, $CD133^+$, $P = 0.0983$, $ALDH1^+/CD133^+$, $P = 0.25$, $Notch1^+$, $P = 0.6913$, $ALDH1^+/Notch1^+$, $P = 0.1188$, $Notch2^+$, $P = 0.0109$, $ALDH1^+/Notch2^+$, $P = 0.0094$. RU, relative units. (*H*) Immunodetection of epithelial (Calretinin and PAX8), and stem cell (ABCG2, CD44, CK6, Notch1, p63 and CD133) markers. Paraffin ovarian sections from 6 - 8 weeks old mice. Immunofluorescence (CD133) or ABC Elite immunoperoxidase (all other images). Counterstaining with methyl green (calretinin, PAX8, p63); hematoxylin (ABCG2, CD55, CK6 and Notch1) or DAPI (CD133). Arrows indicate positive cells; arrowheads indicate negative cells; OV, ovary; OVI, oviduct. Bar for all images, 50 *μ*m.

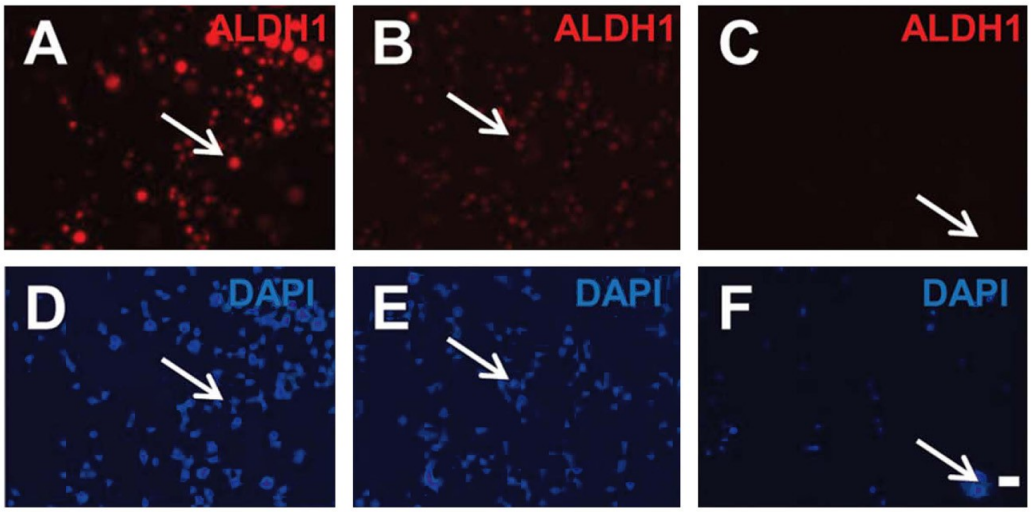
A
ALDH1
B
ALDH1
C
ALDH1
D
DAPI
E
DAPI
F
DAPI

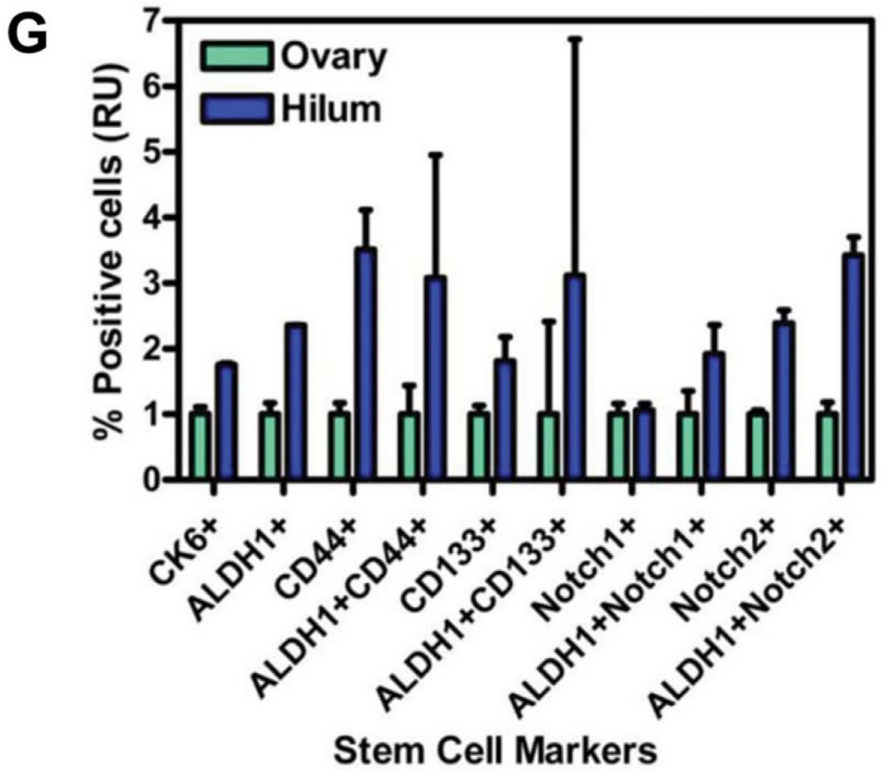
G
Ovary
Hilum
% Positive cells (RU)
0
1
2
3
4
5
6
7
CK6+
ALDH1+
CD44+
ALDH1+CD44+
CD133+
ALDH1+CD133+
Notch1+
ALDH1+Notch1+
Notch2+
ALDH1+Notch2+
Stem Cell Markers

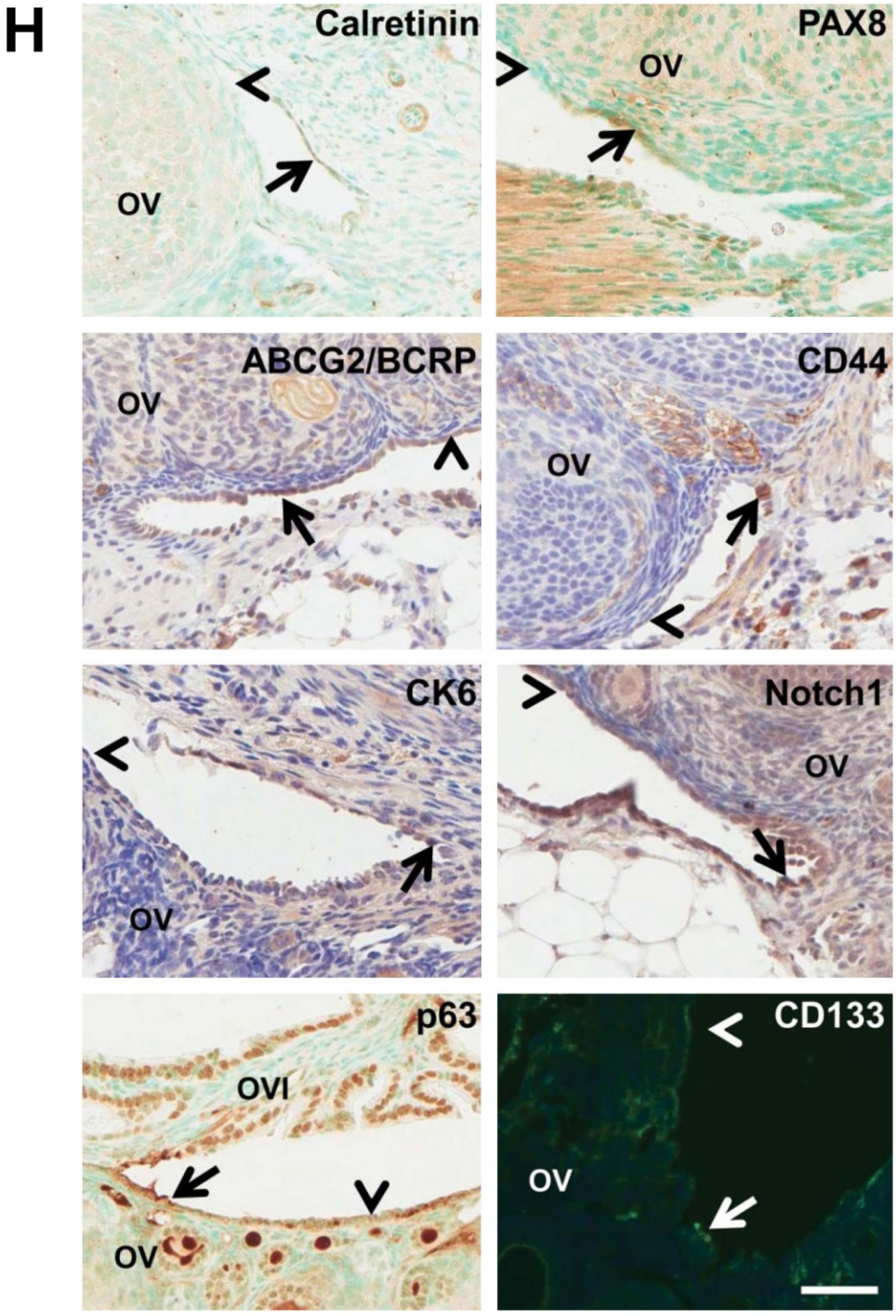
H
Calretinin
OV
PAX8
OV
ABCG2/BCRP
OV
CD44
OV
CK6
OV
Notch1
OV
p63
OVI
OV
CD133
OV

region. In addition to the hilum, p63 expression was detected in other regions of the ovary and was highly positive throughout the oviduct (Fig. 6.5*H*). In addition to the hilum, CD133 expression was detected in some cells of other ovarian regions.

6.4.6 Hilum OSE cells have a greater ex vivo proliferative and self-renewal capacity compared to other regions of the ovary. Slow-cycling quiescent stem cells have an extensive proliferation capacity (Barrandon and Green, 1987; Tsujimura et al., 2002). Therefore we assessed the growth potential of OSE cells isolated from hilum (posterior) and opposite ovary part (anterior) regions of the ovary (Fig. 6.6*A*). After three days of primary culture hilum OSE cells formed significantly more large colonies (over ≥ 20 cells) than OSE from the anterior region (Fig. 6.6, *B-C*). Notably, starting at generation two, hilum OSE cells developed conspicuous large spheres (over 77 *μ*m in diameter). In contrast, cultures of anterior ovary part regions formed such large spheres clones very rarely (Fig. 6.6, *D-F*).

6.5 Discussion

6.5.1 Development of approaches to study functions of OSE-SC. Colony forming assays, such as e.g. clonogenic sphere formation, were developed for *ex vivo* functional characterization of stem cell populations in many tissues, such as the corneal epithelium (Barrandon and Green, 1987; Pellegrini et al., 1999), neural tissues (Reynolds and Weiss, 1996), breast (Pece et al., 2010), and normal human ovarian surface epithelial cells (Jackson et al., 2009; Kwong et al., 2009). Sphere formation has been also successfully used for

Figure 6.6 The proliferative capacity and self-renewal of the hilum OSE. (*A*-*E*) Schematic of the hilum and the anterior (ovary part) regions used for isolation of OSE cells under a dissection microscope (*A*). AN, antral follicle; BU, bursa; CL, corpus luteum; F, follicle; OV, ovary; OVI, oviduct; U, uterus. (*B*) Colony formation by OSE cells isolated from the hilum (left) or the ovary part (right) images of Giemsa stained colonies (arrows). (*C*) Quantitative analysis formation of large colonies (≥ 20 cells) formed by OSE cells from the hilum (mean ± SD; 42.7 ± 12.8, n = 6; two independent cultures) and the ovary part (11.4 ± 5.68; n = 8; three independent cultures). Two tail $P < 0.0001$. (*D, E*) Hilum OSE sub-population develops conspicuous large spheres demonstrating greater *ex vivo* self-renewal potential compared to OSE cells of the anterior ovary region. (*D*) Largest (bottom image, 199 *μ*m) and smallest (top image, 77 *μ*m, arrow) sizes of spheres at generation three. (*D*) Phase contrast. (*E, F*) Frequency of OSE-sphere forming cells (OSE-CFC, %) and OSE-CFU for 7 consecutive generations (dissociation/clonal formation) in representative experiment. Bar, *A*, 5 *μ*m, *B*, 12.5 *μ*m; *D*, 50 *μ*m.

A

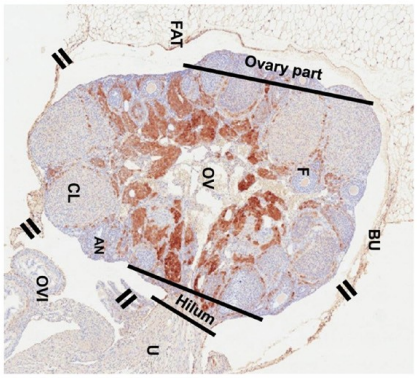

B

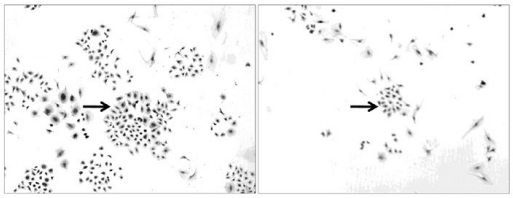

C

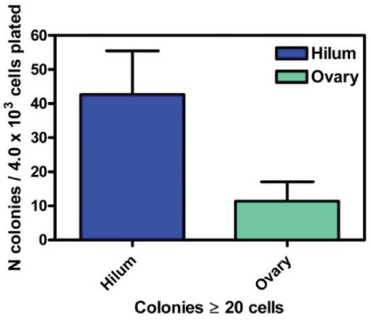

D

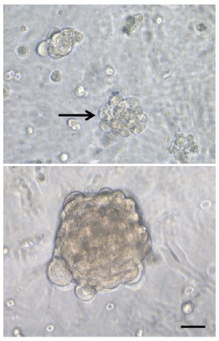

E

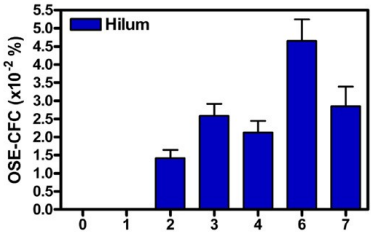

F

Generation		1	2	3	4	6	7
Hilum	Cell number	NA	1 x 10^5	1x10^5	1x10^5	0.59x10^5	1.18x10^5
	OSE-Clones	NA	14.2 (n=5)	25.8 (n=6)	21.3 (n=4)	27.5 (n=2)	29.0 (n=3)
	OSE-CFC (%)	NA	0.014	0.026	0.021	0.047	0.026
	OSE-CFU	NA	1/7468	1/3913	1/4759	1/2153	1/3511
Ovary part	Cell number	NA	1x10^5	1x10^5	1x10^5	0.12x10^5	0.25x10^5
	OSE-Clones	NA	0.2 (n=5)	0.0 (n=3)	0.0 (n=1)	0.0 (n=1)	0.0 (n=1)
	OSE-CFC (%)	NA	0.0002	0	0	0	0
	OSE-CFU	NA	1/500000	NA	NA	NA	NA

studies of ovarian cancer stem cells (Alvero et al., 2009; Zhang et al., 2008). After testing of several approaches, we have successfully adapted and modified a prostate sphere-forming assay (Lawson et al., 2007) for this study.

Long-term label retention assay take advantage of the slow-cycling nature of SC. In this method tissues are pulsed with ^{3}H-thymidine (Cotsarelis et al., 1989), BrdU (Tsujimura et al., 2002), or histone2B-green fluorescent protein (Tumbar et al., 2004). A chase period follows, allowing the identification of fast dividing (transit-amplifying) SC progeny over slow-cycling resident stem cells. Utilizing this approach combined with clonal cell culture analysis, corneal epithelial stem cells of the eye were found to reside in the limbus region, leading to clinically successful development of lens regeneration approaches curing blindness (Ezhkova et al., 2009; Rama et al., 2010). Label retention assays also identified stem cell compartments of other tissues and organs, such as the bulge area of the hair follicle (Oshima et al., 2001; Taylor et al., 2000), the terminal end bud and duct of the mouse mammary gland (Kenney et al., 2001), the renal papilla of the kidney SC reservoir (Oliver et al., 2004) and the proximal part of the prostatic ducts (Tsujimura et al., 2002).

6.5.2 Identification of putative niche for OSE-SC. Stem cell biology requires a protective microenvironment known as the stem niche. Niche components nurture and shield SC from unwanted stimuli and/or initiate required differentiation (Fuchs et al., 2004; Hsu et al., 2011; Jones and Wagers, 2008). Anatomical niche locations have been defined for several organs. A narrow transitional zone between the cornea and the bulbar conjunctiva, the limbus region, shelters corneal epithelial stem cells (Pellegrini et al., 1999; Schermer

et al., 1986). Mouse prostate epithelial stem cells reside in the proximal region of mouse prostatic ducts, near their connection to the urethra (Burger et al., 2005; Tsujimura et al., 2002; Zhou et al., 2007). Putative intestinal stem cells are located in a narrow band near the base of the intestinal crypt (Potten and Loeffler, 1990). The hair-follicle bulge serves as niche for hair follicle epidermal stem cells (Alonso and Fuchs, 2003). Stem cells of the mammary gland inhabit the terminal end bud at the end of the mammary duct (Hennighausen and Robinson, 2005). These examples demonstrate preferred niche locations for different tissues structures. However, notably, all are closely located to nerves and vessels, elementary components to support stem cell nourishment and some of them, such as corneal and prostate niches are at the junction between two tissues or organs.

Utilizing FACS we demonstrate ALDH1 activity can be used to enrich for OSE cells with functional properties of stem/progenitor cells. These sub set of cells revealed self-renewal properties in clonogenic OSE sphere forming assays and were slow cycling in label retaining assays. Strikingly, we detected $ALDH1^{+}$ OSE cells predominantly in the hilum region of the ovary. This region represents point where nerves and vessels enter the ovary and is covered by the epithelium representing transition between OSE, mesothelium and oviductal epithelium.

In 1932 Butcher et al. (Butcher and College, 1932), reported that the greatest growth activity of OSE (aka, germinal epithelium) induced by ovulation occurred near the hilum of the rat ovary. Increased OSE proliferation was also observed in the hilum region of mice and rats after local injection of estrogen (Stein and Allen, 1942). It was also observed that in adult mice, the OSE covering the posterior part of the ovary, close to the oviduct,

showed little mitotic activity (Bullough et al., 1942). Although none of these early reports proposed existence of stem cell compartment in the hilum, their findings are very consistent with our results showing location of slow-cycling, yet with high growth potential, cells in this region.

Cell replacement in tissue homeostasis requires stem cells to execute different programs of terminal differentiation. Stimuli send out from the niche instruct stem cells to selectively adopt a particular cell lineages. The Notch signaling pathway controls selective cell-fate determination in various tissues .(Artavanis-Tsakonas et al., 1999). We detected significantly higher frequency of Notch2 and ALDH1^{+}/Notch2^{+} expressing cells in primary hilum primary cultures compared to ovary part cultures. Although we detected frequent Notch1 positive cells in the hilum region on paraffin sections. Notch signaling regulates lineages determination of epithelial stem cells of the intestine, skin and mammary gland (Blanpain et al., 2007). The SC marker CD44 has been demonstrated to be important in stem cell niches (Haylock and Nilsson, 2006). Consistently, we detected CD44 in the hilum OSE by immunohistochemistry and found significantly more CD44^{+} cells in hilum primary cultures versus ovary part cultures. Interestingly, we also found frequent expression of mammary, prostate and skin stem cell marker CK6 (Hsu et al., 2011; Schmelz et al., 2005; Stingl et al., 2006) in primary hilum but not ovary part cultures. This is of particular interest, because CK6 is postulated to participate in the advancement of a stem cell from its specialized niche into a differentiated state (Schmelz et al., 2005).

In humans the area corresponding to the junction part between OSE and the oviduct in the mouse would be a narrow epithelial isthmus extending onto the ovary from the ovarian fimbriae of the Fallopian tube (Auersperg et

al., 2008). Notably, while there is a clear morphologic transition from the OSE to the fimbrial epithelium, epithelial cells in this transitional area express both OSE and fimbrial epithelium markers, calretinin and E-Cadherin, respectively. Based on these observations, it has been proposed that cells in the transitional area may have more plastic and, presumably, less differentiated state. Our findings develop this concept further raising the question whether, similarly to the mouse hilum cells, as well as to human corneal and mouse prostate niches, human cells of epithelial isthmus represent stem cell compartment. This question is of particular importance because transitional areas were found to be particularly susceptible to neoplastic transformation a number of locations, such as the uterine cervix and the esophageal-gastric junction in humans (Auersperg et al., 2008), and prostatic ducts in mice (Zhou et al., 2006).

During recent years it has become increasingly clear that similar to cancers of other locations neoplastic cells in EOC may acquire molecular and cellular mechanisms typical for stem and progenitor cells (Cheng et al., 2010). However, it remains unknown if EOC may arise from the stem cell compartment and if so, whether neoplasms originating from stem/progenitor cells have particularly aggressive behavior. Of interest, ovarian cancer stem cells express ALDH1, CD44 and CD133 (Alvero et al., 2009; Bapat et al., 2005; Deng et al., 2010; Ferrandina et al., 2009), the markers expressed in normal hilum OSE cells according to our observations. Identification and characterization of the OSE stem cell compartment described in our study provide a necessary basis for further studies aimed to understand the molecular and cellular mechanisms that regulate normal ovarian development

and to unravel how aberrations in those regulatory mechanisms may contribute to EOC pathogenesis.

REFERENCES

Alonso, L., and Fuchs, E. (2003). Stem cells of the skin epithelium. Proc Natl Acad Sci U S A *100 Suppl 1*, 11830-11835.

Alvero, A.B., Chen, R., Fu, H.H., Montagna, M., Schwartz, P.E., Rutherford, T., Silasi, D.A., Steffensen, K.D., Waldstrom, M., Visintin, I.*, et al.* (2009). Molecular phenotyping of human ovarian cancer stem cells unravels the mechanisms for repair and chemoresistance. Cell Cycle *8*, 158-166.

Artavanis-Tsakonas, S., Rand, M.D., and Lake, R.J. (1999). Notch signaling: cell fate control and signal integration in development. Science *284*, 770-776.

Auersperg, N., Wong, A.S., Choi, K.C., Kang, S.K., and Leung, P.C. (2001). Ovarian surface epithelium: biology, endocrinology, and pathology. Endocr Rev *22*, 255-288.

Auersperg, N., Woo, M.M., and Gilks, C.B. (2008). The origin of ovarian carcinomas: a developmental view. Gynecol Oncol *110*, 452-454.

Bapat, S.A., Mali, A.M., Koppikar, C.B., and Kurrey, N.K. (2005). Stem and progenitor-like cells contribute to the aggressive behavior of human epithelial ovarian cancer. Cancer Res *65*, 3025-3029.

Barrandon, Y., and Green, H. (1987). Three clonal types of keratinocyte with different capacities for multiplication. Proc Natl Acad Sci U S A *84*, 2302-2306.

Blanpain, C., Horsley, V., and Fuchs, E. (2007). Epithelial stem cells: turning over new leaves. Cell *128*, 445-458.

Bullough, W.S. (1942). Oogenesis and its relation to the oestrous cycle in the adult mouse. Journal of Endocrinology *3*, 141-149.

Burger, P.E., Gupta, R., Xiong, X., Ontiveros, C.S., Salm, S.N., Moscatelli, D., and Wilson, E.L. (2009). High aldehyde dehydrogenase activity: a novel functional marker of murine prostate stem/progenitor cells. Stem Cells *27*, 2220-2228.

Burger, P.E., Xiong, X., Coetzee, S., Salm, S.N., Moscatelli, D., Goto, K., and Wilson, E.L. (2005). Sca-1 expression identifies stem cells in the proximal region of prostatic ducts with high capacity to reconstitute prostatic tissue. Proc Natl Acad Sci U S A *102*, 7180-7185.

Butcher, E.O., and College, H. (1932). The effect of many corpora lutea on germ-cell formation and growth in the ovary of the white rat. The Anatomical Record *54*, 1.

Cheng, L., Ramesh, A.V., Flesken-Nikitin, A., Choi, J., and Nikitin, A.Y. (2010). Mouse models for cancer stem cell research. Toxicol Pathol *38*, 62-71.

Cho, K.R., and Shih Ie, M. (2009). Ovarian cancer. Annu Rev Pathol *4*, 287-313.

Clark-Knowles, K.V., Garson, K., Jonkers, J., and Vanderhyden, B.C. (2007). Conditional inactivation of Brca1 in the mouse ovarian surface epithelium results in an increase in preneoplastic changes. Exp Cell Res *313*, 133-145.

Corti, S., Locatelli, F., Papadimitriou, D., Donadoni, C., Salani, S., Del Bo, R., Strazzer, S., Bresolin, N., and Comi, G.P. (2006). Identification of a primitive brain-derived neural stem cell population based on aldehyde dehydrogenase activity. Stem Cells *24*, 975-985.

Cotsarelis, G., Cheng, S.Z., Dong, G., Sun, T.T., and Lavker, R.M. (1989). Existence of slow-cycling limbal epithelial basal cells that can be preferentially stimulated to proliferate: implications on epithelial stem cells. Cell *57*, 201-209.

Deng, S., Yang, X., Lassus, H., Liang, S., Kaur, S., Ye, Q., Li, C., Wang, L.P., Roby, K.F., Orsulic, S.*, et al.* (2010). Distinct expression levels and patterns of stem cell marker, aldehyde dehydrogenase isoform 1 (ALDH1), in human epithelial cancers. PLoS One *5*, e10277.

Dinulescu, D.M., Ince, T.A., Quade, B.J., Shafer, S.A., Crowley, D., and Jacks, T. (2005). Role of K-ras and Pten in the development of mouse models of endometriosis and endometrioid ovarian cancer. Nat Med *11*, 63-70.

Dubeau, L. (2008). The cell of origin of ovarian epithelial tumours. Lancet Oncol *9*, 1191-1197.

Ezhkova, E., Pasolli, H.A., Parker, J.S., Stokes, N., Su, I.H., Hannon, G., Tarakhovsky, A., and Fuchs, E. (2009). Ezh2 orchestrates gene expression for the stepwise differentiation of tissue-specific stem cells. Cell *136*, 1122-1135.

Ferrandina, G., Martinelli, E., Petrillo, M., Prisco, M.G., Zannoni, G., Sioletic, S., and Scambia, G. (2009). CD133 antigen expression in ovarian cancer. BMC Cancer *9*, 221.

Flesken-Nikitin, A., Choi, K.C., Eng, J.P., Shmidt, E.N., and Nikitin, A.Y. (2003). Induction of carcinogenesis by concurrent inactivation of p53 and Rb1 in the mouse ovarian surface epithelium. Cancer Res *63*, 3459-3463.

Fuchs, E., Tumbar, T., and Guasch, G. (2004). Socializing with the neighbors: stem cells and their niche. Cell *116*, 769-778.

Gentry, T., Foster, S., Winstead, L., Deibert, E., Fiordalisi, M., and Balber, A. (2007). Simultaneous isolation of human BM hematopoietic, endothelial and mesenchymal progenitor cells by flow sorting based on aldehyde dehydrogenase activity: implications for cell therapy. Cytotherapy *9*, 259-274.

Ginestier, C., Hur, M.H., Charafe-Jauffret, E., Monville, F., Dutcher, J., Brown, M., Jacquemier, J., Viens, P., Kleer, C.G., Liu, S.*, et al.* (2007). ALDH1 is a marker of normal and malignant human mammary stem cells and a predictor of poor clinical outcome. Cell Stem Cell *1*, 555-567.

Haylock, D.N., and Nilsson, S.K. (2006). The role of hyaluronic acid in hemopoietic stem cell biology. Regen Med *1*, 437-445.

Hennighausen, L., and Robinson, G.W. (2005). Information networks in the mammary gland. Nat Rev Mol Cell Biol *6*, 715-725.

Hsu, Y.C., Pasolli, H.A., and Fuchs, E. (2011). Dynamics between stem cells, niche, and progeny in the hair follicle. Cell *144*, 92-105.

Huang, E.H., Hynes, M.J., Zhang, T., Ginestier, C., Dontu, G., Appelman, H., Fields, J.Z., Wicha, M.S., and Boman, B.M. (2009). Aldehyde dehydrogenase 1 is a marker for normal and malignant human colonic stem cells (SC) and tracks SC overpopulation during colon tumorigenesis. Cancer Res *69*, 3382-3389.

Jackson, K.S., Inoue, K., Davis, D.A., Hilliard, T.S., and Burdette, J.E. (2009). Three-dimensional ovarian organ culture as a tool to study normal ovarian surface epithelial wound repair. Endocrinology *150*, 3921-3926.

Jemal, A., Siegel, R., Xu, J., and Ward, E. (2010). Cancer statistics, 2010. CA Cancer J Clin *60*, 277-300.

Jones, D.L., and Wagers, A.J. (2008). No place like home: anatomy and function of the stem cell niche. Nat Rev Mol Cell Biol *9*, 11-21.

Kenney, N.J., Smith, G.H., Lawrence, E., Barrett, J.C., and Salomon, D.S. (2001). Identification of Stem Cell Units in the Terminal End Bud and Duct of the Mouse Mammary Gland. J Biomed Biotechnol *1*, 133-143.

Kwong, J., Chan, F.L., Wong, K.K., Birrer, M.J., Archibald, K.M., Balkwill, F.R., Berkowitz, R.S., and Mok, S.C. (2009). Inflammatory cytokine tumor necrosis factor alpha confers precancerous phenotype in an organoid model of normal human ovarian surface epithelial cells. Neoplasia *11*, 529-541.

Lawson, D.A., Xin, L., Lukacs, R.U., Cheng, D., and Witte, O.N. (2007). Isolation and functional characterization of murine prostate stem cells. Proc Natl Acad Sci U S A *104*, 181-186.

Medeiros, F., Muto, M.G., Lee, Y., Elvin, J.A., Callahan, M.J., Feltmate, C., Garber, J.E., Cramer, D.W., and Crum, C.P. (2006). The tubal fimbria is a preferred site for early adenocarcinoma in women with familial ovarian cancer syndrome. Am J Surg Pathol *30*, 230-236.

Nikitin, A., and Lee, W.H. (1996). Early loss of the retinoblastoma gene is associated with impaired growth inhibitory innervation during melanotroph carcinogenesis in Rb+/- mice. Genes Dev *10*, 1870-1879.

Nikitin, A.Y., Nafus, M. G., Zhou, Z., Liao, C.-P., and Roy-Burman, P. (2009). (2009). Prostate stem cells and cancer in animals.

Oliver, J.A., Maarouf, O., Cheema, F.H., Martens, T.P., and Al-Awqati, Q. (2004). The renal papilla is a niche for adult kidney stem cells. J Clin Invest *114*, 795-804.

Orsulic, S., Li, Y., Soslow, R.A., Vitale-Cross, L.A., Gutkind, J.S., and Varmus, H.E. (2002). Induction of ovarian cancer by defined multiple genetic changes in a mouse model system. Cancer Cell *1*, 53-62.

Oshima, H., Rochat, A., Kedzia, C., Kobayashi, K., and Barrandon, Y. (2001). Morphogenesis and renewal of hair follicles from adult multipotent stem cells. Cell *104*, 233-245.

Pece, S., Tosoni, D., Confalonieri, S., Mazzarol, G., Vecchi, M., Ronzoni, S., Bernard, L., Viale, G., Pelicci, P.G., and Di Fiore, P.P. (2010). Biological and molecular heterogeneity of breast cancers correlates with their cancer stem cell content. Cell *140*, 62-73.

Pellegrini, G., Golisano, O., Paterna, P., Lambiase, A., Bonini, S., Rama, P., and De Luca, M. (1999). Location and clonal analysis of stem cells and their differentiated progeny in the human ocular surface. J Cell Biol *145*, 769-782.

Potten, C.S., and Loeffler, M. (1990). Stem cells: attributes, cycles, spirals, pitfalls and uncertainties. Lessons for and from the crypt. Development *110*, 1001-1020.

Rama, P., Matuska, S., Paganoni, G., Spinelli, A., De Luca, M., and Pellegrini, G. (2010). Limbal stem-cell therapy and long-term corneal regeneration. N Engl J Med *363*, 147-155.

Reynolds, B.A., and Weiss, S. (1996). Clonal and population analyses demonstrate that an EGF-responsive mammalian embryonic CNS precursor is a stem cell. Dev Biol *175*, 1-13.

Schermer, A., Galvin, S., and Sun, T.T. (1986). Differentiation-related expression of a major 64K corneal keratin in vivo and in culture suggests limbal location of corneal epithelial stem cells. J Cell Biol *103*, 49-62.

Schmelz, M., Moll, R., Hesse, U., Prasad, A.R., Gandolfi, J. A., Hasan, S. R., Bartholdi, M., and Cress, A. E. (2005). Identification of a stem cell candidate in the normal human prostate gland. Eur J Cell Biol *84*, 341-354.

Scully, R.E. , Henson, D. E., Nielsen, M. L., and Ruby, S. G. (1996). Practice protocol for the examination of specimens removed from patients with ovarian tumors. Cancer *78*, 927-940.

Stein, K.F., and Allen, E. (1942). Attempts to stimulate proliferation of the germinal epithelium of the ovary. The Anatomical Record *82*, 1-9.

Stingl, J., Eirew, P., Ricketson, I., Shackleton, M., Vaillant, F., Choi, D., Li, H.I., and Eaves, C.J. (2006). Purification and unique properties of mammary epithelial stem cells. Nature *439*, 993-997.

Storms, R.W., Trujillo, A.P., Springer, J.B., Shah, L., Colvin, O.M., Ludeman, S.M., and Smith, C. (1999). Isolation of primitive human hematopoietic progenitors on the basis of aldehyde dehydrogenase activity. Proc Natl Acad Sci U S A *96*, 9118-9123.

Szotek, P.P., Chang, H.L., Brennand, K., Fujino, A., Pieretti-Vanmarcke, R., Lo Celso, C., Dombkowski, D., Preffer, F., Cohen, K.S., Teixeira, J.*, et al.* (2008). Normal ovarian surface epithelial label-retaining cells exhibit stem/progenitor cell characteristics. Proc Natl Acad Sci U S A *105*, 12469-12473.

Taylor, G., Lehrer, M.S., Jensen, P.J., Sun, T.T., and Lavker, R.M. (2000). Involvement of follicular stem cells in forming not only the follicle but also the epidermis. Cell *102*, 451-461.

Tsujimura, A., Koikawa, Y., Salm, S., Takao, T., Coetzee, S., Moscatelli, D., Shapiro, E., Lepor, H., Sun, T.T., and Wilson, E.L. (2002). Proximal location of mouse prostate epithelial stem cells: a model of prostatic homeostasis. J Cell Biol *157*, 1257-1265.

Tumbar, T., Guasch, G., Greco, V., Blanpain, C., Lowry, W.E., Rendl, M., and Fuchs, E. (2004). Defining the epithelial stem cell niche in skin. Science *303*, 359-363.

Wu, R., Hendrix-Lucas, N., Kuick, R., Zhai, Y., Schwartz, D.R., Akyol, A., Hanash, S., Misek, D.E., Katabuchi, H., Williams, B.O.*, et al.* (2007). Mouse model of human ovarian endometrioid adenocarcinoma based on somatic defects in the Wnt/beta-catenin and PI3K/Pten signaling pathways. Cancer Cell *11*, 321-333.

Zhang, S., Balch, C., Chan, M.W., Lai, H.C., Matei, D., Schilder, J.M., Yan, P.S., Huang, T.H., and Nephew, K.P. (2008). Identification and characterization of ovarian cancer-initiating cells from primary human tumors. Cancer Res *68*, 4311-4320.

Zhou, Z., Flesken-Nikitin, A., Corney, D.C., Wang, W., Goodrich, D.W., Roy-Burman, P., and Nikitin, A.Y. (2006). Synergy of p53 and Rb deficiency in a conditional mouse model for metastatic prostate cancer. Cancer Res *66*, 7889-7898.

Zhou, Z., Flesken-Nikitin, A., and Nikitin, A.Y. (2007). Prostate cancer associated with p53 and Rb deficiency arises from the stem/progenitor cell-enriched proximal region of prostatic ducts. Cancer Res *67*, 5683-5690.

CHAPTER 7

SUMMARY AND FUTURE DIRECTIONS

7.1 Summary

Alterations in p53 and RB tumor suppressor pathways are detected frequently in epithelial ovarian cancer (EOC), particular in high grade serous adenocarcinomas (Corney et al., 2008; D'Andrilli et al., 2008). To elucidate their roles in EOC pathogenesis we instigated a study to determine whether concurrent inactivation of *p53* and *Rb1* genes in the mouse ovarian surface epithelium (OSE) is sufficient for induction of epithelial ovarian carcinogenesis (Chapter 2, and Flesken-Nikitin et al., 2003). As nearly ninety percent of ovarian cancer cases are believed to be derived from the OSE (Auersperg et al., 2008; Feeley and Wells, 2001), with serous adenocarcinomas comprising around eighty percent of EOC (Bast et al., 2009; Scully et al., 1999) we targeted these cells in mice carrying floxed copies of *p53* and *Rb1* genes (Jonkers et al., 2001; Marino et al., 2000). First, we established a tissue culture method for reproducible generation of primary OSE and OSE cell lines. When primary OSE cells were treated with recombinant adenovirus expressing EGFP (Ad*CMVEGFP*, Anderson et al., 2000) we observed more than 80 % of OSE expressed EGFP after 24 hours after infection. Similar results were received with cultured OSE of *Rosa26STOP^{floxP}LacZ* reporter mice (Chai et al., 2000; Jiang et al., 2000; Soriano et al., 1999) confirming that recombinant adenovirus efficiently infects OSE. Primary OSE derived from mice homozygous for conditional gene alleles (*p53/Rb1* double floxed mice)

and treated with Ad*CMVCre* had deletion of both genes according to PCR analysis. Next we took advantage of the anatomical structure of the mouse ovary, which is completely enveloped with a thin membrane called the bursa. We developed a transinfundibular intrabursal injection technique and, by using different adenoviruses, shown that OSE infection efficiency was similar to that in *ex vivo* experiments. Importantly, no adverse effects of the viruses on the OSE were observed. Utilizing this novel technique of intrabursal administration, we performed concomitant inactivation of *p53* and *Rb1* in the OSE of *p53/Rb1* double floxed mice by injection of Ad*CMVCre*. Loss of both *p53* and *Rb1* genes resulted in 97% of epithelial ovarian neoplasms within 7 to 8 months after single Ad-*Cre* administration. Importantly, these cancers were histopathologically similar to human high grade serous adenocarcinomas. Deletion of only *p53* or *Rb1* resulted in 13 % and 3 % of ovarian neoplasms, respectively. Similarly to progression of malignancy in women (Kurman and Shih Ie, 2010; Lengyel et al., 2010), ovarian cancer spread intraperitoneally, formed ascites, and metastasized to the contralateral ovary, lung, and the liver.

Our results ascertained critical interactions between p53 and RB pathways in EOC pathogenesis, and established a genetically defined immunocompetent mouse model of sporadic EOC. Our in situ OSE-targeting approach is well suitable for studies of different genetic alterations in EOC pathogenesis and has been successfully used in subsequent studies by other investigators (Clark-Knowles et al., 2007; Dinulescu et al., 2005; Wu et al., 2007).

Since in our model EOC develops after a long latency period, we have also decided to established mouse models suitable for fast assessment of

advanced stages of disease. To this end we developed syngeneic lines of OSE. Primary cell cultures were prepared from either *p53*$^{flox/floxP}$*Rb*$^{floxP/floxP}$, *p53*$^{floxP/floxP}$ or wild-type age-matched mice of the same background as described (Chapter 2). Cancer cell lines OSN1 and OSN2 were established by Cre-*loxP* mediated inactivation of *p53* and *Rb* or *p53* alone, after three passages of OSE primary cultures, following continuous passaging upon reaching confluence for more than 20 generations (Corney et al., 2007). At least fifteen oncogenes have been associated with EOC (Bast and Mills & Jr, 2008), among them the *C-MYC* transcription factor. *C-MYC* overexpression was detected in 41-66% of EOCs, while amplification ranged at 20 % of cases (Plisiecka-Halasa et al., 2003). We introduced *c-Myc* by retroviral transduction into OSN1 and OSN2 generating neoplastic cell lines OSN3 and OSN4, respectively (Chapter 4, and Flesken-Nikitin et al., 2008)). OSE cultures from wild-type mice were immortalized by continuous culturing without Ad-*Cre* treatment resulting in cell line OSN5. These cells are non-tumorigenic and carry wild-type p53 (Flesken-Nikitin et al., 2008).

Using the OSN cancer cell lines we developed a mouse model of EOC intraperitoneal spreading (Chapter 4) and have initial evidences that *c-Myc* promotes tumorigenicity of *p53*-and *p53/Rb*- deficient OSE (Flesken-Nikitin et al., 2008).

Cancer screening procedures can be augmented with in vivo imaging techniques. Towards the development of multiphoton microscopy (Denk et al., 1990; Williams et al., 2001; Zipfel et al., 2003a; Zipfel et al., 2003b) as a new imaging modality we established a method for studying cell motility in the living mouse using MPM (Chapter 3, and Flesken-Nikitin et al., 2005). In our work we successfully traced individual cells and monitored their behavior in the

living organism. Furthermore, we provided very detailed description of the whole imaging technology, mouse preparation and anesthesia, labeling target cells with EGFP, implantation of beads coated with chemoattractant (Gu et al., 1999; Luini et al., 1994; Rollins et al., 1988), and the multiphoton microscope equipment, thereby facilitating future advances of the research in this field.

Encouraged by our cell migration work we decided to initiate a follow-on study, testing the suitability of MPM and second harmonic generation (SHG) for high-resolution imaging of EOC (Chapter 4, and Williams et al., 2010). By imaging human biopsy samples and three mouse models of ovarian cancer (Connolly et al., 2003; Flesken-Nikitin et al., 2003), we demonstrated that MPM/SHG (Helmchen and Denk, 2005; Zipfel et al., 2003b) imaging of endogenous tissue emissions allows visualization of unfixed, unsectioned, and unstained tissues at a resolution comparable to that of routinely processed histological sections. At a sub-cellular level we observed atypical neoplastic cells forming glandular structures while imaging human and mouse ovarian adenocarcinomas. In contrast, optical sections of normal OSE presented a single layer with typical squamous morphology. Importantly, differences in the collagenous stroma of normal and cancer tissue were detected via SHG (Zipfel et al., 2003a) imaging. Rigid collagen fibers near the tumor periphery were found to be always perpendicular towards its surface. This feature is not evident in conventionally prepared tissue. The same differences in observations were made by imaging normal and malignant mouse tissues. Furthermore, quantitative morphometric assessment (Deligdisch et al., 1999; Deligdisch et al., 1993; Gil and Deligdisch, 1989) of MPM sections from one of our mouse models, revealed a significant enlargement of nuclei and cytoplasm of OSE at very early stages of carcinogenesis, a second feature which is

difficult to assess in traditional histological assessments. Thirdly, while imaging EOCs in our ascites mouse model, we observed a reproducible red shift of intrinsic fluorescence with respect to normal OSE owing to a distinct red-emitting cell population in neoplasm.

Thus, we show that MPM/SHG imaging is translatable into a clinical setting for diagnosis of EOC biopsy samples and adds three additional auxiliary criteria, namely collagen structure, neoplastic cell size measurements and intrinsic fluorescence red-shift, to the final pathological assessment. Towards, the development of an endoscopic devise for EOC screening procedures we tested a microprobe "stick" objective for laparoscopic (Rogart et al., 2008) imaging in live mice. Tissue stabilization and blood flow disturbing the view are common problems which need to be overcome in life imaging settings. After improvements for tissue rinsing and stabilization by exteriorizing the ovary, we were able to acquire images from neoplastic cells discernable from surrounding normal tissues in our mouse model of disseminated peritoneal EOC. Moreover, we facilitated the intravital screenings of tissues by injection of a fluorescent indicator of protease activity, ProSense 680, (Gounaris et al., 2008) which labeled most neoplastic cells. Notably, our live imaging data corroborated with the results obtained from biopsy samples.

Towards development of targeted drug delivery to ovarian cancer cells we initiated a toxicity and biomedical imaging study of layered nanohybrids (LNH) in the mouse (Chapter 5). Although LNH (Ferrari et al., 2005; Hirsch et al., 2003; LaVan et al., 2002; Vijayanathan et al., 2002; Wagner et al., 2006) are promising vehicles in controlled drug delivery, they were not tested in the whole mammalian system. We administered LNH in all standard clinical routes, intravenoulsy (i.v.), intraperitoneally (i.p.), and subcutaneously (s.c.)

and covered different concentrations, exceeding those likely to be required for targeted delivery of therapeutic compounds. Our results indicated no pronounced toxicity of LNH particles in mice. Furthermore, by intrabursal injection of LNH we demonstrated, via MPM efficient LNH incorporation into the OSE without any detectable toxicological effects. We also tested LNH containing gadolinium (magnetic resonance imaging, MRI, contrast agent) and shown that *in vivo* administration of these particles results in increased MRI contrast of the mouse ovary. Taken together, our results revealed that LNH displayed moderate *in vivo* toxicity and are promising multifunctional nanoscale particles allowing combination of intravital biomedical imaging with controlled drug release.

Recent research supports the notion that cancerous lesions feature a subpopulation of neoplastic cells that may be responsible for cancer initiation and progression. These cells, called cancer stem cells (Deng et al., 2010; Pan and Huang, 2008; Sell et al., 2004), tumor-initiating cells or tumor-propagating cells, share several properties with embryonic and somatic cells, such as self-renewal and multi-potent differentiation. However, little is known if such cells arise from the OSE stem cell compartment. Therefore, our research interest turned to the characterization and functional analysis of previously reported (Szotek et al., 2008) a putative OSE stem cell population previously reported (Chapter 6). We identified Aldehyde dehydrogenase 1 (ALDH1) (Yoshida et al., 1998) as a useful OSE stem cell marker (Gentry et al., 2007; Hess et al., 2004; Storms et al., 1999), demonstrated the clonal origin of OSE spheres derived from an OSE subset grown in 3D sphere assays(Lawson et al., 2007; Xin et al., 2007) and found enrichment of BrdU label retaining cells (LRCs) in the hilum region of the ovary. Notably, most of the BrdU LRCs expressed

ALDH1. In primary sphere cultures grown over 7 consecutive passages, OSE cells generated from the hilum consistently formed conspicuous large clones, which were very rarely formed by OSE cells derived from the anterior segment of ovary. Hilum cells highly expressed the stem cell markers CK6, CD44 and Notch2 as compared to OSE in other parts of the ovary. Additionally, some hilum OSE expressed the epithelial markers Calretinin, and PAX8 and the stem cell markers CD44, CD133, Notch1 and p63. Combining these results we propose that the hilum region of the ovary is a putative OSE stem cell niche.

7.2 Future Directions

Ideal genetically induced EOC mouse models need to fulfill multiple criteria (Cheon and Orsulic, 2011). They should mimic the human tumor histopathology and the multistage processes of carcinogenesis, including ascites formation and metastatic spread (Jonkers and Berns, 2002; Nikitin et al., 2005; Van Dyke and Jacks, 2002). Additionally, they should have similar multiple mutations in specific genes, gross chromosomal aberrations induced by genomic instability, and specific pathway alterations known to be involved in human cancers. Our mouse models closely satisfy these requirements. At the same time, our spontaneous mouse model of EOC has certain limitations, as the transinfundibular intrabursal administration of adenovirus needs specific training of personnel and is time consuming. Cross-contamination of neighboring tissues can occur from leaking the virus and low efficiency of *in vivo* infection for some cell types, such as non-dividing cells might be a disadvantage. Therefore, generation of a genetically modified mice allowing conditional induction of EOC without surgical intervention remains highly

desirable. The development of an OSE specific promoter is crucial for the realization of this goal. Although different mouse models of ovarian cancer were made during recent years (Fong and Kakar, 2009), a specific promoter targeting the OSE was not achieved and no inheritable line that would spontaneously form EOC is available. A project aimed to identify OSE specific promoter would require individual isolation of the OSE, mesothelium, oviductal epithelium and stromal cells by Laser Microdissection (LMD), genome-wide microarray analysis of gene expression profile of isolated cells, identification of OSE specific gene signatures, validation of findings by quantitative RT-PCR and in situ hybridization or immunostaining. After the lack of expression of identified genes has been determined in other organs and systems, computational promoter analysis of selected genes will be initiated, following by preparing BAC constructs for generation of BAC transgenes or knock-ins expressing Cre recombinase. Additional control of Cre recombinase expression will be achieved by using either Tamoxifen or tetracycline-mediated regulation. Among first likely, particularly, considering, our results of higher Notch 1 and Notch 2 expression in OSE-SC, Notch target genes could be promising candidates, but unfortunately they are also expressed in a number of other organs and systems.

We will continue *in vivo* imaging using various modalities. In addition to the MPM we anticipate using the Olympus OV 100 small imaging system (Hayashi et al., 2006) for whole body fluorescence imaging, XenogenIVIS200 (Peterson et al., 2008) for bioluminescence/fluorescence whole body imaging, and Visual Sonics Vevo770 (Olive et al., 2009) hi-resolution ultrasound imaging. In one therapeutic treatment analysis we have already monitored tumor reduction in our mouse model of EOC intraperitoneal spreading

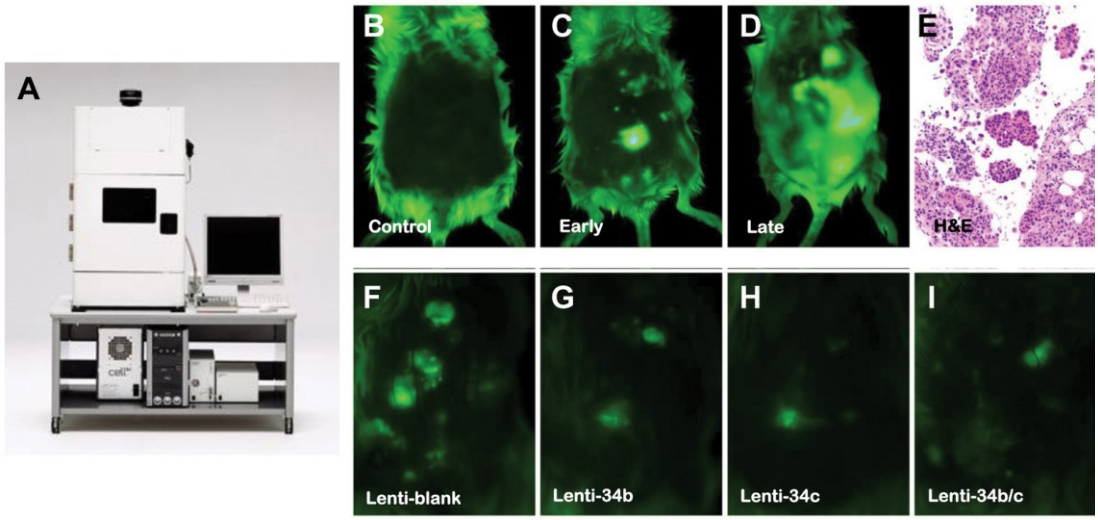

Figure 7.1 Therapeutic treatment analysis in live animals with the OV100. Our ascites epithelial ovarian cancer mouse model is very useful to assess different therapeutic approaches. The Olympus OV100 Small Animal Imaging System (*A*) allows Bright field, GFP 680nm and RFP 750nm fluorescence imaging; 114:1 Zoom ratio; High magnification 1.6 - 16x zoom; Low magnification 0.89x, 0.56x and 0.14x. Mice were injected with OSN1-GFP cell line (*p53/Rb*1 deficient) and tumor growths imaged after 6 - 8 weeks was compared to a control mouse (*B*), early tumor growth (*C*) and late stage of tumor growth (*D*). Histopathology of the same neoplasm; Hematoxylin and Eosin staining (*E*). Cancer mice treated with Lenti-viruses expressing blank (*F*), miR-34b (*G*), miR-34c (*H*) and miR-34b/c virus (*I*) demonstrating tumor reduction.

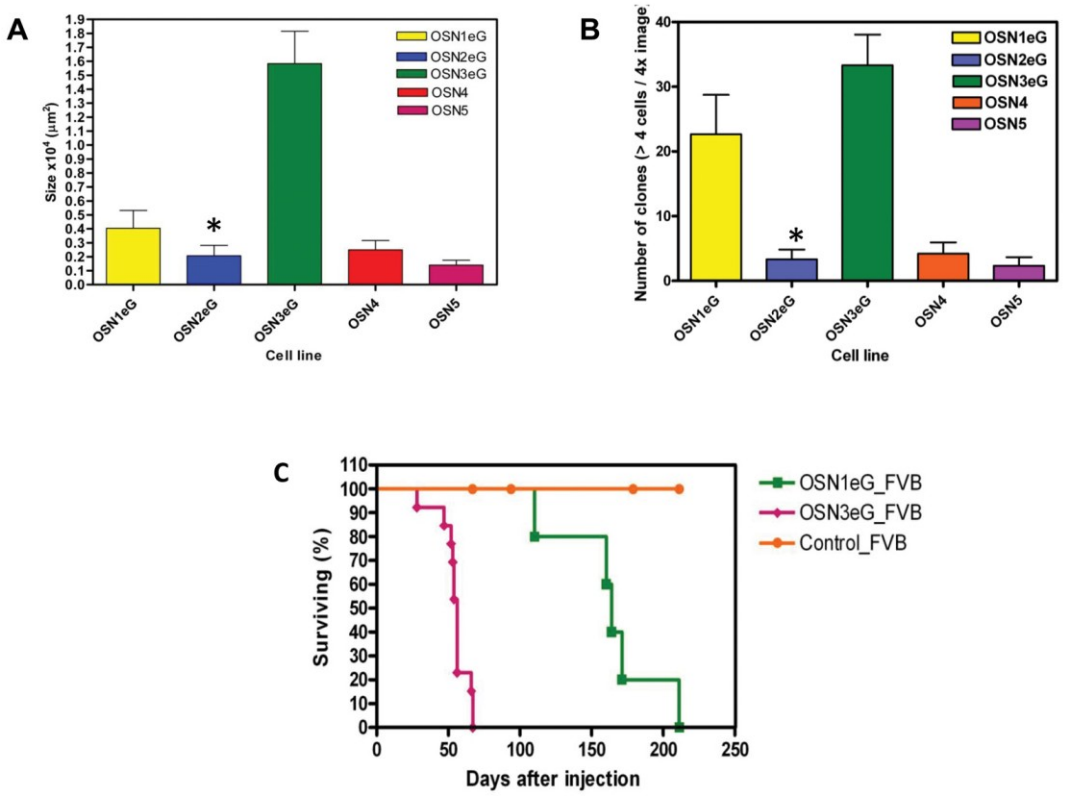

Figure 7.2 *C-Myc* promotes tumorigenicity of *p53*- and *p53/Rb*- deficient OSE. Soft agar assays were performed to test the ability of different OSE cell lines for adhesion independent growth. Bar graph analysis of clone sizes (*A*) or clone number (*B*) from different syngeneic lines of OSE. Graph showing survival data (*C*). Neoplastic cell lines OSN1eG (*p53, Rb* deficient, expressing EGFP), OSN2eG (*p53* deficient, expressing EGFP), OSN3eG (*p53/Rb* deficient, overexpressing *c-Myc*, expressing EGFP), OSN4 (*p53* deficient, overexpressing *c-Myc*), OSN5 (non-transformed); * indicates $P < 0.05$; survival curves $P = 0.001$.

employing the OV100 (Corney, Flesken-Nikitin and Nikitin, unpublished). Tumors induced by our *p53/Rb* deficient epithelial ovarian cancer cell line were treated with Lentivirus expressing the tumor suppressor genes *mir-34b*, *mir-34c* and their combination. The genes of *miR-34* family are direct transcriptional targets of *p53* (Corney et al., 2007). We observed the highest reduction in cancer progression after treatment with Lentivirus expressing both micro RNAs 34b/c (Fig. 7.1).

One area of our studies we are going to extend is related to the *C-MYC* oncogene association with EOC. *C-Myc* plays an important role in normal growth control during mammalian development (Davis et al., 1993) and somatic cell reprogramming into induced pluripotent stem cells (Takahashi and Yamanaka, 2006) indicating deregulated *c-Myc* in stem cells might accelerate carcinogenesis. Interestingly, survival curves and soft agar assays from our syngeneic OSN lines reveal OSE cells *p53*-and *p53/Rb*-deficient and overexpressing *c-Myc* are highly malignant (Flesken-Nikitin et al., 2008) and Fig. 7.2). Notably, corroborating data (Wong et al., 2008) suggests that *c-Myc* is sufficient to reactivate the embryonic stem cell-like program in normal and epithelial cancer cells (Chapter 1). Exploring the function of *c-Myc* in OSE-stem cell homeostasis may reveal important new insights into EOC pathogenesis.

Most of our future work will center on further characterization of somatic OSE stem cells and their relationship with epithelial ovarian carcinogenesis. Several challenges should be addressed in this research. First, enrichment of OSE-SC will be achieved by isolating $ALDH1^+$ OSE cells specifically from the hilum region. In our previous test we used bulk epithelium. These enriched

populations will allow more precise and thorough characterization of OSE stem cells (Szotek et al., 2008).

Secondly, we plan to develop an OSE reconstitution assay. The ability to regenerate tissue *in vivo* is a hallmark of stem cells (Burger et al., 2005; Shackleton et al., 2006; Stingl et al., 2006; Wang et al., 2009). This property has been used to characterize various antigens as stem cell markers. In this way Sca-1 (stem cell antigen-1) was found to be a marker for hematopoietic (Spangrude et al., 1988) and mammary epithelial stem cells (Welm et al., 2002). Sca-1 expressing cells isolated from bone marrow were able to reconstitute all blood cell types. Moreover, mammary epithelial cells enriched for Sca-1 can regenerate the mammary gland *in vivo* and demonstrated greater growth potential than Sca-1 negative cells. Implantation of grafts under the renal capsule (Burger et al., 2005; Li et al., 2010; Xin et al., 2005) and organ cultures (Jackson et al., 2009; Kwong et al., 2009) are tissue regeneration procedures which we will pursue as the initial step in these studies.

Thirdly, to determine the extent of contribution of the hilum OSE-SC to the renewal and regeneration of whole OSE we plan two different approaches: OSE-SC lineage tracing and OSE-SC ablation. For the lineage tracing experiment we plan to test a recently generated *Lgr5-EGFP-IRES-creERT2* knock-in mouse strain (Barker et al., 2007). This strain is likely to be useful because stem cells in the small intestine and colon are characterized by high Lgr5 (leucine rich repeat containing G protein coupled receptor 5) expression. Moreover Lgr5 is expressed in rare cells in several other tissues as in skin stem cells (Hsu et al., 2011; Jaks et al., 2008). Heterozygous Lgr5 animals harbor a "kock-in" allele that both abolishes *Lgr5* gene function and expresses

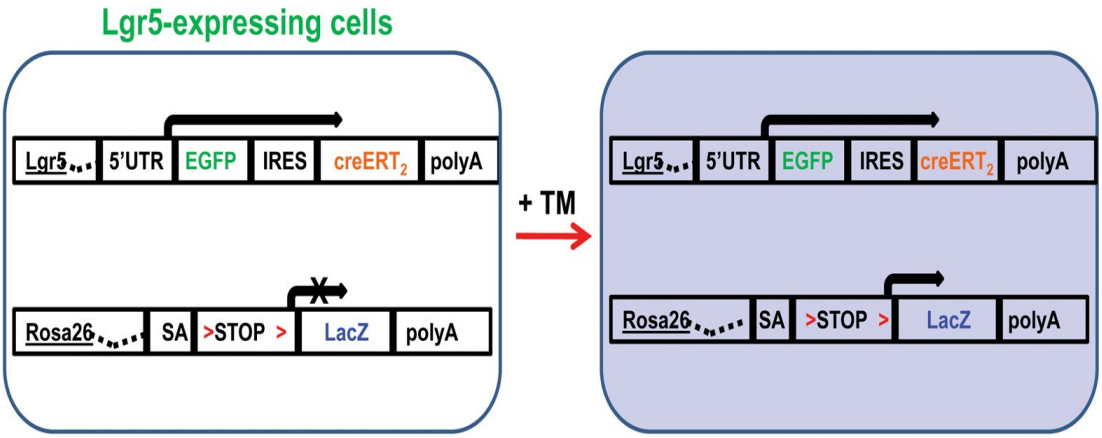

Figure 7.3 Identification of OSE-SC by marker Lgr5. Adapted schematic from Barker et al. (Barker et al., 2007) depicturing generation of mice expressing EGFP and creERT$_2$ from a single bicistronic message by gene knock-in into the first exon of *Lgr5*. Following Tamoxifen treatment the *LacZ* gene is activated and ß-galactosidase can be detected in Lgr5$^+$ cells shown in blue frame. SA, splice acceptor; UTR, untranslated region; EGFP, enhanced green fluorescent protein; IRES, internal ribosome entry site; creERT2, Cre recombinase fused to a G$_{400}$V/M$_{543}$A/L544A triple mutation of the human estrogen receptor ligand binding domain; TM, Tamoxifen.

EGFP and CreERT$_2$ fusion protein from the *Lgr5* promoter/enhancer elements. EGFP fluorescence is observed in Lgr5$^+$ stem cells. Injection of tamoxifen activates the CreERT$_2$ fusion enzyme in Lgr5-expressing cells. Cre-mediated excision of the roadblock sequence in the *Rosa26STOP^{floxP}LacZ* reporter irreversibly marks Lgr5$^+$ cells. Even through potential progeny of these cells will no longer express EGFP, the activated *LacZ* reporter functions as a genetic marker, allowing lineage tracing. If our initial tests show that OSE cells express Lgr5, crosses to the Cre-activatable *Rosa26STOP^{floxP}LacZ* reporter mouse (Soriano et al., 1999) will be made. ß-galactosidase expressing progeny of Lgr5$^+$ will reveal fate and migration of OSE-SC (Barker et al., 2007; Fuchs et al., 2009)(Fig. 7. 3).

For OSE-SC ablation we plan to use MPM. OSE-SC ablation can be achieved by UV pulse delivered through the endoscopic stick objective. We will determine if it is possible to accurately ablate small areas of OSE cells in the living mouse. Tracking tissue regeneration after ablation should reveal cells with extreme high proliferation potential. In both imaging and tracing experiments, tissues collected at different time points 7, 14, 28 and 35 days after treatments should illuminate stem cell fate.

To initiate testing if OSE-SCs have increased potential for malignant transformation, as compared to the rest of OSE cells, we intend to study effects of *p53* and/or *Rb* inactivation on the OSE-SCs and more differentiated OSE cells. This gene inactivation will be accomplished both *ex vivo*, after isolation of individual cell with ALDEFLUOR, followed by their infection with Ad*CMVCre*, and *in vivo* by using adenovirus expressing Cre under the control of ALDH1 promoter. Parameters, such as genome-wide changes in gene expression, proliferation, apoptosis, differentiation, senescence, DNA repair,

invasion and tumorigenicity will be studied in OSE-SC and the rest of OSE before and after gene inactivation.

REFERENCES

Anderson, R.D., Haskell, R.E., Xia, H., Roessler, B.J., and Davidson, B.L. (2000). A simple method for the rapid generation of recombinant adenovirus vectors. Gene Ther *7*, 1034-1038.

Auersperg, N., Woo, M.M., and Gilks, C.B. (2008). The origin of ovarian carcinomas: a developmental view. Gynecol Oncol *110*, 452-454.

Barker, N., van Es, J.H., Kuipers, J., Kujala, P., van den Born, M., Cozijnsen, M., Haegebarth, A., Korving, J., Begthel, H., Peters, P.J.*, et al.* (2007). Identification of stem cells in small intestine and colon by marker gene Lgr5. Nature *449*, 1003-1007.

Bast, R.C., Jr., Hennessy, B., and Mills, G.B. (2009). The biology of ovarian cancer: new opportunities for translation. Nat Rev Cancer *9*, 415-428.

Bast, R.C., and Mills & Jr, G.B., eds. (2008). The Molecular Basis of Cancer (W. B. Saunders Co., Philadelphia).

Burger, P.E., Xiong, X., Coetzee, S., Salm, S.N., Moscatelli, D., Goto, K., and Wilson, E.L. (2005). Sca-1 expression identifies stem cells in the proximal region of prostatic ducts with high capacity to reconstitute prostatic tissue. Proc Natl Acad Sci U S A *102*, 7180-7185.

Chai, Y., Jiang, X., Ito, Y., Bringas, P., Jr., Han, J., Rowitch, D.H., Soriano, P., McMahon, A.P., and Sucov, H.M. (2000). Fate of the mammalian cranial neural crest during tooth and mandibular morphogenesis. Development *127*, 1671-1679.

Cheon, D.J., and Orsulic, S. (2011). Mouse models of cancer. Annu Rev Pathol *6*, 95-119.

Clark-Knowles, K.V., Garson, K., Jonkers, J., and Vanderhyden, B.C. (2007). Conditional inactivation of Brca1 in the mouse ovarian surface epithelium results in an increase in preneoplastic changes. Exp Cell Res *313*, 133-145.

Connolly, D.C., Bao, R., Nikitin, A.Y., Stephens, K.C., Poole, T.W., Hua, X., Harris, S.S., Vanderhyden, B.C., and Hamilton, T.C. (2003). Female mice chimeric for expression of the simian virus 40 TAg under control of the MISIIR promoter develop epithelial ovarian cancer. Cancer Res *63*, 1389-1397.

Corney, D.C., Flesken-Nikitin, A., Choi, J., and Nikitin, A.Y. (2008). Role of p53 and Rb in ovarian cancer. Adv Exp Med Biol *622*, 99-117.

Corney, D.C., Flesken-Nikitin, A., Godwin, A.K., Wang, W., and Nikitin, A.Y. (2007). MicroRNA-34b and MicroRNA-34c are targets of p53 and cooperate in control of cell proliferation and adhesion-independent growth. Cancer Res *67*, 8433-8438.

D'Andrilli, G., Giordano, A., and Bovicelli, A. (2008). Epithelial ovarian cancer: the role of cell cycle genes in the different histotypes. Open Clin Cancer J *2*, 7-12.

Davis, A.C., Wims, M., Spotts, G.D., Hann, S.R., and Bradley, A. (1993). A null c-myc mutation causes lethality before 10.5 days of gestation in homozygotes and reduced fertility in heterozygous female mice. Genes Dev *7*, 671-682.

Deligdisch, L., Gil, J., Kerner, H., Wu, H.S., Beck, D., and Gershoni-Baruch, R. (1999). Ovarian dysplasia in prophylactic oophorectomy specimens: cytogenetic and morphometric correlations. Cancer *86*, 1544-1550.

Deligdisch, L., Miranda, C., Barba, J., and Gil, J. (1993). Ovarian dysplasia: nuclear texture analysis. Cancer *72*, 3253-3257.

Deng, S., Yang, X., Lassus, H., Liang, S., Kaur, S., Ye, Q., Li, C., Wang, L.P., Roby, K.F., Orsulic, S.*, et al.* (2010). Distinct expression levels and patterns of stem cell marker, aldehyde dehydrogenase isoform 1 (ALDH1), in human epithelial cancers. PLoS One *5*, e10277.

Denk, W., Strickler, J.H., and Webb, W.W. (1990). Two-photon laser scanning fluorescence microscopy. Science *248*, 73-76.

Dinulescu, D.M., Ince, T.A., Quade, B.J., Shafer, S.A., Crowley, D., and Jacks, T. (2005). Role of K-ras and Pten in the development of mouse models of endometriosis and endometrioid ovarian cancer. Nat Med *11*, 63-70.

Feeley, K.M., and Wells, M. (2001). Precursor lesions of ovarian epithelial malignancy. Histopathology *38*, 87-95.

Ferrari, M. (2005). Cancer nanotechnology: opportunities and challenges. Nat Rev Cancer *5*, 161-171.

Flesken-Nikitin, A., Choi, K.C., Eng, J.P., Shmidt, E.N., and Nikitin, A.Y. (2003). Induction of carcinogenesis by concurrent inactivation of p53 and Rb1 in the mouse ovarian surface epithelium. Cancer Res *63*, 3459-3463.

Flesken-Nikitin, A., Williams, R.M., Zipfel, W.R., and Nikitin, A.Y. (2008). Modeling epithelial ovarian cancer in the mouse. Proc AACR 5856.

Flesken-Nikitin, A., Williams, R.M., Zipfel, W.R., Webb, W.W., and Nikitin, A.Y. (2005). Use of multiphoton imaging for studying cell migration in the mouse. Methods Mol Biol *294*, 335-345.

Fong, M.Y., and Kakar, S.S. (2009). Ovarian cancer mouse models: a summary of current models and their limitations. J Ovarian Res *2*, 12.

Fuchs, E. (2009). The tortoise and the hair: slow-cycling cells in the stem cell race. Cell *137*, 811-819.

Gentry, T., Foster, S., Winstead, L., Deibert, E., Fiordalisi, M., and Balber, A. (2007). Simultaneous isolation of human BM hematopoietic, endothelial and mesenchymal progenitor cells by flow sorting based on aldehyde dehydrogenase activity: implications for cell therapy. Cytotherapy *9*, 259-274.

Gil, J., and Deligdisch, L. (1989). Interactive morphometric procedures and statistical analysis in the diagnosis of ovarian dysplasia and carcinoma. Pathol Res Pract *185*, 680-685.

Gounaris, E., Tung, C.H., Restaino, C., Maehr, R., Kohler, R., Joyce, J.A., Ploegh, H.L., Barrett, T.A., Weissleder, R., and Khazaie, K. (2008). Live imaging of cysteine-cathepsin activity reveals dynamics of focal inflammation, angiogenesis, and polyp growth. PLoS One *3*, e2916.

Gu, L., Tseng, S.C., and Rollins, B.J. (1999). Monocyte chemoattractant protein-1. Chem Immunol *72*, 7-29.

Hayashi, T., Imai, K., Morishita, Y., Hayashi, I., Kusunoki, Y., and Nakachi, K. (2006). Identification of the NKG2D haplotypes associated with natural cytotoxic activity of peripheral blood lymphocytes and cancer immunosurveillance. Cancer Res *66*, 563-570.

Helmchen, F., and Denk, W. (2005). Deep tissue two-photon microscopy. Nat Methods *2*, 932-940.

Hess, D.A., Meyerrose, T.E., Wirthlin, L., Craft, T.P., Herrbrich, P.E., Creer, M.H., and Nolta, J.A. (2004). Functional characterization of highly purified human hematopoietic repopulating cells isolated according to aldehyde dehydrogenase activity. Blood *104*, 1648-1655.

Hirsch, L.R., Stafford, R.J., Bankson, J.A., Sershen, S.R., Rivera, B., Price, R.E., Hazle, J.D., Halas, N.J., and West, J.L. (2003). Nanoshell-mediated near-infrared thermal therapy of tumors under magnetic resonance guidance. Proc Natl Acad Sci U S A *100*, 13549-13554.

Hsu, Y.C., Pasolli, H.A., and Fuchs, E. (2011). Dynamics between stem cells, niche, and progeny in the hair follicle. Cell *144*, 92-105.

Jackson, K.S., Inoue, K., Davis, D.A., Hilliard, T.S., and Burdette, J.E. (2009). Three-dimensional ovarian organ culture as a tool to study normal ovarian surface epithelial wound repair. Endocrinology *150*, 3921-3926.

Jaks, V., Barker, N., Kasper, M., van Es, J.H., Snippert, H.J., Clevers, H., and Toftgard, R. (2008). Lgr5 marks cycling, yet long-lived, hair follicle stem cells. Nat Genet *40*, 1291-1299.

Jiang, X., Rowitch, D.H., Soriano, P., McMahon, A.P., and Sucov, H.M. (2000). Fate of the mammalian cardiac neural crest. Development *127*, 1607-1616.

Jonkers, J., and Berns, A. (2002). Conditional mouse models of sporadic cancer. Nat Rev Cancer *2*, 251-265.

Jonkers, J., Meuwissen, R., van der Gulden, H., Peterse, H., van der Valk, M., and Berns, A. (2001). Synergistic tumor suppressor activity of BRCA2 and p53 in a conditional mouse model for breast cancer. Nat Genet *29*, 418-425.

Kurman, R.J., and Shih Ie, M. (2010). The origin and pathogenesis of epithelial ovarian cancer: a proposed unifying theory. Am J Surg Pathol *34*, 433-443.

Kwong, J., Chan, F.L., Wong, K.K., Birrer, M.J., Archibald, K.M., Balkwill, F.R., Berkowitz, R.S., and Mok, S.C. (2009). Inflammatory cytokine tumor necrosis factor alpha confers precancerous phenotype in an organoid model of normal human ovarian surface epithelial cells. Neoplasia *11*, 529-541.

LaVan, D.A., Lynn, D.M., and Langer, R. (2002). Moving smaller in drug discovery and delivery. Nat Rev Drug Discov *1*, 77-84.

Lawson, D.A., Xin, L., Lukacs, R.U., Cheng, D., and Witte, O.N. (2007). Isolation and functional characterization of murine prostate stem cells. Proc Natl Acad Sci U S A *104*, 181-186.

Lengyel, E. (2010). Ovarian Cancer Development and Metastasis. The American Journal of Pathology *177*, 1053-1064.

Li, J., Kawamura, K., Cheng, Y., Liu, S., Klein, C., Duan, E.K., and Hsueh, A.J. (2010). Activation of dormant ovarian follicles to generate mature eggs. Proc Natl Acad Sci U S A *107*, 10280-10284.

Luini, W., Sozzani, S., Van Damme, J., and Mantovani, A. (1994). Species-specificity of monocyte chemotactic protein-1 and -3. Cytokine *6*, 28-31.

Marino, S., Vooijs, M., van Der Gulden, H., Jonkers, J., and Berns, A. (2000). Induction of medulloblastomas in p53-null mutant mice by somatic inactivation

of Rb in the external granular layer cells of the cerebellum. Genes Dev *14*, 994-1004.

Nikitin, A.Y., and Hamilton, T. C. (2005). Modeling ovarian cancer in the mouse. RE Adv in Cancer, 2005 *5*, 49-59.

Olive, K.P., Jacobetz, M.A., Davidson, C.J., Gopinathan, A., McIntyre, D., Honess, D., Madhu, B., Goldgraben, M.A., Caldwell, M.E., Allard, D*., et al.* (2009). Inhibition of Hedgehog signaling enhances delivery of chemotherapy in a mouse model of pancreatic cancer. Science *324*, 1457-1461.

Pan, Y., and Huang, X. (2008). Epithelial ovarian cancer stem cells-a review. Int J Clin Exp Med *1*, 260-266.

Peterson, J.R., Infanger, D.W., Braga, V.A., Zhang, Y., Sharma, R.V., Engelhardt, J.F., and Davisson, R.L. (2008). Longitudinal noninvasive monitoring of transcription factor activation in cardiovascular regulatory nuclei using bioluminescence imaging. Physiol Genomics *33*, 292-299.

Plisiecka-Halasa, J., Karpinska, G., Szymanska, T., Ziolkowska, I., Madry, R., Timorek, A., Debniak, J., Ulanska, M., Jedryka, M., Chudecka-Glaz, A*., et al.* (2003). P21WAF1, P27KIP1, TP53 and C-MYC analysis in 204 ovarian carcinomas treated with platinum-based regimens. Ann Oncol *14*, 1078-1085.

Rogart, J.N., Nagata, J., Loeser, C.S., Roorda, R.D., Aslanian, H., Robert, M.E., Zipfel, W.R., and Nathanson, M.H. (2008). Multiphoton imaging can be used for microscopic examination of intact human gastrointestinal mucosa ex vivo. Clin Gastroenterol Hepatol *6*, 95-101.

Rollins, B.J., Morrison, E.D., and Stiles, C.D. (1988). Cloning and expression of JE, a gene inducible by platelet-derived growth factor and whose product has cytokine-like properties. Proc Natl Acad Sci U S A *85*, 3738-3742.

Scully, R.E. (1999). Histological typing of ovarian tumours, Vol 9 (New York, Springer Berlin).

Sell, S. (2004). Stem cell origin of cancer and differentiation therapy. Crit Rev Oncol Hematol *51*, 1-28.

Shackleton, M., Vaillant, F., Simpson, K.J., Stingl, J., Smyth, G.K., Asselin-Labat, M.L., Wu, L., Lindeman, G.J., and Visvader, J.E. (2006). Generation of a functional mammary gland from a single stem cell. Nature *439*, 84-88.

Soriano, P. (1999). Generalized lacZ expression with the ROSA26 Cre reporter strain. Nat Genet *21*, 70-71.

Spangrude, G.J., Heimfeld, S., and Weissman, I.L. (1988). Purification and characterization of mouse hematopoietic stem cells. Science *241*, 58-62.

Stingl, J., Eirew, P., Ricketson, I., Shackleton, M., Vaillant, F., Choi, D., Li, H.I., and Eaves, C.J. (2006). Purification and unique properties of mammary epithelial stem cells. Nature *439*, 993-997.

Storms, R.W., Trujillo, A.P., Springer, J.B., Shah, L., Colvin, O.M., Ludeman, S.M., and Smith, C. (1999). Isolation of primitive human hematopoietic progenitors on the basis of aldehyde dehydrogenase activity. Proc Natl Acad Sci U S A *96*, 9118-9123.

Szotek, P.P., Chang, H.L., Brennand, K., Fujino, A., Pieretti-Vanmarcke, R., Lo Celso, C., Dombkowski, D., Preffer, F., Cohen, K.S., Teixeira, J.*, et al.* (2008). Normal ovarian surface epithelial label-retaining cells exhibit stem/progenitor cell characteristics. Proc Natl Acad Sci U S A *105*, 12469-12473.

Takahashi, K., and Yamanaka, S. (2006). Induction of pluripotent stem cells from mouse embryonic and adult fibroblast cultures by defined factors. Cell *126*, 663-676.

Van Dyke, T., and Jacks, T. (2002). Cancer modeling in the modern era: progress and challenges. Cell *108*, 135-144.

Vijayanathan, V., Thomas, T., and Thomas, T.J. (2002). DNA nanoparticles and development of DNA delivery vehicles for gene therapy. Biochemistry *41*, 14085-14094.

Wagner, V., Dullaart, A., Bock, A.K., and Zweck, A. (2006). The emerging nanomedicine landscape. Nat Biotechnol *24*, 1211-1217.

Wang, X., Kruithof-de Julio, M., Economides, K.D., Walker, D., Yu, H., Halili, M.V., Hu, Y.P., Price, S.M., Abate-Shen, C., and Shen, M.M. (2009). A luminal epithelial stem cell that is a cell of origin for prostate cancer. Nature *461*, 495-500.

Welm, B.E., Tepera, S.B., Venezia, T., Graubert, T.A., Rosen, J.M., and Goodell, M.A. (2002). Sca-1(pos) cells in the mouse mammary gland represent an enriched progenitor cell population. Dev Biol *245*, 42-56.

Williams, R.M., Flesken-Nikitin, A., Ellenson, L.H., Connolly, D.C., Hamilton, T.C., Nikitin, A.Y., and Zipfel, W.R. (2010). Strategies for high-resolution imaging of epithelial ovarian cancer by laparoscopic nonlinear microscopy. Transl Oncol *3*, 181-194.

Williams, R.M., Zipfel, W.R., and Webb, W.W. (2001). Multiphoton microscopy in biological research. Curr Opin Chem Biol *5*, 603-608.

Wong, D.J., Liu, H., Ridky, T.W., Cassarino, D., Segal, E., and Chang, H.Y. (2008). Module map of stem cell genes guides creation of epithelial cancer stem cells. Cell Stem Cell *2*, 333-344.

Wu, R., Hendrix-Lucas, N., Kuick, R., Zhai, Y., Schwartz, D.R., Akyol, A., Hanash, S., Misek, D.E., Katabuchi, H., Williams, B.O.*, et al.* (2007). Mouse model of human ovarian endometrioid adenocarcinoma based on somatic defects in the Wnt/beta-catenin and PI3K/Pten signaling pathways. Cancer Cell *11*, 321-333.

Xin, L., Lawson, D.A., and Witte, O.N. (2005). The Sca-1 cell surface marker enriches for a prostate-regenerating cell subpopulation that can initiate prostate tumorigenesis. Proc Natl Acad Sci U S A *102*, 6942-6947.

Xin, L., Lukacs, R.U., Lawson, D.A., Cheng, D., and Witte, O.N. (2007). Self-renewal and multilineage differentiation in vitro from murine prostate stem cells. Stem Cells *25*, 2760-2769.

Yoshida, A., Rzhetsky, A., Hsu, L.C., and Chang, C. (1998). Human aldehyde dehydrogenase gene family. Eur J Biochem *251*, 549-557.

Zipfel, W.R., Williams, R.M., Christie, R., Nikitin, A.Y., Hyman, B.T., and Webb, W.W. (2003a). Live tissue intrinsic emission microscopy using multiphoton-excited native fluorescence and second harmonic generation. Proc Natl Acad Sci U S A *100*, 7075-7080.

Zipfel, W.R., Williams, R.M., and Webb, W.W. (2003b). Nonlinear magic: multiphoton microscopy in the biosciences. Nat Biotechnol *21*, 1369-1377.

APPENDIX

SUMMARY OF ADDITIONAL RELEVANT PUBLICATIONS WITH CONTRIBUTIONS BY THE AUTHOR

MAMMARY CARCINOMA SUPPRESSION BY CELLULAR RETINOIC ACID BINDING PROTEIN-II

Danny Manor, Elena N. Shmidt, Anuradha Budhu, Andrea Flesken-Nikitin, Marsha Zgola, Rodney Page, Alexander Yu. Nikitin, and Noa Noy, (2003). Cancer Research. 63: 4426-4433. PMID: 12907615.

Abstract

Retinoic acid (RA) modulates cell proliferation, differentiation, and apoptosis, and is used in chemotherapy and chemoprevention in several human cancers. RA exerts its pleiotropic activities by activating the nuclear receptors, retinoic acid receptor (RAR), which, in turn, regulate transcription of multiple target genes. In cells, RA also associates with cellular RA-binding proteins [cellular RA binding proteins (CRABPs)-I and -II]. Recent studies revealed that CRABP-II functions by “channeling” RA to RAR, thereby enhancing the transcriptional activity of the receptor. In search for a biologically meaningful role for CRABP-II, we examined its effect on RA-induced growth inhibition in RA-resistant tumors. Stable expression of CRABP-II in mammary carcinoma SC115 cells enabled activation of RAR, considerably sensitized the cells to RAinduced growth inhibition, and dramatically suppressed their tumorigenicity in immunodeficient mice. Similarly, injection of an adenovirus expressing CRABP-II into mammary carcinomas that spontaneously develop in TgN(*MMTVneu*)202Mul mice resulted in a significant delay in tumor growth and in prolonged survival rates. Remarkably, in both mouse models, administration of exogenous RA had no additional beneficial effect, indicating that endogenous levels of RA are sufficient for maximal tumor suppression on CRABP-II overexpression. The observations reveal that CRABP-II plays a critical role in sensitizing tumors to the growth-suppressive activities of RA *in vivo*.

SUPPRESSION OF MELANOTROPH CARCINOGENESIS LEADS TO ACCELERATED PROGRESSION OF PITUITARY ANTERIO LOBE TUMORS AND MEDULLAR THYROID CARCINOMAS IN RB+/- MICE

Zongxiang Zhou, Andrea Flesken-Nikitin, Corinna G. Levine, Elena N. Shmidt, Jessica P. Eng,Ekaterina Yu. Nikitina, David M. Spencer, and Alexander Yu. Nikitin, (2005). Cancer Research. 65: 787-796. PMID: 15705875.

Abstract

Mice with a single copy of the retinoblastoma gene (Rb+/-) develop a syndrome of multiple neuroendocrine neoplasia. They usually succumb to fast-growing, Rb-deficient melanotroph tumors of the pituitary intermediate lobe, which are extremely rare in humans. Thus, full assessment of Rb role in other, more relevant to human pathology, neoplasms is complicated. To prevent melanotroph neoplasia while preserving spontaneous carcinogenesis in other types of cells, we have prepared transgenic mice in which 770-bp fragment of pro-opiomelanocortin promoter directs expression of the human RB gene to melanotrophs (TgPOMC-RB). In three independent lines, transgenic mice crossed to Rb+/- background are devoid of melanotroph tumors but develop the usual spectrum of other neoplasms. Interestingly, abrogation of melanotroph carcinogenesis results in accelerated progression of pituitary anterior lobe tumors and medullary thyroid carcinomas. A combination of immunologic tests, cell culture studies, and tumorigenicity assays indicates that a-melanocyte–stimulating hormone, which is overproduced by melanotroph tumors, attenuates neoplastic progression by decreasing cell proliferation and inducing apoptosis. Taken together, we show that cell lineage–specific complementation of Rb function can be successfully used for refining available models of stochastic carcinogenesis and identify a-melanocyte–stimulating hormone as a potential attenuating factor during progression of neuroendocrine neoplasms.

SYNERGY OF P53 AND RB DEFICIENCY IN A CONDITIONAL MOUSE MODEL FOR METASTATIC PROSTATE CANCER

Zongxiang Zhou, Andrea Flesken-Nikitin, David C. Corney, Wei Wang, David W. Goodrich, Pradip Roy-Burman, and Alexander Yu. Nikitin, (2006). Cancer Research. 66:7889-7898. PMID: 16912162.

Abstract

Pathways mediated by p53 and Rb are frequently altered in aggressive human cancers, including prostate carcinoma. To test directly the roles of *p53* and *Rb* in prostate carcinogenesis, we have conditionally inactivated these genes in the prostate epithelium of the mouse. Inactivation of either *p53* or *Rb* leads to prostatic intraepithelial neoplasia developing from the luminal epithelium by 600 days of age. In contrast, inactivation of both genes results in rapidly developing (median survival 226 days) carcinomas demonstrating both epithelial and neuroendocrine differentiation. The resulting neoplasms are highly metastatic, resistant to androgen depletion from the early stage of development, and marked with multiple gene expression signatures commonly found in human prostate carcinomas. Interestingly, gains at 4qC3 and 4qD2.2 and loss at 14qA2-qD2, have been consistently found by comparative genomic hybridization. These loci contain such human cancer-related genes as *NFIB, L-myc* and *Nkx3.1,* respectively. Our studies demonstrate a critical role for p53 and Rb deficiency in prostate carcinogenesis and identify likely secondary genetic alterations. The new genetically defined model should be particularly valuable for providing new molecular insights into the pathogenesis of human prostate cancer.

PROSTATE CANCER ASSOCIATED WITH P53 AND RB DEFICIENCY ARISES FROM THE STEM/PROGENITOR CELL-ENRICHED PROXIMAL REGION OF PROSTATIC DUCTS

Zongxiang Zhou, Andrea Flesken-Nikitin, and Alexander Yu. Nikitin, (2007). Cancer Research. 67: 5683-5690. PMID: 17553900.

Abstract

Recently, we have shown that prostate epithelium–specific deficiency for p53 and Rb tumor suppressors leads to metastatic cancer, exhibiting features of both luminal and neuroendocrine differentiation. Using stage-by-stage evaluation of carcinogenesis in this model, we report that all malignant neoplasms arise from the proximal region of the prostatic ducts, the compartment highly enriched for prostatic stem/progenitor cells. In close similarity to reported properties of prostatic stem cells, the cells of the earliest neoplastic lesions express stem cell marker stem cell antigen 1 and are not sensitive to androgen withdrawal. Like a subset of normal cells located in the proximal region of prostatic ducts, the early neoplastic cells coexpress luminal epithelium markers cytokeratin 8, androgen receptor, and neuroendocrine markers synaptophysin and chromogranin A. Inactivation of p53 and Rb also takes place in the lineage-committed transit-amplifying and/or differentiated cells of the distal region of the prostatic ducts. However, the resulting prostatic intraepithelial neoplasms never progress to carcinoma by the time of mouse death. Interestingly, in an ectopic transplantation assay, early mutant cells derived from either region of the prostatic ducts are capable of forming neoplasms within 3 months. These findings indicate that p53 and Rb are critically important for the regulation of the prostatic stem cell compartment, the transformation in which may lead to particularly aggressive cancers in the context of microenvironment.

MICRORNA-34B AND MICRORNA-34C ARE TARGETS OF P53 AND COOPERATE IN CONTROL OF CELL PROLIFERATION AND ADHESION-INDEPENDENT GROWTH

David C. Corney, Andrea Flesken-Nikitin, Andrew K. Godwin, Wei Wang, and Alexander Yu. Nikitin, (2007). Cancer Research. 67: 8433-8438. PMID: 17553900.

Abstract

MicroRNAs (miRNA) are a recently discovered class of noncoding RNAs that negatively regulate gene expression. Recent evidence indicates that miRNAs may play an important role in cancer. However, the mechanism of their deregulation in neoplastic transformation has only begun to be understood. To elucidate the role of tumor suppressor p53 in regulation of miRNAs, we have analyzed changes in miRNA microarray expression profile immediately after conditional inactivation of p53 in primary mouse ovarian surface epithelium cells. Among the most significantly affected miRNAs were miR-34b and miR-34c, which were down-regulated 12-fold according to quantitative reverse transcription–PCR analysis. Computational promoter analysis of the mir-34b/mir-34c locus identified the presence of evolutionarily conserved p53 binding sites f3 kbups tream of the miRNA coding sequence. Consistent with evolutionary conservation, mir-34b/mir-34c were also down-regulated in p53-null human ovarian carcinoma cells. Furthermore, as expected from p53 binding to the mir- 34b/c promoter, doxorubicin treatment of wild-type, but not p53-deficient, cells resulted in an increase of mir-34b/ mir-34c expression. Importantly, miR-34b and miR-34c cooperate in suppressing proliferation and soft-agar colony formation of neoplastic epithelial ovarian cells, in agreement with the partially overlapping spectrum of their predicted targets. Taken together, these results show the existence of a novel mechanism by which p53 suppresses such critical components of neoplastic growth as cell proliferation and adhesion-independent colony formation.

CORE-SHELL SILICA NANOPARTICLES AS FLUORESCENT LABELS FOR NANOMEDICINE

Jinhyang Choi, Andrew A. Burns, Rebecca M. Williams, Zongxiang Zhou, Andrea Flesken-Nikitin, Warren R. Zipfel, Ulrich Wiesner, and Alexander Yu. Nikitin, (2008). Journal of Biomedical Optics. 12: 064007-1-11. PMID: 18163823.

Abstract.

Progress in biomedical imaging depends on the development of probes that combine low toxicity with high sensitivity, resolution, and stability. Toward that end, a new class of highly fluorescent core-shell silica nanoparticles with narrow size distributions and enhanced photostability, known as C dots, provide an appealing alternative to quantum dots. Here, C dots are evaluated with a particular emphasis on *in-vivo* applications in cancer biology. It is established that C dots are nontoxic at biologically relevant concentrations, and can be used in a broad range of imaging applications including intravital visualization of capillaries and macrophages, sentinel lymph node mapping, and peptide-mediated multicolor cell labeling for realtime imaging of tumor metastasis and tracking of injected bone marrow cells in mice. These results demonstrate that fluorescent coreshell silica nanoparticles represent a powerful novel imaging tool within the emerging field of nanomedicine.

ROLE OF P53 AND RB IN OVARIAN CANCER

David C. Corney, Andrea Flesken-Nikitin, Jinhyang Choi, and Alexander Yu. Nikitin, (2008). Advances in Experimental Medicine and Biology. 622: 99-117. PMID: 18546622.

Abstract

Ovarian cancer remains a major health concern worldwide, primarily in postmenopausal women. Among the most common genetic alterations in human sporadic epithelial ovarian cancer (EOC) are *p53* mutations, defective retinoblastoma (RB) pathway ($p16^{Ink4a}$/RB) and activation of oncogenes such as *c-myc*, *K-ras* and *Akt*. Although these alterations are frequently associated with poor clinical prognosis, their specific contributions to EOC formation remain unclear. In order to gain a better understanding of the roles of these proteins *in vivo*, a number of mouse models have been generated, largely based upon inducing specific genetic lesions in the ovarian surface epithelium from which the majority of carcinomas are thought to arise in humans. Here, we review the role of tumor suppressor p53 and the Rb pathway in EOC with particular attention to association of p53 to high grade serous carcinomas as opposed to low grade and benign tumors. We also provide an overview of the utility and application of genetically engineered mouse models, in particular towards rational drug design and development of improved imaging techniques in ovarian cancer.

CELL LINEAGE-SPECIFIC INTERACTIONS BETWEEN MEN1 AND RB IN NEUROENDOCRINE NEOPLASIA

Andres Matoso, Zongxiang Zhou, Ryo Hayama, Andrea Flesken-Nikitin, and Alexander Yu. Nikitin, (2008). Carcinogenesis. 29: 620-628. PMID: 17893233.

Abstract

Inactivation of multiple endocrine neoplasia (MEN) type 1 gene (Men1) results in development of multiple endocrine tumors in Men11/2 mice and in humans. Intriguingly, loss of the wild-type retinoblastoma 1 (Rb) gene also leads to MEN-like phenotype in Rb1/2 mice. To evaluate potential genetic interactions between these genes, we prepared and characterized Men11/2Rb1/2 compound mice in parallel with their parental genotypes. Men1 and Rb did not cooperate in tumor suppression, as demonstrated by comparable survival rates of Rb1/2 and Men11/2Rb1/2 mice, absence of tumor growth acceleration and lack of novel neoplasms. Notably, the loss of the remaining copy of the wild-type Men1 and Rb was mutually exclusive in all tumors of Men11/2Rb1/2 mice, including pituitary anterior lobe and adrenal medulla neoplasms shared by Rb- and Men1-deficient phenotypes. Down-regulation of Men1 targets p18 and p27 and increased presence of phosphorylated-Rb were observed in Men1-deficient pheochromocytomas of Men11/2Rb1/2 and Men11/2 mice. At the same time, the RNA interference (RNAi) knock-down of Men1 mRNA resulted in increased apoptosis of Rb-deficient medullary thyroid carcinoma cells. These results demonstrate that, depending on cell lineage context, combined Men1 and Rb deficiency may be either redundant or detrimental to neoplastic growth. Identification of cell lineage-specific interactions between Men1 and Rb may have important implications for development of rationally designed therapeutic approaches.

MOUSE MODELS FOR CANCER STEM CELL RESEARCH

Le Cheng, Anirudh V. Ramesh, Andrea Flesken-Nikitin, Jinhuang Choi, and Alexander Yu. Nikitin, (2010). Toxicologic Pathology. 38: 62-71. PMID: 19920280.

Abstract

The cancer stem cell concept assumes that cancers are mainly sustained by a small pool of neoplastic cells, known as cancer stem cells or tumor initiating cells, which are able to reproduce themselves and produce phenotypically heterogeneous cells with lesser tumorigenic potential. Cancer stem cells represent an appealing target for development of more selective and efficient therapies. However, direct testing of the cancer stem cell concept and assessment of its therapeutic implications in human cancers have been complicated by the use of immunocompromised mice. Genetically defined immunocompetent autochthonous mouse models of human cancer provide a valuable tool to address this problem. Furthermore, they allow for a better understanding of the relevance of mechanisms controlling normal stem cell compartment to carcinogenesis. Advantages and disadvantages of some of the existing mouse models are reviewed, and future challenges in cancer stem cell research are outlined.

FREQUENT DOWNREGULATION OF MIR-34 FAMILY IN HUMAN OVARIAN CANCERS

David C. Corney, Chang-Il Hwang, Andres Matoso, Markus Vogt, Andrea Flesken-Nikitin, Andrew K. Godwin, Aparna A. Kamat, Anil K. Sood, Lora H. Ellenson, Heiko Hermeking, and Alexander Yu. Nikitin, (2010). Clinical Cancer Research. 16: 1119-1128. PMID: 20145172.

Abstract

Purpose: The miR-34 family is directly transactivated by tumor suppressor p53, which is frequently mutated in human epithelial ovarian cancer (EOC). We hypothesized that miR-34 expression would be decreased in EOC and that reconstituted miR-34 expression might reduce cell proliferation and invasion of EOC cells. Experimental Designs: miR-34 expression was determined by quantitative reverse transcription-PCR and in situ hybridization in a panel of 83 human EOC samples. Functional characterization of miR-34 was accomplished by reconstitution of miR-34 expression in EOC cells with synthetic pre-miR molecules followed by determining changes in proliferation, apoptosis, and invasion. Results: miR-34a expression is decreased in 100%, and miR-34b*/c in 72%, of EOC with p53 mutation, whereas miR-34a is also downregulated in 93% of tumors with wild-type p53. Furthermore, expression of miR-34b*/c is significantly reduced in stage IV tumors compared with stage III ($P = 0.0171$ and $P = 0.0029$, respectively). Additionally, we observed promoter methylation and copy number variations at mir-34. In situ hybridization showed that miR-34a expression is inversely correlated with MET immunohistochemical staining, consistent with translational inhibition by miR-34a. Finally, miR-34 reconstitution experiments in p53 mutant EOC cells resulted in reduced proliferation, motility, and invasion, the latter of which was dependent on MET expression. Conclusions: Our work suggests that miR-34 family plays an important role in EOC pathogenesis and reduced expression of miR-34b*/c may be particularly important for progression to the most advanced stages. Part of miR-34 effects on motility and invasion may be explained by regulation of MET, which is frequently overexpressed in EOC.

MOUSE PROSTATE CANCER CELL LINES ESTABLISHED FROM PRIMARY AND POSTCASTRATION RECURRENT TUMORS

Chun-Peng Liao, Mengmeng Liang, Michael B. Cohen, Andrea Flesken-Nikitin, Joseph H. Jeong, Alexander Yu. Nikitin, and Pradip Roy-Burman, (2010). Hormones and Cancer. 1: 44-45. PMID: 20631921.

Abstract

The clinical course of prostate cancer is grouped into two broad phases. The first phase, which is the growth of the androgen-dependent cancer (AD-Ca), responds well to androgen depletion treatment while the second phase that could be termed as androgen-depletion-independent cancer (ADI-Ca) does not. We used two separate prostate tumors, one AD-Ca and one ADI-Ca from the conditional Pten deletion mouse model, to generate from each a pair of cell lines. The AD-Ca cell lines (E2 and E4) and the ADI-Ca cell lines (cE1 and cE2) display biallelic deletion at the Pten gene locus, an event which is specific for the prostate epithelium for this mouse model and a fairly similar level of expression of the androgen receptor (AR). The ADI-Ca cell lines (cE series) grow well in the absence of androgen, display increased AR transcription under androgendeprived environment, and retain the sensitivity to increased proliferation when androgen is supplemented. The AD-Ca cell lines (E series) grow slowly in the absence of androgen and, unlike cE cells, do not show increased AR expression when maintained in the absence of androgen. The detection of epithelial cell markers, such as CK8, CK14, CK18, and E-cadherin in the cE series is conforming with the polygonal epithelial morphology of these cells in culture. The E cells also present mostly polygonal-shaped morphology with a small percent of cells with fibroblastoid morphology and produce little or very low levels of cytokeratins but increased levels of vimentin, Twist, and Slug, the markers known to be associated with epithelial– mesenchymal transition. Each of the cell lines, when inoculated subcutaneously into male or female NOD.SCID mice induced tumors within 8 weeks with 100% incidence. Histopathological examinations of the tumor

sections, however, led to noticeable biological differences. The cE series engenders adenocarcinomas, particularly in male hosts, and the E series induces sarcomatoid carcinomas (positively stained for CK8 and AR as well as vimentin expression) in either male or female hosts. These new cell lines are promising models for the elucidation of the androgen metabolism and their role in prostate cancer.

RB INACTIVATION ACCELERATES NEOPLATIC GROWTH AND SUBSTITUTES FOR RECURRENT AMPLIFICATION OF CIAP1, CIAP2 AND YAP1 IN SPORADIC MAMMARY CARCINOMA ASSOCIATED WITH P53 DEFICIENCY

Le Cheng, Zongxiang Zhou, Andrea Flesken-Nikitin, Ilja A. Toshkov, Wei Wang, John Camps, Thomas Ried, and Alexander Yu. Nikitin, (2010). Oncogene. 29: 5700-50711. PMID: 20676140.

Abstract

Genetically defined mouse models offer an important tool to identify critical secondary genetic alterations with relevance to human cancer pathogenesis. We used newly generated MMTV-Cre105Ayn mice to inactivate p53 and/or Rb strictly in the mammary epithelium, and to determine recurrent genomic changes associated with deficiencies of these genes. p53 inactivation led to formation of estrogen receptor-positive raloxifene-responsive mammary carcinomas with features of luminal subtype B. Rb deficiency was insufficient to initiate carcinogenesis but promoted genomic instability and growth rate of neoplasms associated with p53 inactivation. Genome-wide analysis of mammary carcinomas identified a recurrent amplification at chromosome band 9A1, a locus orthologous to human 11q22, which contains protooncogenes cIAP1 (Birc2), cIAP2 (Birc3) and Yap1. It is interesting that this amplicon was preferentially detected in carcinomas carrying wild-type Rb. However, all three genes were overexpressed in carcinomas with p53 and Rb inactivation, likely due to E2F-mediated transactivation, and cooperated in carcinogenesis according to gene knockdown experiments. These findings establish a model of luminal subtype B mammary carcinoma, identify critical role of cIAP1, cIAP2 and Yap1 co-expression in mammary carcinogenesis and provide an explanation for the lack of recurrent amplifications of cIAP1, cIAP2 and Yap1 in some tumors with frequent Rb deficiency, such as mammary carcinoma.

CONDITIONAL KNOCKOUT OF FIBRONECTIN ABROGATES MOUSE MAMMARY GLAND LOBULOALVEOLAR DIFFERENTIATION

Keyi Liu, Le Cheng, Andrea Flesken-Nikitin, Lynn Huang, Alexander Yu. Nikitin, and Bendicht U. Pauli, (2010). Developmental Biology. 6: 11-24. PMID: 20624380.

Abstract

Fibronectin (Fn) plays an important part in the branching morphogenesis of salivary gland, lung, and kidney. Here, we examine the effect of the conditional knockout of Fn in the mammary epithelium [FnMEp−/−] on postnatal mammary gland development, using Cre-loxP-mediated gene knockout technology. Our data show that Fn deletion causes a moderate retardation in outgrowth and branching of the ductal tree in 5-week-old mice. These defects are partially compensated in virgin 16-week-old mice. However, mammary glands consisting of Fn-deficient epithelial cells fail to undergo normal lobuloalveolar differentiation during pregnancy. The severity of lobuloalveolar impairment ranged from lobular hypoplasia to aplasia in some cases and was associated with the amount of Fn protein recovered from these glands. Decreased rates of mammary epithelial cell proliferation accounted for delayed ductal outgrowth in virgin and lack of alveologenesis in pregnant FnMEp−/− mice. Concomitant decreased expression of integrin β1 (Itgb1) and lack of autophosphorylation of focal adhesion kinase (Fak) suggest that this pathology might, at least in part, be mediated by disruption of the Fn/Itgb1/Fak signaling pathway.

LOCAL MESENCHYMAL STEM/PROGENITOR CELLS ARE A PREFERENTIAL TARGET FOR INITIATION OF ADULT SOFT TISSUE SARCOMAS ASSOCIATED WITH P53 AND RB DEFICIENCY

Jinhyang Choi, Stephen J. Curtis, David M. Roy, Andrea Flesken-Nikitin, and Alexander Yu. Nikitin, (2010). The American Journal of Pathology. 177: 2645-2658. PMID: 20864684.

Abstract

The cell of origin and pathogenesis of the majority of adult soft tissue sarcomas (STS) remains poorly understood. Because mutations in both the *P53* and *RB* tumor suppressor genes are frequent in STS in humans, we inactivated these genes by Cre-*loxP*–mediated recombination in mice with floxed *p53* and *Rb*. Ninety-three percent of mice developed spindle cell/ pleomorphic sarcomas after a single subcutaneous injection of adenovirus carrying Cre-recombinase. Similar to human STS, these sarcomas overexpress Cxcr4, which contributes to their invasive properties. Using irradiation chimeras generated by transplanting bone marrow cells from mice carrying either the *Rosa26StoploxPLacZ* or the *Z/EG* reporter, as well as the floxed *p53* and *Rb* genes, into irradiated *p53loxP/loxPRbloxP/loxP* mice, it was determined that sarcomas do not originate from bone marrow–derived cells, such as macrophages, but arise from the local resident cells. At the same time, dermal mesenchymal stem cells isolated by strict plastic adherence and low levels of Sca-1 expression (Sca-1low, CD31negCD45neg) have shown enhanced potential for malignant transformation according to soft agar, invasion, and tumorigenicity assays, after the conditional inactivation of both *p53* and *Rb*. Sarcomas formed after transplantation of these cells have features typical for undifferentiated high-grade pleomorphic sarcomas. Taken together, our studies indicate that local Sca-1low dermal mesenchymal stem/progenitor cells are preferential targets for malignant transformation associated with deficiencies in both *p53* and *Rb*.